6-25-2015

SPECTROSCOPIC, IMAGING, AND DOPING STUDIES OF PUSH-PULL CONJUGATED POLYMER SOLAR CELLS

Eric Jeri Jon Martin

Eric J. J. Martin
Candidate

Nanoscience and Microsystems
Department

This dissertation is approved, and it is acceptable in quality and form for publication:

Approved by the Dissertation Committee:

Dr. John K. Grey Chairperson

Dr. Ganesh Balakrishnan

Dr. Sang Eon Han

Dr. David Dunlap

SPECTROSCOPIC, IMAGING, AND DOPING STUDIES OF PUSH-PULL CONJUGATED POLYMER SOLAR CELLS

BY

ERIC J. J. MARTIN

Bachelor of Science, Materials Science and Engineering, University of Arizona, 1996
Master of Music, Music Performance, Northwestern University, 1998
Master of Science, Materials Science and Engineering, Northwestern University, 2004

DISSERTATION

Submitted in Partial Fulfillment of the
Requirements for the Degree of
Doctor of Philosophy

Nanoscience and Microsystems

The University of New Mexico
Albuquerque, New Mexico

May, 2015

Acknowledgements

The work presented herein would not have been possible without the help and support of a great many people. First, I need to thank Professor John Grey for accepting me into his research group and for his guidance and direction throughout my Ph.D. work and research efforts. My thanks also go to my friends and members of the Grey research group, Jian Gao, Adam Wise, Tray Niles, Alan Thomas, John Rabinowitz, Lee Martin, Tom Martin, Jose Garcia, and Cody Aldaz, and to my good friends Ryan Johnson, Ben Stein, Logan Giles, Michael Williams, Wenhan He, and Xiaobei Chen for their help and lively discussions of experiments, theory, and coursework. I need to thank Heather Armstrong for her friendship and for making the admissions process and all administrative aspects of this degree flow so smoothly. I need to thank Dr. Stephen Doorn at Los Alamos National Laboratory and Professors Carlos Silva and Michel Côté at the Université de Montréal for the use of their equipment, help with computational studies, and valuable insights into the data. I also thank Dr. Françoise Provencher (U. de Montréal), Dr. Hagen Telg (LANL), and Dr. Erik Harroz (LANL) for their help with experimental setups and data collection, and Nicolas Bérubé (U. de Montréal) for his help with density functional theory calculations. And finally, I send my most heartfelt thanks and deepest appreciation to my family, my wife Adriana, my mom Carol and dad John, their respective spouses Tom and Pat, my sister Christie, and my uncles Gary and Ed for providing me with the means, encouragement, and support without which I could never have arrived at this point.

SPECTROSCOPIC, IMAGING, AND DOPING STUDIES OF PUSH-PULL CONJUGATED POLYMER SOLAR CELLS

By

ERIC J. J. MARTIN

B. S., Materials Science and Engineering, University of Arizona, 1996
M. M., Music Performance, Northwestern University, 1998
M. S., Materials Science and Engineering, Northwestern University, 2004

Ph. D., Nanoscience and Microsystems, The University of New Mexico, 2015

ABSTRACT

Organic Photovoltaics (OPV) have the potential to provide inexpensive, renewable electric power to satisfy increasing global energy demands due to their low materials and processing costs. Poly[2,6-(4,4-bis-(2-ethylhexyl)-4*H*-cyclopenta [2,1-*b*;3,4-*b*′]dithiophene)-*alt*-4,7(2,1,3-benzothiadiazole)] (PCPDTBT) is a promising candidate for use in solar cell active layers, and has produced OPV devices with power conversion efficiencies (PCEs) exceeding 5% when blended with fullerene electron acceptors. Although these results are encouraging, a molecular-level understanding of photophysical processes involved in photocurrent production is needed to propel the use of PCPDTBT and other conjugated molecules into widespread use in solar cells. The research presented herein is aimed at improving our understanding of the electronic processes that allow PCPDTBT to outperform its homopolymer counterparts in OPV devices. Electronic absorption and Raman spectroscopies are used to probe the morphology-dependent optical properties of PCPDTBT in pristine nanoparticles and thin films and in thin film blends with [6,6]-phenyl C_{61} butyric acid methyl ester (PCBM) and 1,8-octanedithiol (ODT). Absorption spectra suggest decreased polymer order in

nanoparticles and increased polymer ordering in thin film blends with PCBM and ODT. Raman spectra collected at wavelengths spanning the entire absorption spectrum of PCPDTBT show selective excitation of the benzothiadiazole (BT) vibrational modes at low excitation energies and cyclopentadithiophene (CPDT) vibrational modes at high excitation energies. In addition, density functional theory (DFT) calculations provide a means of assigning specific molecular vibrational modes, and provide more insight into the interactions between PCPDTBT and PCBM in functional solar cell devices. Raman intensity and frequency imaging of PCPDTBT:PCBM and PCPDTBT:PCBM:ODT blend thin films show correlations between areas of decreased BT vibrational activity and increased PCBM vibrational mode activity, suggesting preferential interaction between the acceptor moiety and PCBM. Photocurrent imaging of PCPDTBT:PCBM:ODT solar cell devices shows areas of higher photocurrent production in well-blended regions of the active layers, suggesting some degree of disorder and more thorough intercalation of PCBM into PCPDTBT domains are advantageous for increased photocurrent production.

Doping PCPDTBT with the strong electron acceptor 2,3,5,6-tetrafluoro-7,7,8,8-tetracyanoquinodimethane (F_4-TCNQ) allows devices based on these blends to show improved power conversion efficiencies (PCEs), as well as improvements in other solar cell operating parameters and figures of merit. Blends of PCPDTBT with the electron acceptors 2,3-Dichloro-5,6-dicyano-1,4-benzoquinone (DDQ) and F_4-TCNQ are investigated with absorption and Raman spectroscopies in an effort to better understand the reasons behind these performance enhancements and the preferential interactions between these dopant molecules and the PCPDTBT backbone. Absorption spectra of doped PCPDTBT thin films show red-shifts in the low-energy PCPDTBT absorption

peak and decreased intensity of the high-energy absorption peak, suggesting increased polymer ordering upon addition of electron-accepting dopant species. Raman spectra of doped PCPDTBT thin films reveal increasing BT vibrational activity with increasing doping levels of both DDQ and F_4-TCNQ, suggesting preferential interaction between the dopants and the polymer acceptor moiety. DFT calculations provide additional insight into the interactions between PCPDTBT and these dopant molecules, showing varying degrees of charge transfer between the polymer and dopants as a function of the position of the dopant molecule relative to the CPDT and BT moieties.

Declaration

This dissertation is comprised of 5 chapters. Chapter 1 provides background information and motivations for this work, and introduces the area of study with an overview of the theoretical framework upon which the experiments and discussions are based. Chapters 2, 3, and 4 contain information that has been submitted for publication. Journal volumes, issue numbers, and page numbers are yet to be assigned.

My research advisor, John Grey, supervised all manuscripts for publication as corresponding author. Professors Carlos Silva and Michel Côté (University of Montréal) participated in the experiments in Chapter 2. Dr. Françoise Provencher, Laura-Isabelle Dion-Bertrand, and Nicolas Bérubé aided in the collection of data and calculations presented in Chapter 2.

Table of Contents

List of Figures

Chapter 3

List of Tables

List of Abbreviations

A	Electron Acceptor
AFM	Atomic force Microscopy
AM	Air Mass
BHJ	Bulk Heterojunction
C	Capacitance
CB	Chlorobenzene
CCD	Charge Coupled Device
cm-1	Reciprocal Centimeter (Wavenumber)
CS	Charge Separated
CT	Charge Transfer
CTC	Charge Transfer Complex
D	Electron Donor
Δ	Nuclear Displacement
DDQ	2,3-Dichloro-5,6-dicyano-1,4-benzoquinone
DFT	Density Functional Theory
DOS	Density of Electronic States
E_{00}	Energy of Electronic Origin
ε_0	Permittivity of Free Space
ε_r	Relative Permittivity (Dielectric Constant)
EPR	Electron Paramagnetic Resonance
EQE	External Quantum Efficiency

ET	Energy Transfer
F_4-TCNQ	2,3,5,6-tetrafluoro-7,7,8,8-tetracyanoquinodimethane
F8BT	Poly-(9,9-dioctylfluorene-co-benzothiadiazole)
FET	Field Effect Transistor
FF	Fill Factor
Γ	Phenomenological Damping Factor
GIWAXS	Grazing-Incidence Wide Angle X-ray Scattering
h	Planck's Constant
ħ	$h/2\pi$
HOMO	Highest Occupied Molecular Orbital
I(ω)	Absorption Intensity as a Function of Frequency
I_{if}	Raman Intensity
IMPS	Intensity Modulated Photocurrent Spectroscopy
IQE	Internal Quantum Efficiency
I_{MP}	Current at Maximum Power
I_{SC}	Short-Circuit Current
ITO	Indium Tin Oxide (tin-doped indium Oxide)
LUMO	Lowest Unoccupied Molecular Orbital
MDMO-PPV	Poly[2-methoxy-5-(3,7-dimethyloctyloxy)-1,4-phenylene-vinylene]
MEH-PPV	Poly[2-methoxy-5-(2-ethylhexyloxy)-1,4-phenylenevinylene]
NIR	Near-Infrared
n_k	Overtone Order for Mode k
nm	Nanometer

NP	Nanoparticle
NSOM	Near-Field Scanning Optical Microscopy
OFET	Organic Field Effect Transistor
OLED	Organic Light Emitting Diode
OPV	Organic Photovoltaic
φ	Vibrational Wavefunction
Φ_{in}	Incident Radiant Power
P3HT	Poly (3-hexylthiophene)
PCE	Power Conversion Efficiency
$PC_{61}BM$	[6, 6]-phenyl-C61-butyric acid methyl ester
PCBM	[6, 6]-phenyl-C61-butyric acid methyl ester
PCDTBT	Poly[N-9'-heptadecanyl-2,7-carbazole-alt-5,5-(4',7'-di-2-thienyl-2',1',3'-benzothiadiazole)]
PCPDTBT	Poly[2,6-(4,4-bis-(2-ethylhexyl)-4H-cyclopenta [2,1-b;3,4-b']dithiophene)-alt-4,7(2,1,3-benzothiadiazole)]
p-DTS(FBTTh2)2	7,7'-(4,4-bis(2-ethylhexyl)-4H-silolo[3,2-b:4,5-b']dithiophene-2,6-diyl)bis(6-fluoro-4-(5′-hexyl-[2,2'-bithiophen]-5-yl)benzo[c][1,2,5] thiadiazole)
PEDOT:PSS	Poly (3, 4-ethylenedioxythiophene) poly (styrenesulfonate)
PL	Photoluminescence
P_{MAX}	Maximum Power
PPV	Poly Phenylene Vinylene
PTB7	Poly[[4,8- bis[(2-ethylhexyl)oxy]benzo[1,2-b:4,5-b']dithiophene-

	2,6-diyl][3-fluoro-2-[(2-ethylhexyl)carbonyl]thieno[3,4-b]thiophenediyl]]
Q	Nuclear Coordinate
SEM	Scanning Electron Microscopy
STEM	Scanning Transmission Electron Microscopy
TCE	Trichloroethylene
TCO	Transparent Conducting Oxide
TEM	Transmission Electron Microscopy
UV	Ultraviolet
V_{MP}	Voltage at Maximum Power
V_{OC}	Open-Circuit Voltage
$W_2(hpp)_4$	Ditungsten tetra(1,3,4,6,7,8-hexahydro-2H-pyrimido[1,2-a]pyrimidine)
XRD	X-ray Diffraction
ω_I	Incident Photon Frequency
ω_k	Vibrational Frequency of Mode k
ω_S	Scattered Photon Frequency

1. Introduction

Alternating donor/acceptor copolymers have shown considerable promise as active materials in organic photovoltaic devices.[1-4] As such, a great number of studies have been published focusing on improving the performance of solar cells based on these polymers and understanding the photophysical processes that underlie their improved performance in these devices relative to their homopolymer counterparts.[5-11] However, the relationships between polymer conformation, solar cell active layer morphology, and material functions are still debated. This dissertation is focused on improving our basic understanding of structure-function relationships in one such polymer, poly[2,6-(4,4-bis-(2-ethylhexyl)-4H-cyclopenta[2,1-b;3,4-b′]dithiophene)-alt-4,7(2,1,3-benzothiadiazole)] (PCPDTBT), and its interactions with the commonly used electron acceptor [6,6]-phenyl C_{61} butyric acid methyl ester (PCBM) and small molecule strong electron acceptors. Spectroscopic techniques including absorption and Raman spectroscopies are used to investigate the morphology the polymer adopts in pristine and blend thin films, and the response of the polymer as it is exposed to photons of varied energies, as well as interactions between the polymer donor and acceptor moieties and electron acceptors. Raman and photocurrent imaging are employed to increase our understanding of these interactions, and density functional theory calculations supplement the experimental data with views of specific polymer vibrational modes and electronic states.

1.1 Background and Motivation

Climate change as a result of fossil fuel consumption has been debated in political arenas and the media for the better part of the last fifteen years. The fact that our current rate of

fossil fuel consumption (~8×10^{16} BTU/year[12]) outpaces the rate of fossil fuel production on earth (~0) means we will inevitably exhaust these resources. As a result, we must look for new, renewable sources of energy to satisfy our increasing energy appetite. Former U.S. Energy Secretary Steven Chu remarked, "the Stone Age did not end because we ran out of stones; we transitioned to better solutions."[13]

Among renewable energy technologies, solar electric power offers the potential to be the most abundant and most efficient source for clean, renewable electric power on our future energy menu. Although the technology to convert light directly into electricity has been available for quite some time, it has not been until relatively recently that great strides have been made in improving solar cell device efficiencies through materials selection and processing techniques. Still, the cost-per-watt of conventional inorganic semiconductor-based solar cells prohibits widespread implementation of photovoltaic power throughout the world. For this reason, forward-thinking governments have established financial incentives to utilities, private companies, and individuals to encourage installation of photovoltaic arrays for power generation.

Organic photovoltaics (OPVs) have the potential to provide low-cost, renewable electrical power for our growing energy demands.[14-19] Although not yet as efficient as their inorganic semiconductor counterparts, OPV materials are entirely solution-processable, and as a result, offer a considerable reduction in production costs. Research efforts in this field have expanded considerably over the last decade with the goals of understanding the material-driven performance characteristics of organic solar cells and building cells with higher power conversion efficiencies.

The overarching goal of the work presented in this dissertation is to increase our understanding of the photophysical and electronic behaviors of one conjugated polymer that has been used in the active layers of some of the highest-performing OPV devices to date. [20-25] The investigations in the following chapters aim to improve our understanding of these behaviors through spectroscopic investigations and density functional theory simulations. First, these studies seek to enhance our understanding of the morphologies PCPDTBT adopts when blended with PCBM and small molecule electron acceptors. Second, these studies are intended to provide insight into how PCBM and electron-accepting dopants interact with specific PCPDTBT backbone moieties. And finally, these investigations aim to reveal the effects of local morphology on photocurrent production in PCPDTBT blend solar cell devices. It is my hope that the information gained through this research can spur new investigations and ultimately lead to commercially viable organic solar cells and broadened implementation of solar energy.

1.2 A Brief History of Organic Solar Cells

Credit for the discovery of the photovoltaic effect has been given to Parisian physicist Edmond Becquerel. His 1839 observation of current and voltage produced by an illuminated electrochemical cell represents the first documented success in converting light to electrical power.[26] Investigations into solid state solar cells later in the 19th century with Selenium gave way to studies of other inorganic semiconductors in the first half of the 20th century, and the development of the first silicon cell in 1954 at Bell Labs.[27] A few years later in 1958, Kearns and Calvin reported photovoltaic behavior in a device made by coating magnesium phthalocyanine with oxidized tetramethyl p-

phenylenediamine.[28] Studies of photovoltaic cells based on phthalocyanines continued, and in 1973, Amal Ghosh et al. published results for Al/Mg phthalocyanine-Ag sandwich cells with PCEs of 0.001%.[29] In 1986, C. W. Tang reported a power conversion efficiency of about 1% for a two-layer photovoltaic cell using Cu-phthalocyanine and a perylene tetracarboxylic derivative.[30] While the cell produced a modest V_{OC} and I_{SC}, the device showed very good rectifying behavior with an impressive FF of 0.65. In the early 1990s, charge transfer behavior between different moieties in porphyrins was investigated by Suslick et al.[31] Niyazi Sariciftci et al. made the first conjugated polymer/fullerene solar cell device in 1993 using Poly[2-methoxy-5-(2-ethylhexyloxy)-1,4-phenylenevinylene] (MEH-PPV) and C_{60}.[32] The first bulk heterojunction (BHJ) device was reported two years later by Yu et al., wherein the authors used the functionalized fullerene phenyl-C61-butyric acid methyl ester (PCBM) in place of C_{60}.[33] The utilization of PCBM allowed the active layer to be entirely processed in solution, as opposed to thermally depositing C_{60} onto polymer film. In 2002, MacKenzie, Arias, Friend, and Huck patented light emissive, photodetecting, and photovoltaic devices based on the donor/acceptor copolymer Poly(9,9-dioctylfluorene-*alt*-benzothiadiazole) (F8BT).[34] Mitsubishi Chemical currently holds the record for an OPV cell at 11.1% PCE as verified by the National Renewable Energy Laboratory (NREL) in 2012.[35] Unfortunately, the details of the materials and structure of this device have not been published. The German company Heliatek reported a PCE of 12% for their OPV cell in 2013,[36] but this efficiency has not yet been verified by an independent laboratory.

1.3 Important Parameters for Solar Cell Performance Characterization

Solar cell performance is characterized by the current-voltage response of the cell under illumination. Important parameters include the open-circuit voltage (V_{OC}), the short-circuit current (I_{SC}), the maximum power point (MPP), the voltage at the maximum power point (V_{MP}), and the current at the maximum power point (I_{MP}). These points are illustrated in Figure A along with the fill factor (FF). The fill factor is a figure of merit for solar cells and is a measure of the ideality of device performance, and is defined as shown in Figure 1.3.1. Graphically, this can be interpreted as the "rectangularity" of the I-V curve, and is illustrated by the gray area in Figure A.

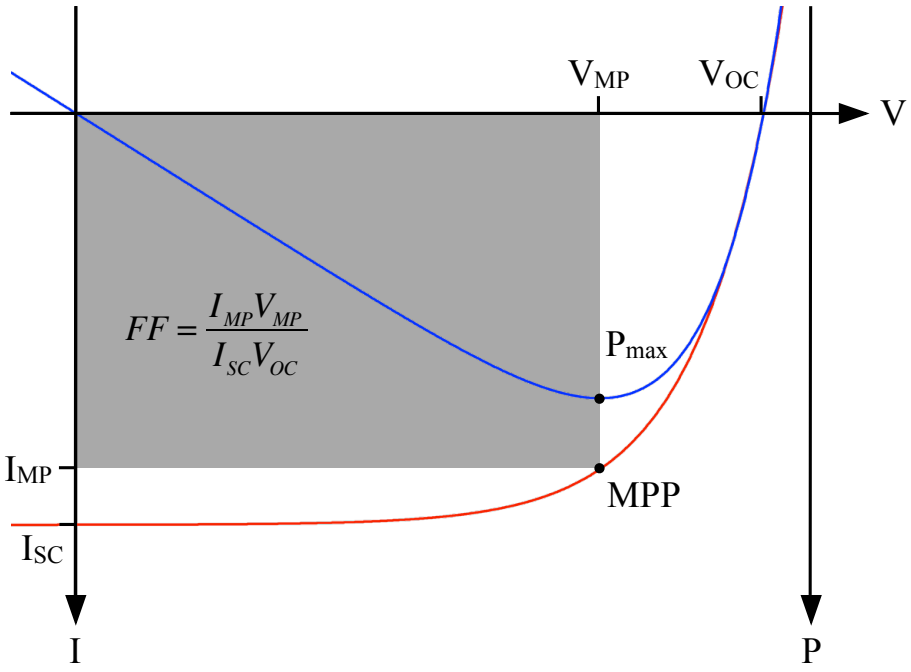

Figure 1.3.1. Typical current-voltage (red) and power (blue) curves for a solar cell device illustrating points of importance and the fill factor figure of merit.

$$PCE = \frac{I_{MP}V_{MP}}{\Phi_{in}} = \frac{I_{SC}V_{OC}FF}{\Phi_{in}} \qquad (1.3.1)$$

Equation 1 relates important points and FF from Figure A to power conversion efficiency (PCE). Φ_{in} is the radiometric power incident on the solar cell device.

1.4 Basic Photophysical Operation of an Organic Photovoltaic Device

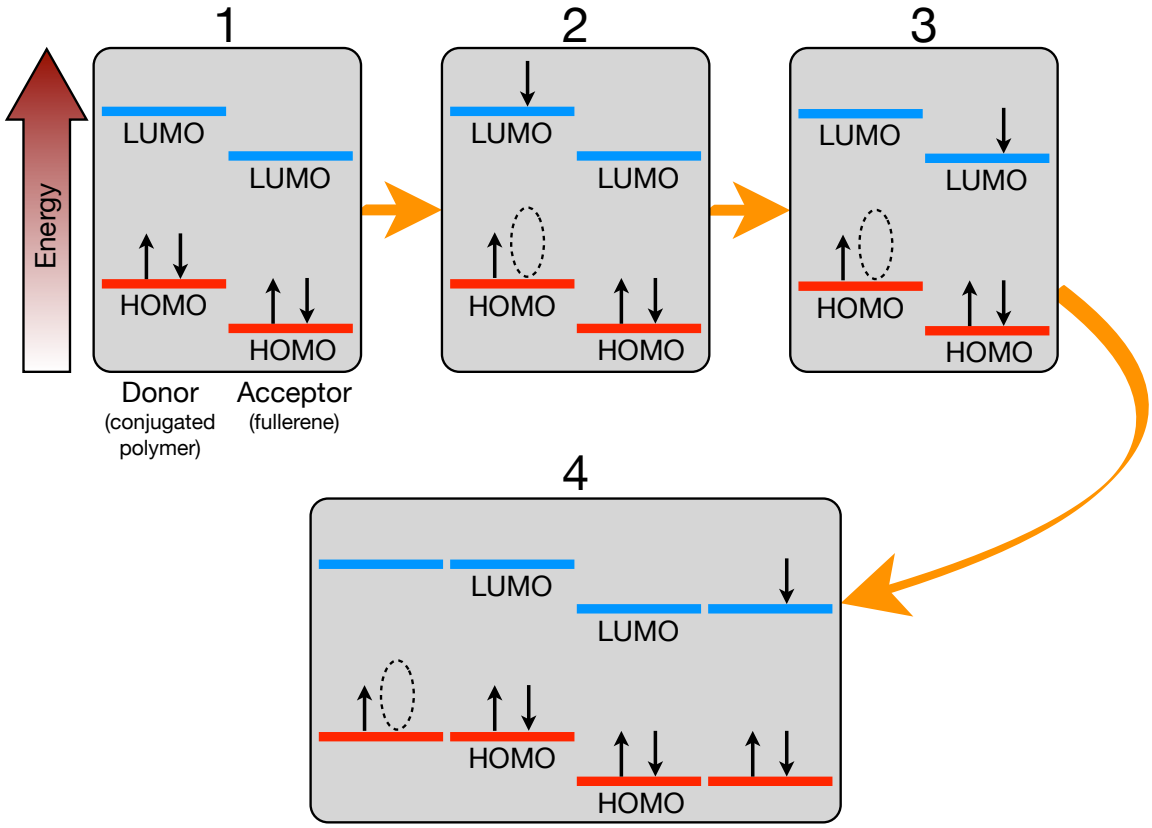

Figure 1.4.1. Basic photophysical operation of an OPV device.

The basic steps involved in generating photocurrent are illustrated in Figure 1.4.1.[37-42] Generation of photocurrent requires a heterojunction between a donor species, e.g. a conjugated polymer, and an acceptor species, e.g. a fullerene, as in panel 1. Absorption of a photon by the donor promotes an electron into an excited state, the donor LUMO, leaving behind an electron vacancy or hole in the donor HOMO, as in panel 2. At this point, the electron in the donor LUMO is still coulombically bound to the hole it left behind in the HOMO, and the electron-hole pair, or exciton, must migrate or diffuse to an interface with an acceptor molecule before the electron decays radiatively or non-radiatively back to the HOMO. Once at the interface, the electron can hop across the

interface to the acceptor LUMO, creating a charge-transfer (CT) state, as in panel 3. The possibility exists for a photon to be absorbed by the acceptor and for the exciton to diffuse to an interface with a donor. The hole can then be transferred to the donor. The energy offset between the donor and acceptor LUMO levels must be such that the acceptor LUMO is at a lower energy than the donor LUMO, but not so low as to allow an electron from the donor HOMO to fall into the acceptor LUMO. This scenario would result in ground state charge transfer, creating a donor-acceptor salt and would prevent the photovoltaic process. An extended network of donor species and acceptor species must exist for exciton scission into free charge carriers, i.e., a charge separated (CS) state. The electron and hole must then migrate through the extended donor and acceptor networks, respectively, to be extracted at the device electrodes (panel 4). It is important to note that each step in photocurrent generation can proceed in reverse. After a donor electron is promoted to the LUMO, it can easily recombine with the hole in the HOMO radiatively, emitting another photon, or non-radiatively, imparting a phonon to the polymer. Once the electron and hole are in a CT state at the donor/acceptor interface, they can recombine at that point across the interface. It is also important to note that charge transfer between organic donors and acceptors is vibration-assisted and typically described using the non-adiabatic theory of charge transfer.[42-46] Should the molecular vibrations be insufficient to overcome the charge transfer activation barrier, for example when a sample is at a very low temperature, charge transfer will be unfavorable. Even when the electron and hole are in CS states, they can still migrate back to the interface at which they were separated and recombine, or the free charges can recombine with other free charges. Each of these "reverse" steps is detrimental to photovoltaic performance,

and it is only when charges are extracted at their respective electrodes that they can produce useable electrical power.

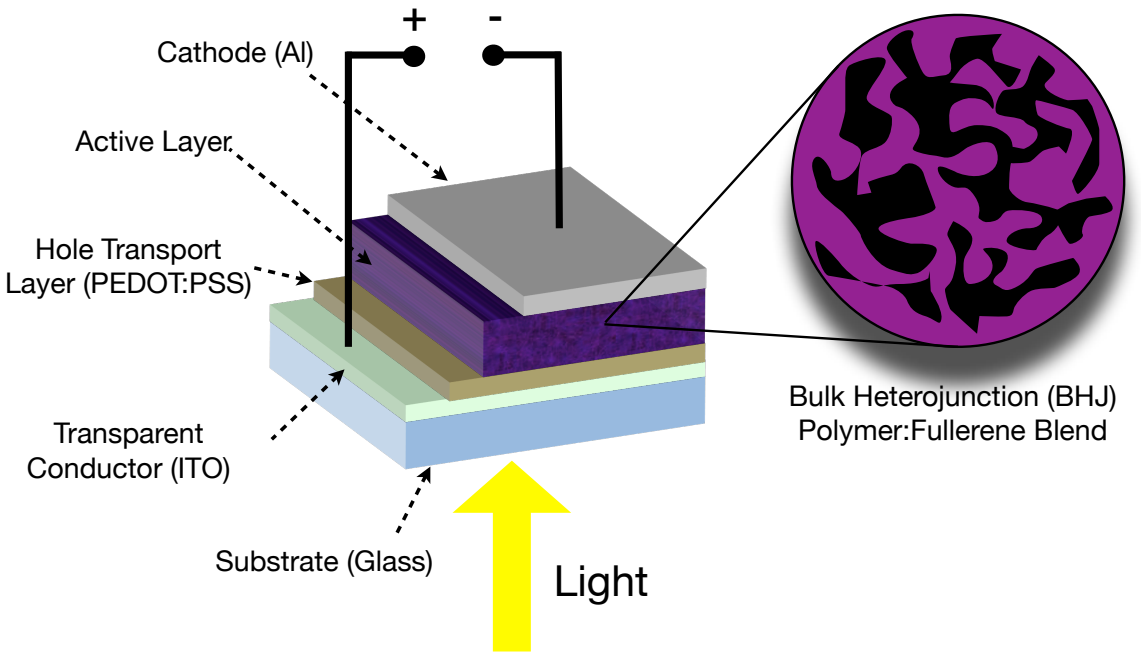

Figure 1.5.1. OPV bulk heterojunction device structure.

1.5 OPV Device Structure

The basic structure of a simple bulk heterojunction (BHJ) OPV device, and the structure for the devices in this work, is illustrated in Figure 1.5.1.[42,47-49] A glass substrate is coated with a transparent conductor, most commonly tin-doped indium oxide (ITO), which serves as the device anode. Poly(3,4-ethylenedioxythiophene) polystyrene sulfonate (PEDOT:PSS) is spun onto the ITO from an aqueous solution as a hole transport layer. The active layer of the device is a donor/acceptor blend, typically a blend of conjugated polymer and PCBM in solution, which is spun on top of the PEDOT:PSS. The D/A blend forms an interpenetrating network of polymer- and fullerene-rich domains

necessary for charge transport. A post-processing step, such as annealing or an additive such as 1,8-octanedithiol (ODT) or diiodooctane (DIO) is sometimes necessary to drive phase segregation in the active layer. Aluminum is then evaporated onto the active layer to form the device cathode.

1.6 Donor/Acceptor Copolymers vs. Homopolymers

Relative newcomers to the photovoltaic materials arena, alternating donor/acceptor (d/a) co-polymers have shown considerable promise for improving the power conversion efficiencies of organic solar cells based on bulk heterojunction (BHJ) conjugated polymer and fullerene blends. [1,4,5,8] As a note to the reader, lower-case "d" and "a" refer to the donor and acceptor moieties on the polymer backbone, as opposed to capital "D" and "A," which refer to the donor and acceptor species (molecules) in a functioning solar cell active layer. In contrast to homopolymers that consist of a single repeat unit, the backbones of d/a copolymers are constructed with alternating electron-donating and electron-accepting moieties. The alternating moieties create a "push-pull" effect that results in significant charge transfer along the backbone, broader absorption profiles, and narrower optical energy gaps that allow the polymers to capture more of the red and near-infrared (NIR) portions of the solar spectrum.[6,39,50-54] Whereas homopolymers generally show absorption profiles with a single, broad band in the visible, donor/acceptor copolymers display characteristic two-maximum absorption profiles, generally with a less intense and narrower high-energy peak and a broader, more intense low-energy peak. Figure 1.6.1 shows absorption profiles for poly[2,6-(4,4-bis-(2-ethylhexyl)-4H-cyclopenta[2,1-b;3,4-b′]dithiophene)-alt-4,7(2,1,3-benzothiadiazole)]

(PCPDTBT), which is the polymer of interest for the present work, as well as two other d/a copolymers commonly used in OPV devices, Poly(9,9-dioctylfluorene-*alt*-benzothiadiazole) (F8BT)[55] and Poly[N-9'-heptadecanyl-2,7-carbazole-alt-5,5-(4',7'-di-2-thienyl-2',1',3'-benzothiadiazole)] (PCDTBT). The structures of these polymers are shown in Figure 1.6.2. This work is focused on examinations of PCPDTBT and its blends with soluble fullerenes, e.g., [6,6]-phenyl C_{61} butyric acid methyl ester (PCBM) and the small molecule strong electron acceptors 2,3-Dichloro-5,6-dicyano-1,4-benzoquinone (DDQ) and 2,3,5,6-Tetrafluoro-7,7,8,8-tetracyanoquinodimethane (F_4-TCNQ). The reader is referred to Chapter 4, Figure 4.1.1 for an illustration of the structures of DDQ and F_4-TCNQ, and to Figure 4.1.2 for an illustration of the highest occupied molecular orbital (HOMO) and lowest unoccupied molecular orbital (LUMO) energy levels for PCPDTBT, PCBM, DDQ, and F_4-TCNQ relative to vacuum.

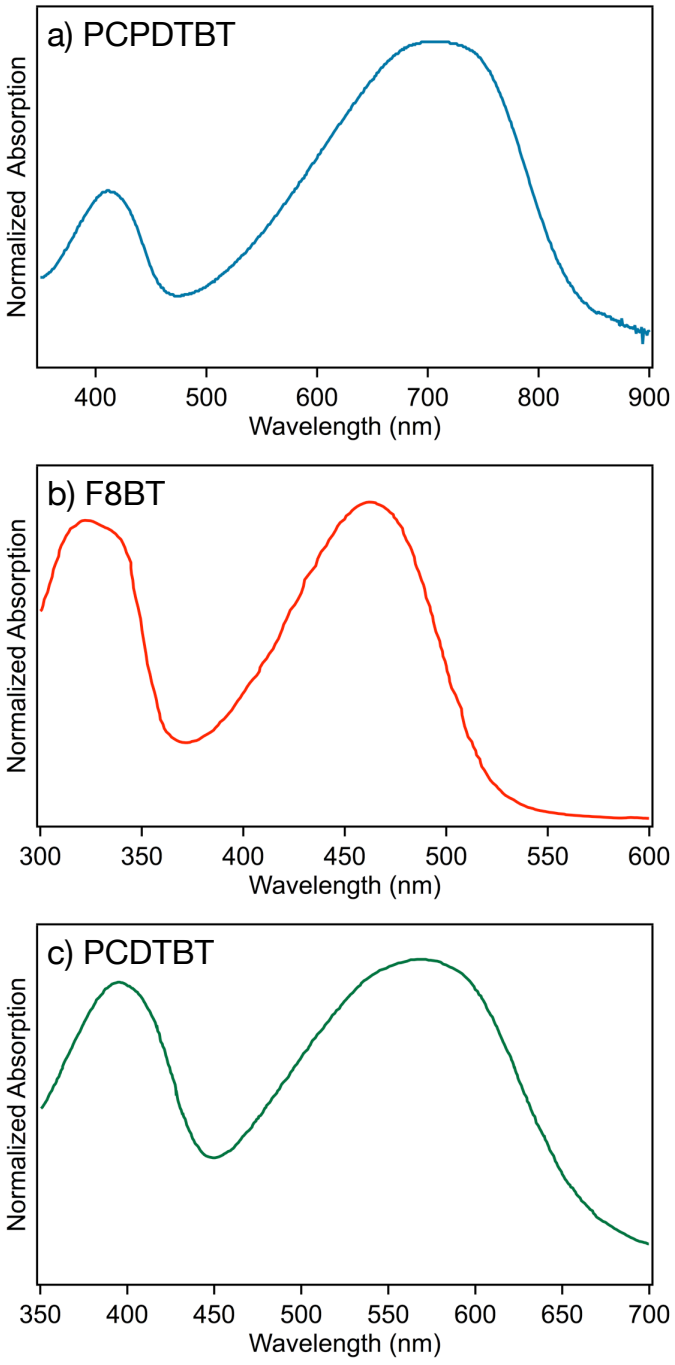

Figure 1.6.1. Absorption profiles for PCPDTBT, F8BT, and PCDTBT.

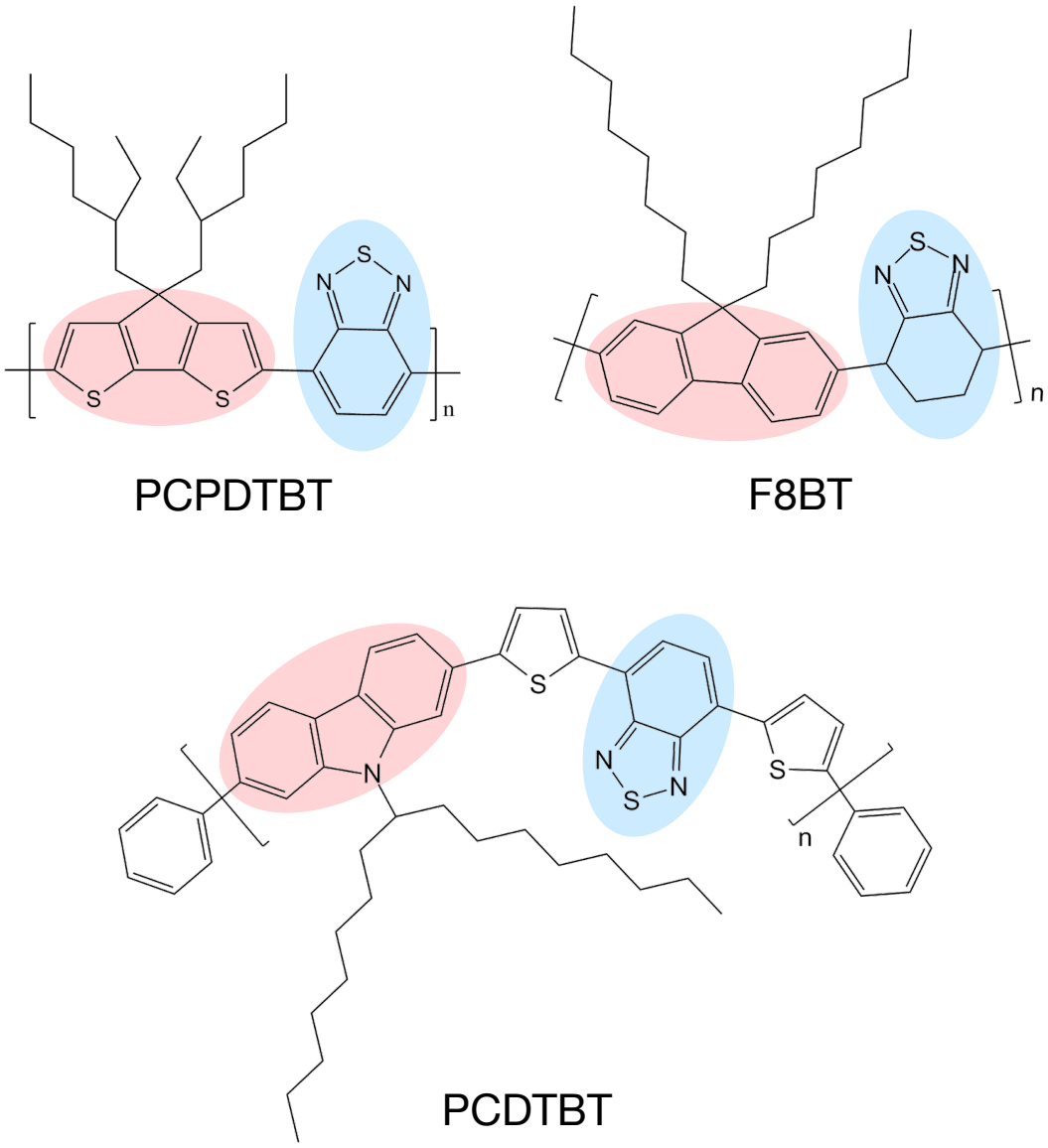

Figure 1.6.2. Structures of PCPDTBT, F8BT, and PCDTBT highlighting the donor (pink) and acceptor (blue) moieties.

The excited state wavefunctions of conjugated d/a polymers tend to be more localized on the acceptor moiety than the ground state wavefunctions due to the charge transfer characteristics of the polymer backbone, while the opposite is generally true of their homopolymer counterparts. The reader is referred to Chapter 2, Figure 2.5.2 for an illustration of HOMO and LUMO calculated electron densities in PCPDTBT. The push-pull, charge transfer character, and as a result, the localization of the electronic

wavefunction in the excited state, are especially sensitive to polymer conformation, namely, d/a orientation as well as packing characteristics in the condensed phase.[23,56-59] It is likely that the charge separation on the polymer backbone creates a lower-energy-barrier pathway for charge transfer to the fullerene in d/a polymer/fullerene blends. Figure 1.6.3 shows the structures of PCBM and ODT.

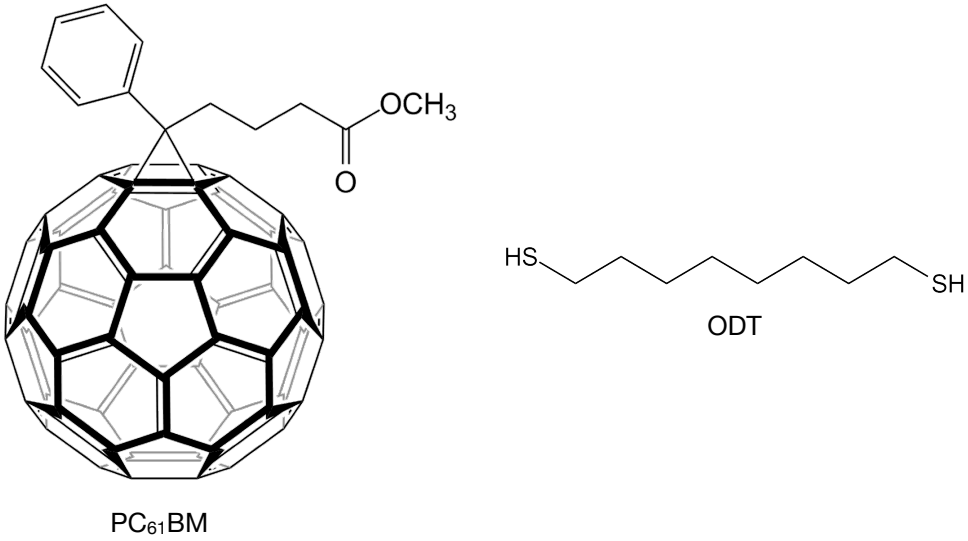

Figure 1.6.3. Structures of PCBM and ODT.

1.7 Overview of Spectroscopic Techniques Used in This Work

Although there are a number of fine characterization techniques for materials at the micro- and nanoscales, only optical techniques can provide insight into the electronic and vibrational behaviors of organic molecules. Electron microscopy techniques such as scanning electron microscopy (SEM) and transmission electron microscopy (TEM) can provide a good amount of structural and topographical information, but cannot provide molecular-level chemical and charge transfer information. Scanning probe techniques such as atomic force microscopy (AFM) and scanning tunneling microscopy (STM) can

give us excellent sub-nanometer height and even atomic-scale lateral resolution in the case of STM, but these techniques deliver little in the way of energetic or chemical information about the sample under investigation. The exception to this is near-field scanning optical microscopy (NSOM), which can deliver topographical and fluorescence information at resolutions less than 30 nm. Absorption and Raman spectroscopies can offer a wealth of information about the conformational, chemical, energetic features of materials, molecules, and atoms, and are chosen as the primary characterization techniques to investigate PCPDTBT and its blends with PCBM, ODT, DDQ, and F_4-TCNQ. Figure 1.7.1 shows a simplified schematic of the transitions that take place in absorption and Raman scattering.

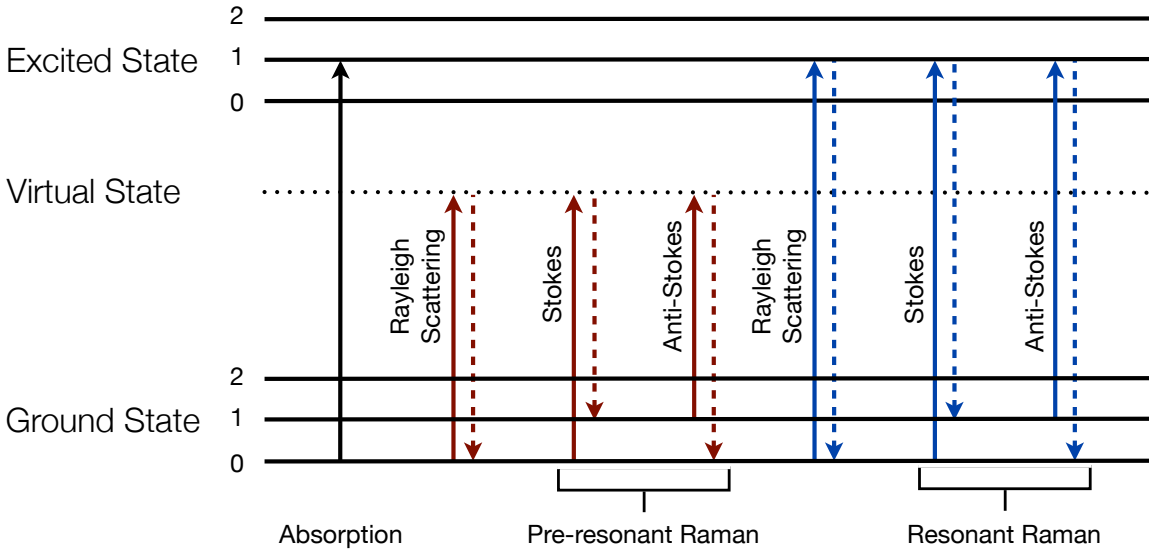

Figure 1.7.1. Processes involved in absorption, pre-resonant Raman scattering, and resonant Raman scattering.

The spectral absorption characteristics of materials, molecules, and atoms offer a wealth of information about the electronic energy landscape these species possess. Absorption lineshapes reflect the strength with which photons promote electrons in a

sample from one electronic state to a higher-energy state as a function of photon energy. Absorption measurements across the near-ultraviolet, visible, and near infrared portions of the spectrum can tell us about the electronic transitions in conjugated molecules and polymers, and the excited state energy and vibrational levels that are accessible when these materials are exposed to light. As such, absorption spectroscopy can be thought of as optically "ringing the bell" of a molecule and "listening" in the excited state. Perhaps more importantly, and à propos to the investigations in the following chapters, absorption spectroscopy can reveal information about the morphological and charge transfer characteristics conjugated polymers display in a variety of local environments.

Raman scattering provides us with information about the vibrational modes and the ground and excited state landscapes of a molecule. Raman spectroscopy relies on the inelastic scattering of photons from an excited electronic potential energy surface, as in the case of resonant Raman scattering, or from a virtual state or higher-energy vibrational level somewhere between the ground and excited states, as in pre-resonant Raman scattering. The net effects in the case of Stokes scattering are that the molecule is left in a higher ground vibrational state than before the scattering event, and that the scattered photon leaves with an energy one vibrational quantum less than the incident photon. In the case of Anti-Stokes scattering, the net effects are reversed. The molecule is left in a lower ground vibrational state, and the scattered photon is of a higher energy than the incident photon by one vibrational quantum. Anti-Stokes scattering is much weaker than Stokes scattering because Anti-Stokes scattering requires that a significant number of higher-energy ground vibrational states be occupied. This would only be the case if a sample were far above room temperature. Raman spectroscopy can be thought of as

optically "ringing the molecular bell" and "listening" in the ground state. Raman spectroscopy is a somewhat more "subtle" technique compared to absorption spectroscopy because the portion of photons scattered inelastically from a sample is typically only about one in 10^7.[60,61] When exciting a sample with photons of an energy corresponding to the energy of an electronic transition, the scattering efficiency can be enhanced by a factor of up to 10^6.[62-65]

1.8 Time-Dependent Theory of Absorption and Raman Spectroscopies

In the classical picture of electronic absorption, the Franck-Condon principle is often invoked, wherein a vertical transition between the ground and excited state potential energy surfaces occurs assuming stationary nuclei. The absorption spectrum is then generated by the overlap of the initial wavefunction with the excited state vibrational eigenfunctions. Taking this approach to interpret and predict spectra becomes cumbersome as the size of a molecule increases beyond just a few atoms. A similar problem is encountered in a classical effort to predict Raman spectra of molecules as the standard approach requires knowing everything about the excited state potential energy surface.[66] Again, this becomes terribly complicated when the number of atoms increases above two. A more convenient and intuitive explanation of absorption and Raman spectroscopies can be obtained through time-dependent quantum theory as described by E. J. Heller et al. in the early 1980s.[66-68] In Heller's time-dependent approach, spectra are modeled by the motion of a single wavepacket, excited from the ground state potential energy surface to the excited state potential energy surface, as it moves and evolves as a function of time. Figure 1.8.1 shows a schematic of this process.

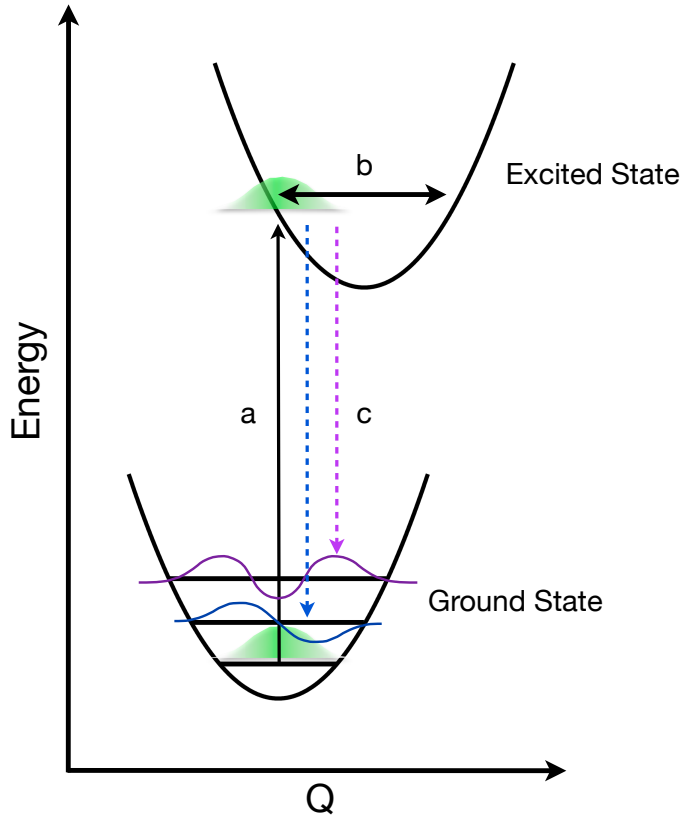

Figure 1.8.1. Schematic representation of the projection of a ground state wavefunction onto the excited state potential surface (a), propagation on the excited state potential surface (b), and projection back down to the ground state vibrational levels (c) where it overlaps with excited vibrational wavefunctions in the ground state.

In the time-dependent formalism, the absorption intensity as a function of incident photon frequency ω is the Fourier transform of the wavepacket overlap with itself, or autocorrelation, as a function of time $\langle \varphi | \varphi(t) \rangle$:[69]

$$I(\omega) = \omega \int_{-\infty}^{\infty} e^{i\omega t} \langle \varphi | \varphi(t) \rangle dt \qquad (1.8.1)$$

The same expression can be used to calculate emission spectra by changing the factor in front of the integral to ω^3. The overlap includes all displaced vibrational modes and can be expressed as:

$$\langle \varphi | \varphi(t) \rangle = \exp\left\{ -\sum_k \left[\frac{1}{2}\Delta_k^2 \left(1 - e^{-i\omega t}\right) - \frac{i\omega_k t}{2} \right] - \frac{iE_{00}t}{\hbar} - \Gamma^2 t^2 \right\} \qquad (1.8.2)$$

where Γ is a phenomenological damping factor, E_{00} is the energy of the electronic origin, ω_k is the frequency of vibrational mode k, and Δ_k is the unitless displacement of vibrational mode k. Maximum overlap occurs only at t = 0, with successive returns of the wavepacket to the Franck-Condon region producing progressively less overlap as the wavepacket is distorted and damped by its motion on the excited state potential surface. Plots of $\langle \varphi | \varphi(t) \rangle$ versus time and the resulting spectra following Fourier transforms can be seen in refs. 30 – 31 and 34 – 36.[44,66,67,70,71]

Applying a similar approach to resonant Raman spectroscopy, the intensity of a scattering at a frequency ω_S is given by:

$$I_{if} \propto \omega_I \omega_S^3 \left[\alpha_{fi}\right]^* \left[\alpha_{fi}\right] \qquad (1.8.3)$$

where ω_I is the incident photon frequency, ω_S is the scattered photon frequency, and α_{fi} is determined by the half-Fourier transform of the overlap as a function of time:

$$\left[\alpha_{fi}\right] = \frac{i}{\hbar}\int_0^\infty \langle \varphi_f | \varphi(t) \rangle \exp\left\{ \left[i\left(\omega_k + \omega_I - E_{00}\right) - \Gamma \right] t \right\} dt \qquad (1.8.4)$$

where again, ω_k is the frequency of vibrational mode k, Γ is a phenomenological damping factor, E_{00} is the energy of the electronic origin. As in the case of absorption, the overlap as a function of time is the key ingredient in calculating the Raman profile. The excited state displacements are also an important factor in determining the recurring overlap of $\varphi(t)$ with φ_f, and play a role in the appearance of Raman overtones and combination bands. In this case, the autocorrelation function can be expressed as:

$$\left\langle \varphi_f \middle| \varphi(t) \right\rangle = \prod_k \left\{ \exp\left[-\frac{\Delta_k^2}{2}\left(1-\exp\left(-i\omega_k t\right)\right) - \frac{i\omega_k t}{2} \right] \times \left(1-\exp\left(-i\omega_k t\right)\right)^{n_k} \times \frac{(-1)^{n_k}\,\Delta_k^{n_k}}{\left(2^{n_k} n_k\right)^{\frac{1}{2}}} \right\} \quad (1.8.5)$$

where n_k is the order of the overtone. While this expression can be used to fit experimental results, Savin's approximation gives us a far simpler method of estimating relative displacements when comparing Raman fundamental modes:[66]

$$\frac{I_k}{I_{k'}} = \frac{\omega_k^2 \Delta_k^2}{\omega_{k'}^2 \Delta_{k'}^2} \quad (1.8.6)$$

Part of the simplicity of this expression comes from the assumptions that the potential energy surfaces are harmonic (quadratic), that we are only concerned with very short times, and that the slope of the potential energy surface in the Franck-Condon region is the driving force that moves the wavepacket away from its initial position in the excited state. Greater displacement results in, for example, greater values of $\left\langle \varphi_1 \middle| \varphi_0(t) \right\rangle$ and $\left\langle \varphi_2 \middle| \varphi_0(t) \right\rangle$. Overtones are typically weak or absent in the Raman spectra of PCPDTBT, however, due to the large number and congestion of fundamental Raman modes, which creates "vibrational dissonance" whereby recurrence of $\varphi(t)$ is quickly suppressed.

1.9 Chapter Summaries

In Chapter 2, the absorption characteristics of PCPDTBT in thin films and nanoparticles, as well as in blends with PCBM and ODT are investigated. In addition to these ground-state absorption measurements, photoinduced absorption experiments are conducted to explore the excited state energetic landscape of PCPDTBT. We also use resonance Raman spectroscopic techniques to study the vibrational modes of PCPDTBT and local ordering of the polymer in PCBM blends, which are later combined with

imaging approaches in Chapter 3 to spatially resolve specific morphological features in functioning solar cell devices. By selectively exciting Raman spectra across the PCPDTBT absorption profile, we see good general agreement between Raman mode activity and absorption intensity. We also see increased donor vibrational mode activity when exciting at high energies, and increased acceptor mode activity when exciting at low excitation energies. Based on previous studies of d/a co-polymers and small molecules, the push-pull character of PCPDTBT is expected to be significantly modulated depending on the local composition of the blend thin film. Density functional theory (DFT) and time-dependent DFT (TD-DFT) simulations of Raman intensities and frequencies are performed that show increased localization of electron density on the benzothiadiazole (BT) moiety in the first excited state (~LUMO) compared to the ground state (~HOMO). This result agrees well with previous theoretical studies as well as photoelectron spectroscopy results of related push-pull D/A polymers that show BT localization is largely independent of the morphology and specific backbone chemical structure.

In Chapter 3, we apply the information gained in Chapter 2 to explore the preferential interaction between PCPDTBT and PCBM in functioning OPV cells. Raman intensity imaging of PCPDTBT:PCBM and PCPDTBT:PCBM:ODT solar cells yields information about the preferential interactions between the polymer donor and acceptor moieties and the fullerene, as well as morphological information about the polymer and PCBM domains in blend thin films. Although optical microscopy images of these blend thin films show no visible signs of phase segregation, Raman images reveal an interpenetrating network of polymer- and PCBM-rich domains as revealed by other AFM

studies of these blends. Raman intensity images also reveal correlations between high acceptor moiety activity and high PCBM activity at lower excitation energies, suggesting enhanced charge transfer to the fullerene from the acceptor moieties. Raman frequency images provide additional insights into these interactions and suggest that lower energy excitation allows relatively equal interaction between the polymer donor and acceptor moieties and PCBM, which may help explain the higher photocurrent production at longer wavelengths. Photocurrent imaging of a PCPDTBT:PCBM:ODT device supports this, and shows areas of higher photocurrent production in well-blended regions of the film.

In Chapter 4, the interactions between PCPDTBT and the small molecule electron acceptors DDQ and F_4-TCNQ are explored using absorption and Raman spectroscopies and density functional theory calculations. Spectroscopic results suggest that even with very low (0.1 weight %) concentrations of DDQ and F_4-TCNQ incorporated into thin films of PCPDTBT, the polymer adopts a more ordered and extended morphology. Raman spectra of doped PCPDTBT films suggest preferential interaction between DDQ and F_4-TCNQ and the BT acceptor moiety on the polymer backbone. Density functional theory calculations provide additional insight into these interactions and give an indication of the extent of wavefunction overlap between the polymer and DDQ and F_4-TCNQ, and degree of charge transfer between the polymer and dopant molecules.

Chapter 5 gives descriptions of sample preparation, equipment, and experimental setups used in collecting the data presented in this dissertation.

2. Spectroscopic Investigation of PCPDTBT:PCBM Blends

Polymer conformation exerts a strong influence over its optical and electronic properties and, in turn, the performance of the OPV cell in which it operates. Absorption spectroscopy is employed to investigate conformational changes in PCPDTBT in blends with PCBM and ODT, and in nanoparticles. Changes in the absorption lineshape can reveal a great deal of information about the extended or collapsed polymer morphologies in solution, nanoparticles, and thin films. Another goal is to gain an understanding of the interactions and resulting changes in vibrational modes PCPDTBT exhibits with varying energies of incident photons. Raman spectroscopy is employed to examine the response of the major PCPDTBT vibrational modes to excitation energies spanning its absorption from the NIR to near-UV. Density functional theory calculations provide a means to assign the major PCPDTBT Raman modes and provide more insight into the nature of wavefunction localization in the ground and excited states.

2.1 Background

The conformation a polymer adopts can have dramatic effects on its optical absorption and charge transport characteristics. As such, examining absorption spectra can reveal a considerable amount of information about polymer morphology and aggregation schemes in solutions and thin films.[72-76] For example, more planar, extended polymer conformations show red-shifted absorption maxima due to increased conjugation lengths and exciton coherence lengths. Conversely, highly disordered polymer chains typically display blue-shifted absorption peaks. Understanding these morphologies and

the conditions under which they are formed can yield insights into why a polymer performs as it does in functioning solar cell devices. Examining thin films and nanoparticles of PCPDTBT along with PCPDTBT:PCBM and PCPDTBT:PCBM:ODT blends, we observe indications of the significant changes in polymer morphology in these blends and nanostructures.

Accurate control of material morphology is necessary for optimizing performance. In addition to post processing techniques such as annealing, solvent additives that selectively solvate one blend component to promote phase separation are widely used. Alkanedithiols are especially well suited for this purpose and lead to significant improvements in overall PCE values, presumably from suppressed charge recombination due to a reduction of polymer/fullerene interfacial contacts.[49,77-79] Interestingly, optical absorption spectra of PCPDTBT:PCBM blends show pronounced red-shifts upon blending and treatment with 1,8-octanedithiol (ODT) suggesting enhanced polymer aggregation (phase segregation).[23,24,80,81] However, the lack of crystallinity in PCPDTBT limits access to important structural information. For example, Peet et al. reported broad, undefined diffraction patterns for PCPDTBT:$PC_{71}BM$ thin films processed with and without alkane dithiols.[24] In another study, Rogers et al. have reported crystal correlation lengths from ~7 to 11 nm in PCPDTBT thin films processed with and without additives in the π-π stacking direction, and correlation lengths roughly 4 nm longer in the alkyl stacking direction.[82] Furthermore, excited state electronic structures are highly complicated in d/a co-polymers from closely overlapping and interacting excited states with appreciable densities that give rise to congested spectral signatures. [58,83-85]

2.2 Absorption Spectroscopic Studies

Figure 2.2.1 shows optical absorption spectra for a spin-cast film of pristine PCPDTBT, PCPDTBT nanoparticles, and thin films of a 1:2 (w:w) blend of PCPDTBT:PCBM and a 1:2:3 (w:w:w) blend of PCPDTBT:PCBM:ODT. The pristine polymer and blend films show two distinct absorption maxima characteristic of donor-acceptor copolymers.[24,83,84,86-89] Arrows in Figure 2.2.1 b) indicate positions of Raman excitation wavelengths relative to the absorption spectra (discussed in Section 2.4). The blend spectrum shows a characteristic absorption peak for PCBM around 330 nm, and a slight shoulder at 434 nm from the relatively small PCBM absorption peak at that wavelength. As with earlier studies, the PCPDTBT:PCBM blend spectrum shows a red-shifted low-energy peak that can be attributed to increased phase separation between the polymer and fullerene acceptor. This new transition becomes enhanced in films treated with ODT, demonstrating increased ordering within PCPDTBT domains, presumably from increased PCBM aggregation. The pristine PCPDTBT nanoparticle spectrum shows a broadening of the low-energy peak in addition to new transitions appearing in the higher energy region that are absent in pristine and blend thin films (Fig. 2.2.1 (a) green trace). We propose these new transitions originate from disordered polymer chains as a result of rapid agglomeration into nanoparticles in the chloroform/water/surfactant solution. It is noteworthy that solution phase absorption studies of the pristine PCPDTBT system do not exhibit these features suggesting that conformations in thin films retain the same structural characteristics as in solution. The presence of the low energy shoulder near the absorption onset region in PCPDTBT nanoparticles indicates that minority ordered domains or extended chains persist that allow more inter- and intra-chain

electronic communication within these domains, as in the blend films with ODT. The prominent red-shifted absorption feature that increases in strength upon addition of PCBM and treatment with ODT is consistent with previous assignments of enhanced local order within polymer domains. Some groups have attributed this feature to PCPDTBT aggregates implying greater interchain electronic communication. However, the bulky nature of the alkyl side groups, which normally impede these interactions, may suggest otherwise. Gélinas et al. presented absorption spectra for the closely related small molecule, 7,7'-(4,4-bis(2-ethylhexyl)-4H-silolo[3,2-b:4,5-b']dithiophene-2,6-diyl)bis(6-fluoro-4-(5′-hexyl-[2,2'-bithiophen]-5-yl)benzo[c][1,2,5] thiadiazole) (p-DTS(FBTTh$_2$)$_2$), that show features very similar to those of PCPDTBT.[25] The more resolved low-energy vibronic progression observed for this molecule was shown through transmission electron microscopy (TEM) and grazing incidence wide angle X-ray scattering (GIWAXS) analysis to be a function of increased ordering by Love et al. when DIO was added to their blends.[90] Vacha et al. also presented intriguing results from single molecule d/a surrogates of polymers where they demonstrated the importance of the twist angle between d/a chain segments (intrasegment configuration) and its impact on intersegment (d/a) interactions.[91] They showed that as the D/A twist angle decreases, improved electronic communication along the chain leads to increased charge transfer character and spectral red-shifts. However, electron densities in the excited state tend to be localized mostly on the BT acceptor units, similar to experimental and theoretical results on related d/a systems. Because absorption probes the excited state potential landscape, the red-shifted absorption feature can be most readily attributed to transitions centered on the BT units. In this picture, the red-shifted absorption feature probably

originates from more ordered PCPDTBT chains. Closer inspection of this lineshape reveals a small dip, possibly corresponding to either a partially resolved vibronic progression or a distinct electronic state. Based on previous studies, the latter can be effectively ruled out. On the other hand, the higher energy transitions largely maintain similar lineshapes regardless of the processing method used. The insensitivity of these features is consistent with localized transitions probably centered on the CPDT unit of the PCPDTBT monomer.

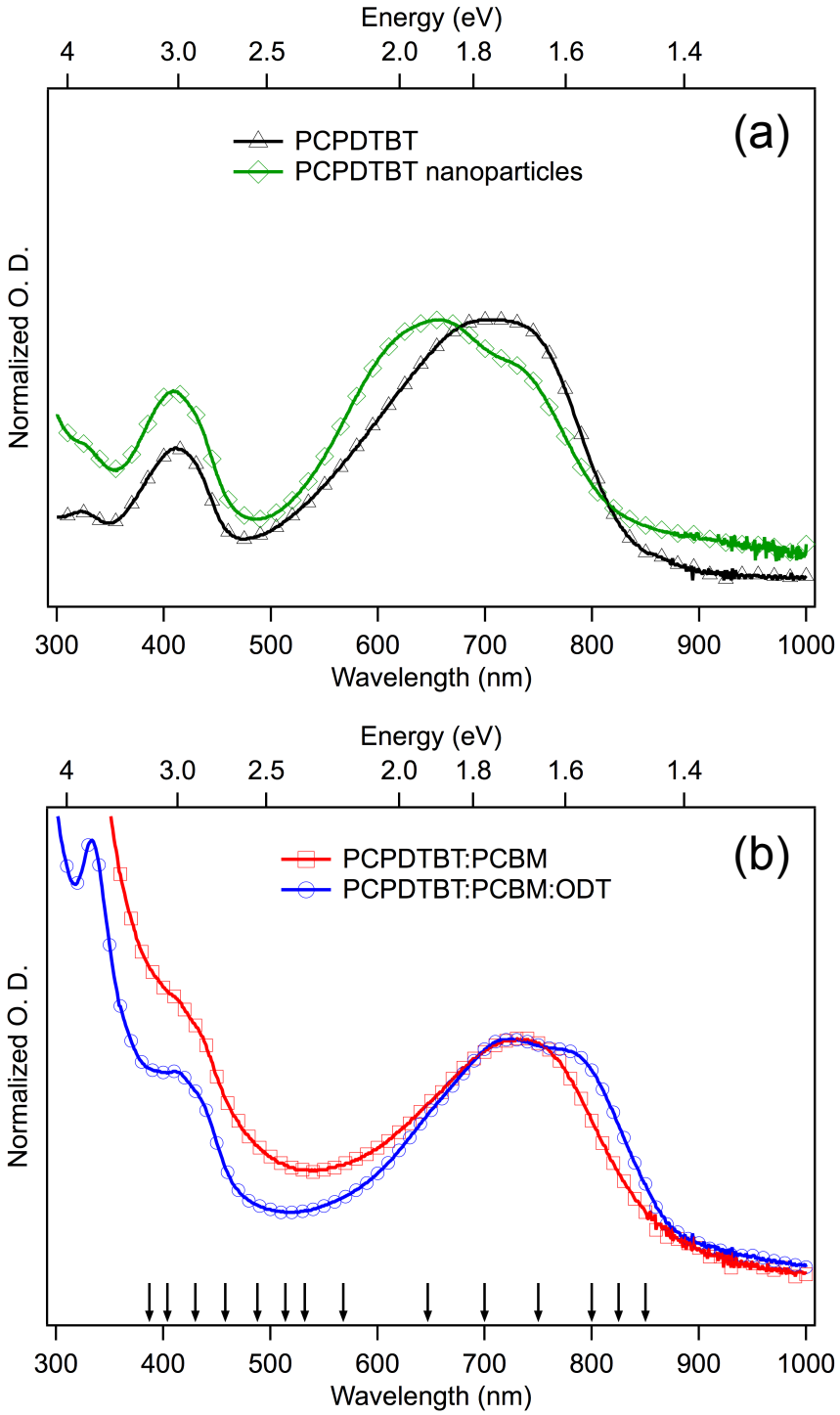

Figure 2.2.1. Normalized optical density vs. wavelength of (a) pristine PCPDTBT thin film and nanoparticles, and (b) thin films of PCPDTBT:PCBM (10:20 mg/ml) and PCPDTBT:PCBM:ODT (10:20:30 mg/ml). Arrows in (b) indicate positions of excitation wavelengths used for Raman experiments.

2.3 Photoinduced Absorption

Steady-state photoinduced absorption (PIA) of pure PCPDTBT films was also measured to assess the presence of other excited states. The spectra show a broad band appearing at ~850 nm and extending into the near infrared when exciting at 405 and 650 nm. Distler et al. have attributed a lower-energy (~1300 nm) photoinduced absorption peak to a $T_1 \rightarrow T_n$ transition in pristine PCPDTBT following intersystem crossing from the S_1 state.[92] The band we observe starting at 850 nm may be a result of absorption into higher-energy singlet states localized on the BT moiety. The similar features in the PIA spectra collected at room temperature and 11K suggest that pristine polymer conformations, and therefore energetics, do not change appreciably upon cooling. The apparent stronger sensitivity of the BT units to polymer conformation and packing is further explored using resonance Raman spectroscopy in Section 2.4.

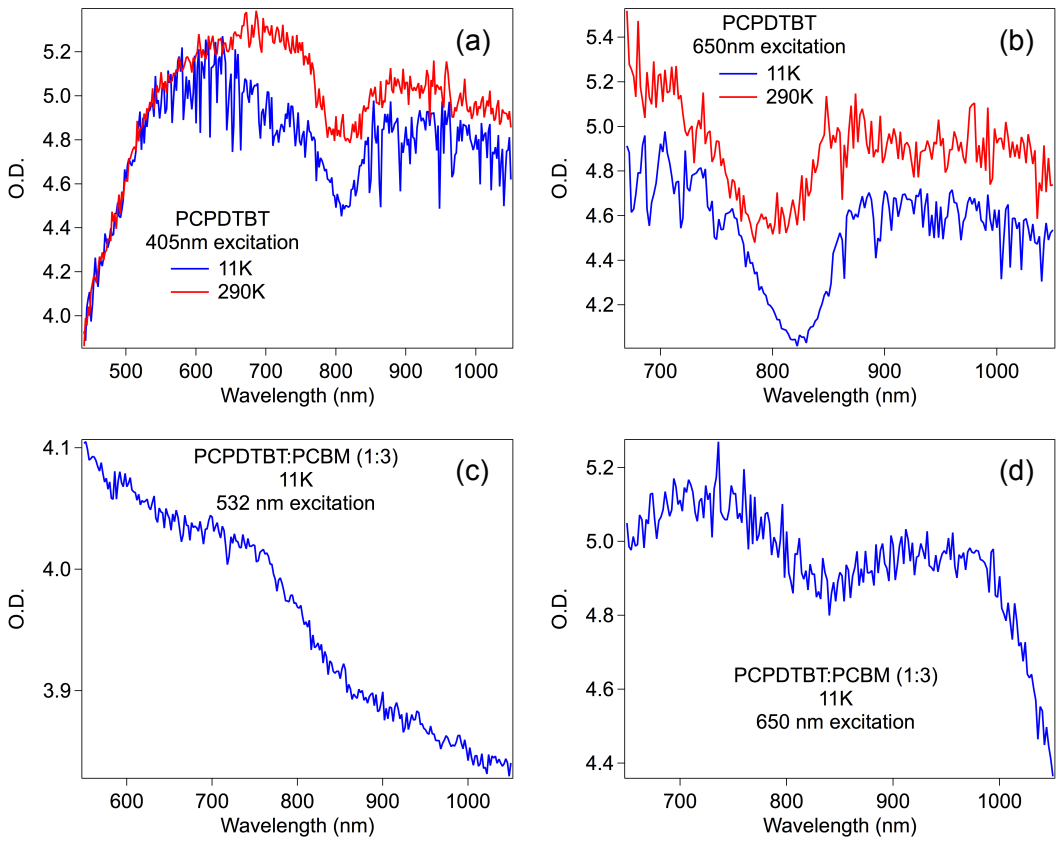

Figure 2.3.1. Photoinduced absorption of PCPDTBT films at a) 405 nm and b) 650 nm excitation at 11K and 290K, and for PCPDTBT:PCBM (1:3) blend films at 11K at c) 532 nm and d) 650 nm excitation.

2.4 Raman Spectroscopic Studies

Many of the limitations imposed by conventional one-photon spectroscopies to probe specific interactions between D/A monomer units of PCPDTBT and with fullerenes can be overcome using two-photon scattering spectroscopic techniques, such as resonance Raman spectroscopy. Raman transitions originate and terminate on well-defined, but different, vibrational levels of the ground electronic state, resulting in chemically specific views of polymer structure and conformation as well as sharp spectral signatures. By tuning excitation energies on resonance with intermediate (excited) states, the non-stationary vibrational wavepacket (i.e., ground state vibrational wavefunction)

samples the excited state(s) potential surface(s) before returning to the ground state. Strong enhancements of Franck-Condon active vibrations usually result from systems with large absorption cross-sections (i.e., conjugated polymers), which provide detailed views of the mode-specific geometrical rearrangements over the excited state potential landscape. Raman processes are also highly sensitive to the local environment of the resonant chromophore giving this technique an additional advantage for elucidating the role of ground state structure and interactions on excited state photovoltaic processes. Reish et al. applied resonance Raman spectroscopy techniques to study the related D/A alternating co-polymer, poly[N-1-octylnonyl-2,7-carbazolealt-5,5-(4′,7′-di-2-thienyl-2′,1′,3′-benzothiadiazole)] (PCDTBT), blended with PCBM and found that Raman patterns changed drastically with excitation energy, indicating conformation-dependent charge transfer character along the chain (i.e., d/a orientation).[22] Additionally, these authors performed nanosecond transient absorption spectroscopy measurements on a series of d/a derivatives using heavy atom substitution and also found a significant dependence of the relaxation timescales with atomic mass, indicating contributions of spin-orbit coupling that are also sensitive to backbone structure and conformation.

Figure 2.4.1 shows Raman spectra for a PCPDTBT:PCBM (1:3 wt:wt) blend film between 1100 cm^{-1} and 1700 cm^{-1} collected at excitation wavelengths from 387 to 850 nm. All Raman spectra are scaled by dividing intensities by absolute energies in order to remove dependence on excitation energies. Due to the lack of a suitable intensity standard for all experimental setups, spectra are normalized to the 1342 cm^{-1} peak to allow for comparisons in relative intensities between Raman modes. Similar comparisons have been made for Raman spectra of related and other d/a co-polymers in

lieu of a non-absorbing intensity standard.[43,93,94] Background fluorescence is especially strong in pristine PCPDTBT thin films, but is efficiently quenched by PCBM. Unfortunately, large background levels in pristine film Raman spectra preclude comparisons to PCBM blends.

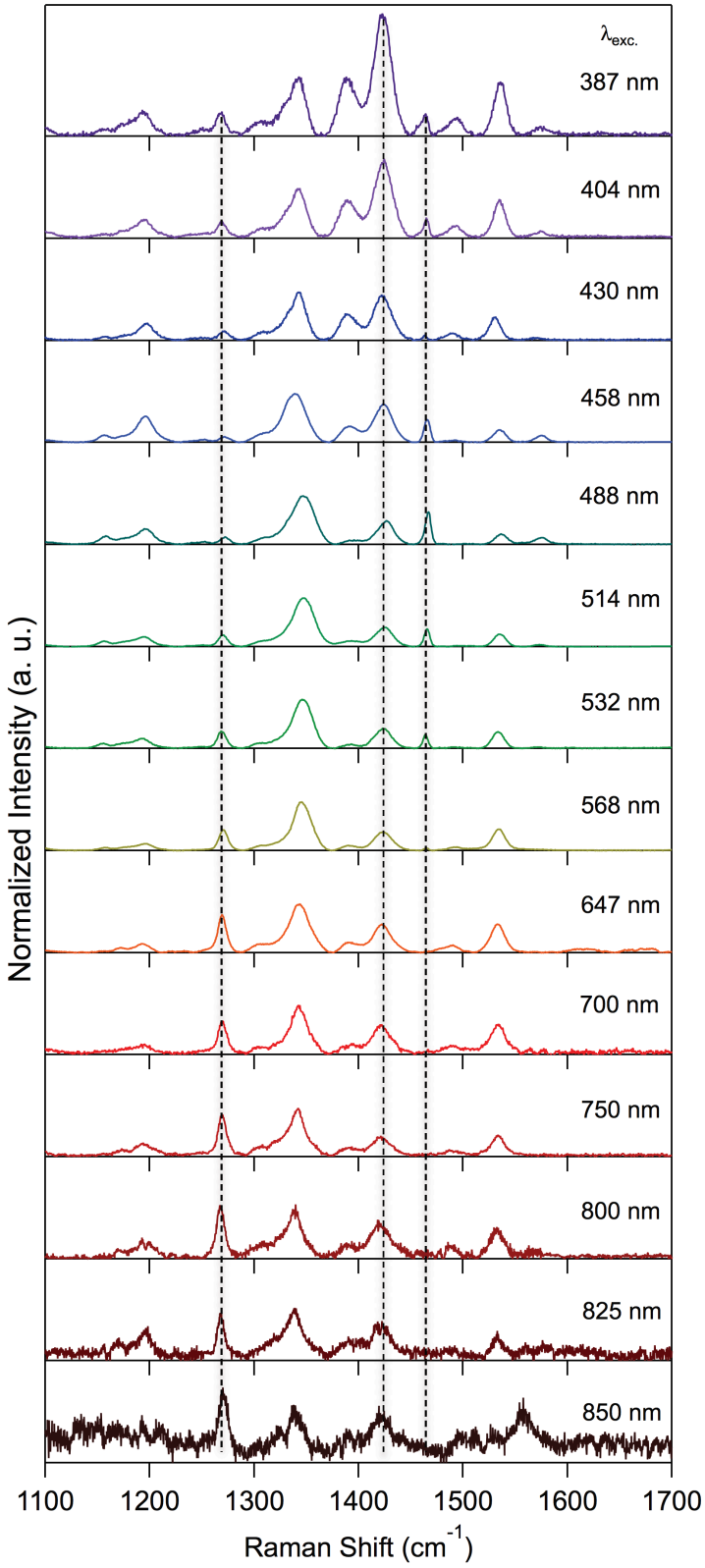

Figure 2.4.1. Raman spectra for PCPDTBT:PCBM (1:3 w:w) at excitation wavelengths from 387 to 850 nm. Intensities are normalized to the 1342 cm^{-1} mode of PCPDTBT.

The relatively large number of Raman active modes and their dependence on excitation energy is consistent with the appearance of a weakly resolved vibronic progression in absorption spectra, namely, multiple overlapping progressions over a broad frequency range. We performed density functional theory (DFT) simulations of Raman spectra using CPDTBT oligomers to first establish a basis for comparing specific vibrations to d/a units as well as their orbital parentage (see Section 2.5). Previous Raman studies of related polymers, such as poly(9,9-di-n-octylfluorene-*alt*-benzothiadiazole) (F8BT) and PCDTBT, show similar trends as observed in Figure 2.4.2 and we use these as a guide for assigning modes of PCPDTBT. Previous studies of F8BT identified the fluorene ring symmetric stretching mode at 1608 cm^{-1} and the BT ring stretch at 1545 cm^{-1}.[59] Reish et al. have provided assignments for the Raman modes displayed by PCDTBT such as the BT C—H wag coupled with the thiophene C—H wag at 1374 cm^{-1}, the thiophene ring stretching mode coupled with a thiophene and carbazole C—H wag at 1447 cm^{-1}, the BT symmetric C—H wag coupled with a thiophene asymmetric C—H wag at 1541 cm^{-1}, and the carbazole ring stretching mode and its coupled C—H wag at 1623 cm^{-1}.[84] The lower-frequency Raman modes at 844 and 874 cm^{-1} are tentatively assigned by these authors to in-plane bending modes of the dithiophene benzothiadiazole group. In their study of PCDTBT, Reish et al. found increased BT intensity when excitation light is resonant with the low-energy absorption peak whereas excitation light resonant with the high-energy absorption peak of PCDTBT showed greater activity of donor carbazole units. In a related study, Provencher et al. identified BT in-plane C—H wags at 1262 and 1260 cm^{-1} for the PCDTBT cation and

neutral molecules, respectively.[95] Because PCPDTBT/PCBM charge transfer interactions are weak in the ground electronic state, we observe no corresponding contributions from these species.

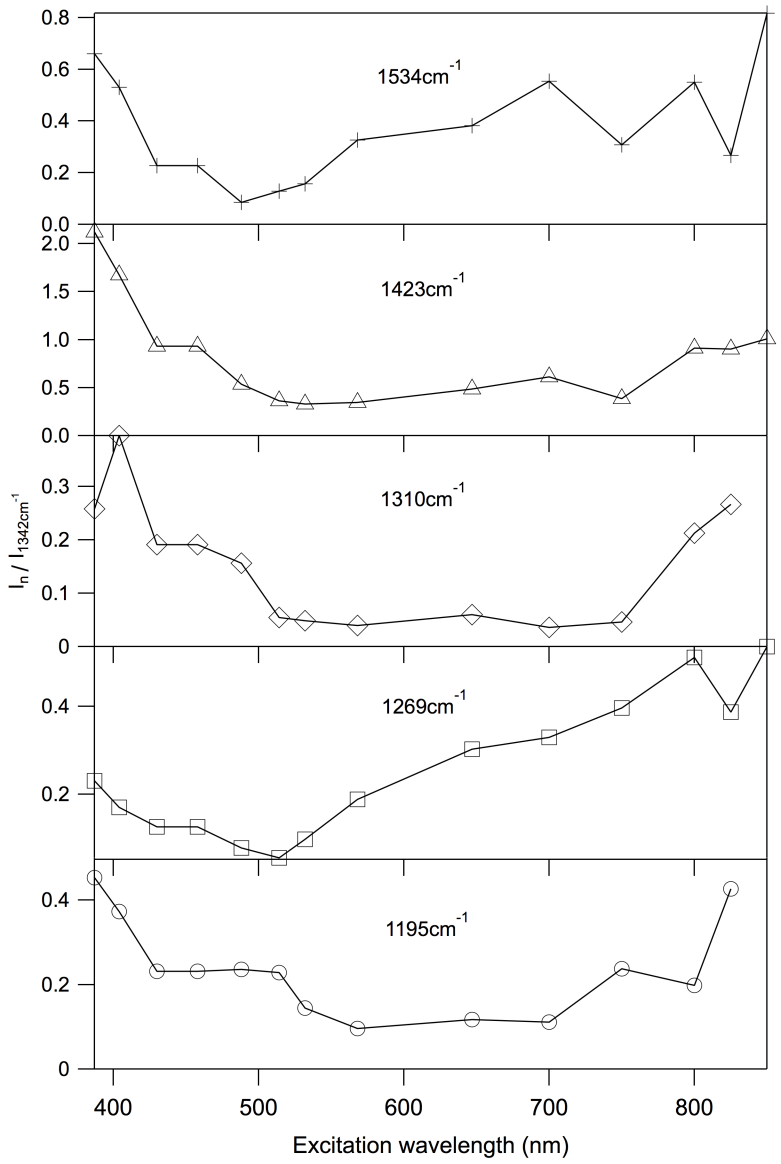

Figure 2.4.2 Relative intensities of PCPDTBT skeletal vibrations as a function of excitation wavelength.

Examining the vibrational mode trends in PCPDTBT (Figure 2.4.2), we see good general agreement between the mode intensities and the absorption profile. The reader is referred to Table 2.5.1 for PCPDTBT vibrational mode assignments. The CPDT in-plane C—H wag coupled with the BT symmetric C—H wag at 1195 cm^{-1}, in particular, shows good agreement with the absorption profile, which suggests charge density is delocalized over several d/a units. Interestingly, the 1423 cm^{-1} mode, assigned to the CPDT C—C stretch, shows large increases in relative intensity for increasing excitation energies, suggesting greater localization on this unit, which is consistent with PCBM induced d/a twisting in a mixed phase. Conversely, the 1269 cm^{-1} and 1534 cm^{-1} modes, assigned to the BT symmetric in-plane C—H wag and C-C stretch, respectively, decrease in relative intensity with higher excitation energies. Most importantly, the 1269 cm^{-1} BT C—H wag mode shows very little relative intensity at higher excitation energies but increases dramatically toward the NIR region corresponding to the red-shifted component in optical absorption spectra of blends. Despite the qualitative nature of these trends, they confirm our expectations of structure-induced delocalization over d/a units in PCPDTBT blends. For example, a higher energy mixed phase results in chains that are more localized in nature as opposed to a lower energy phase-separated morphological component where chains are more ordered leading to greater charge transfer character.

We now turn our attention to the main backbone vibrations displaying the largest intensities in resonance Raman spectra (i.e., modes with the largest Franck-Condon displacements in the excited state). The 1342 cm^{-1} mode corresponding to the BT in-plane “concert wave” C—H wag shows the least sensitivity over all excitation energies used in Fig. 1.2. Beginning at higher excitation energies, we observe larger activities of

the C=C stretches localized on the CPDT units (1423 cm^{-1}). The CC symmetric stretch mode of PCBM is also observed at ~1466 cm^{-1} in the range of 387 – 532 nm excitation, which is expected since it has larger oscillator strength at higher energies. As excitation energies decrease, approaching resonance with the main PCPDTBT absorption band, Raman transitions localized on the BT units become more prevalent (i.e., larger relative intensities), although CPDT bands are still discernible. Because only the low energy region of the PCPDTBT absorption spectrum is affected by PCBM and ODT, this behavior may be due to increased planarization of the polymer backbone d/a units and increased delocalization of the wavefunction between the BT and CPDT groups, as noted in earlier reports of related d/a co-polymers.[59,91] Decreasing excitation energies results in lower intensities of CPDT-centered vibrations and increasing intensities of the BT unit, most notably the 1269 cm^{-1} in-plane C—H wag.

2.5 Density Functional Theory Calculations

In the present study, DFT simulations are carried out using several functionals including CAM-B3LYP, OPBE, and B3LYP to calculate Raman spectra for CPDTBT trimers with abbreviated side chains. We found that the B3LYP functional with the 6-311(d) basis set provided relatively good agreement with experimental frequencies and intensities. It is also interesting to note that reduction of exchange energies led to substantial deviations from the experimental results in Fig. 1.3.1 suggesting excitons are more localized in character (see Figure 2.5.1 below). Vibrational mode assignments for the CPDTBT trimer using the B3LYP functional are given in Table 2.5.1.

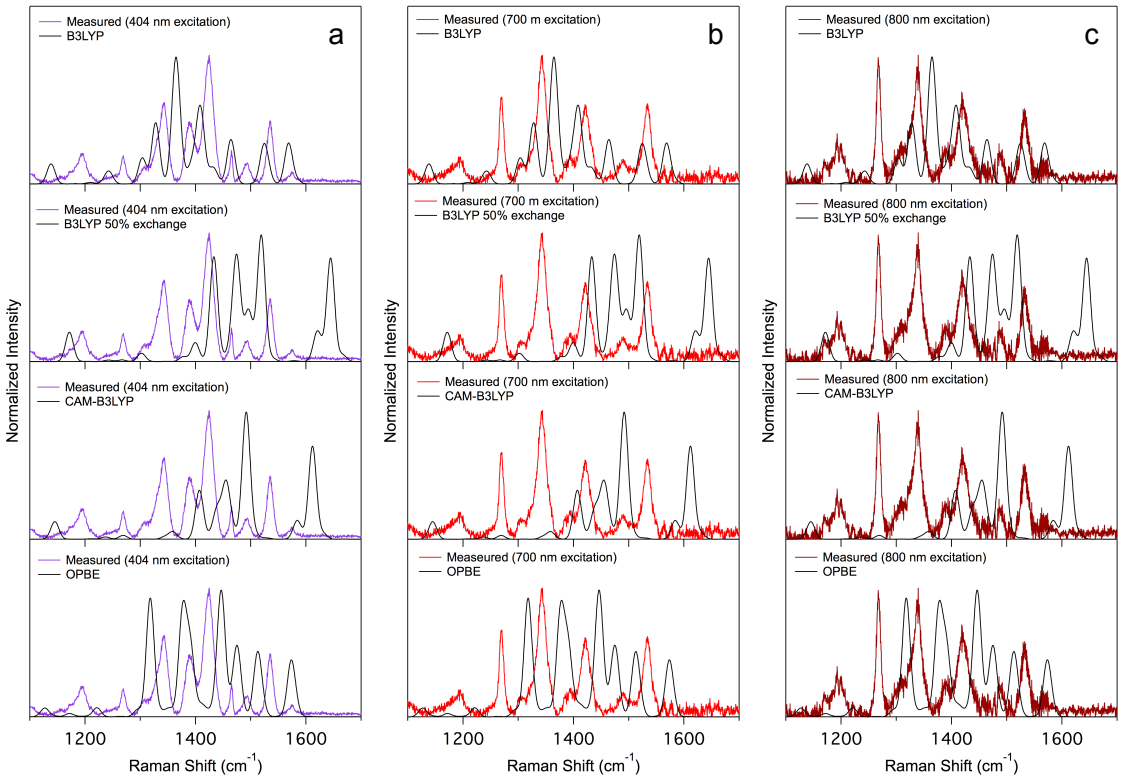

Figure 2.5.1. Calculated Raman spectra using B3LYP, B3LYP with reduced exchange energy, CAM-B3LYP, and OPBE functionals compared with measured PCPDTBT:PCBM (1:3) spectra at a) 404 nm, b) 700 nm, and c) 800 nm excitation wavelengths.

Table 2.5.1. Raman mode frequencies and vibrational modes for the CPDTBT trimer.

Peak	$\hbar\omega$ (cm^{-1})	Assignment	
n_1	1156		
n_2	1195	CPDT in-plane C-H wag coupled + BT symmetric C-H wag	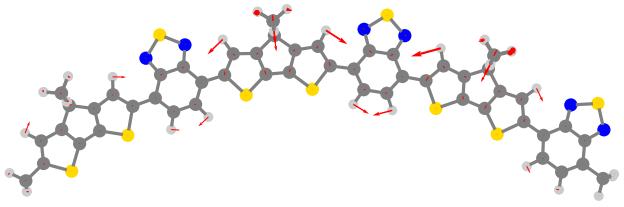

n_3	1269	BT symmetric in-plane C-H wag	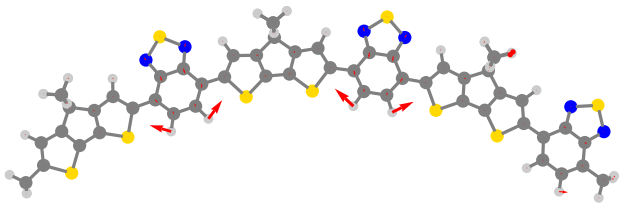
n_4	1310	BT C=C coupled with C=N stretch and in-plane H wag	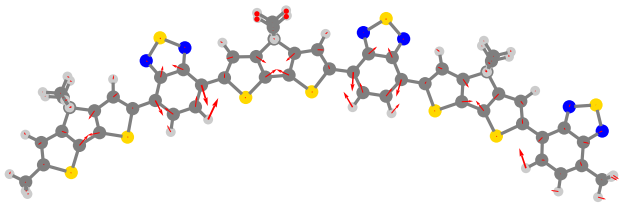
n_5	1342	BT in-plane "concert wave" C-H wag	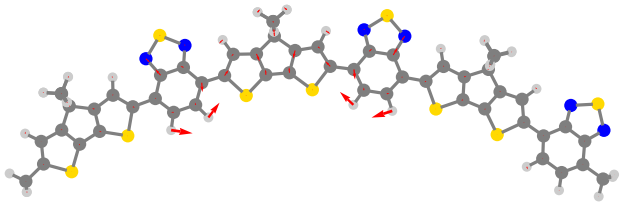
n_6	1391		
n_7	1423	Dithiophene C-C stretch	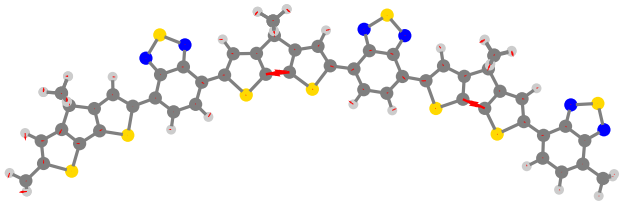
n_8	1466	PCBM	
n_9	1492		
n_{10}	1534	BT C-C stretch coupled with in-plane symmetric C-H wag	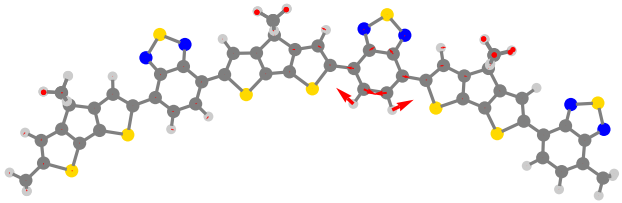
n_{11}	1575	PCBM	

HOMO and LUMO level iso-surfaces are calculated and shown in Fig. 2.5.2 for a 0.01 isovalue. Similar to other computational studies of donor-acceptor copolymers, our calculations show relatively delocalized electron densities in the HOMO and more localized densities in the LUMO, specifically on BT units even when backbone d/a orientations are fixed in a planar conformation.[58,59,84,96] Provencher et al. showed similar

results for PCDTBT, with increased wavefunction localization on the BT acceptor moiety in the LUMO for the neutral species.[95] Likewise, in F8BT, when the F8 (donor) and BT (acceptor) moieties are coplanar, calculations show increased localization in the LUMO state compared to the HOMO.[59,97,98] When the plane of the BT group is perpendicular to the plane of the F8 groups, however, almost complete localization of the wavefunction occurs on the F8 groups in the HOMO and on the BT group in the LUMO. Although we did not investigate the effects of torsional angle between the CPDT and BT moieties in our calculations, it may be reasonable to assume that an increase in torsional angle between moieties in PCPDTBT would result in increased localization of the wavefunction in the ground and excited states. Delocalization of charge densities on HOMO levels indicates good charge transfer between d/a units, which may provide a lower energy barrier pathway for charge transfer from the polymer to fullerene acceptors in functioning solar cell devices due to reduced reorganization energies. This view is similar to the one proposed by Grancini et al. who suggested that larger electronic coupling between higher energy PCPDTBT exciton states and charge separated states can overwhelm reorganization energies, making hot exciton dissociation possible.

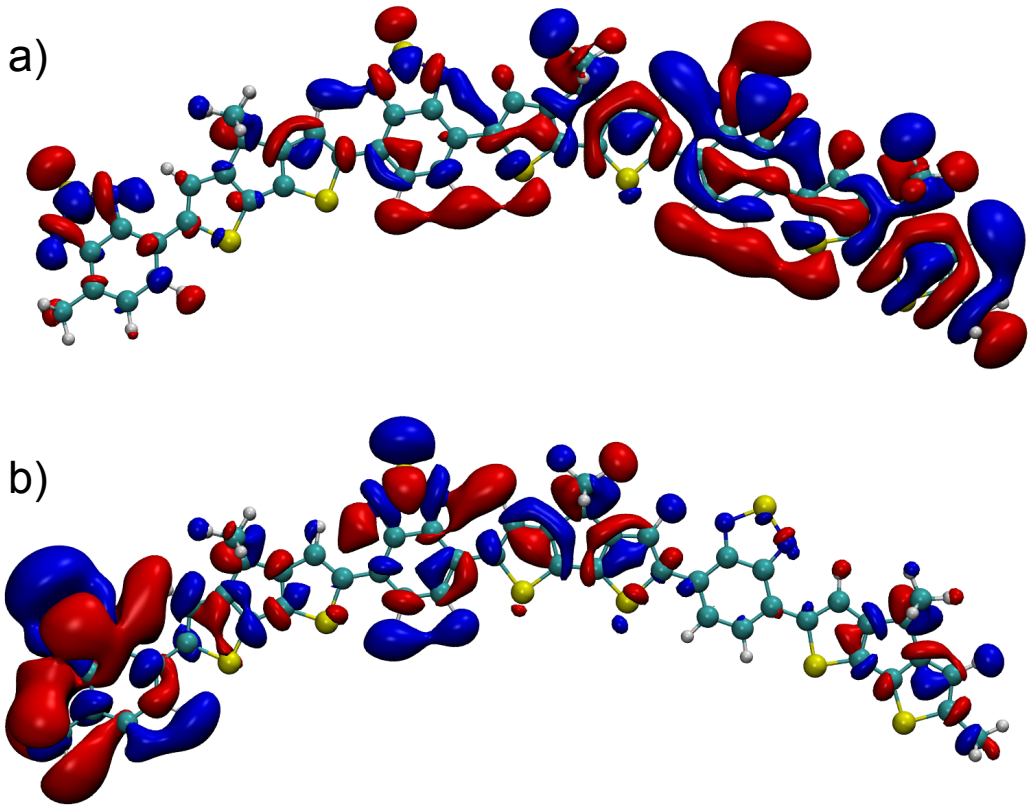

Figure 2.5.2. Electron density isosurfaces for the a) HOMO and b) LUMO of the PCPDTBT trimer at isovalues of 0.01.

Similar to previous reports, our DFT results are consistent with the view of strong charge transfer character amongst the donor-acceptor repeat units of the PCPDTBT backbone. The optimized geometry calculated for the PCPDTBT trimer is arched as a result of the bonding arrangement on either side of the CPDT groups, and is essentially planar. These results correlate well with those calculated by Risko et al. who showed a planar, arc-like conformation for a tetramer of PCPDTBT, with a near-zero twist angle between the CPDT and BT groups.[99] CPDTBT trimers with a PCBM molecule over the CPDT and BT group were also optimized that show a slightly distorted polymer geometry with the plane of the polymer backbone bending very slightly around the

fullerene, as in Figure 2.5.3. In these optimized arrangements, the physical separation between the trimer and PCBM when PCBM is placed over the BT group is 3.65 Å and the separation when the PCBM is over the CPDT group is 5.15 Å. The increased distance between the trimer and PCBM with PCBM over the CPDT group may be due to reduced interaction between PCBM and the trimer backbone and steric hindrance with the abbreviated trimer side chains. We also see slightly more bending of the trimer backbone when the PCBM is placed over the BT group compared to over the CDPT group, which suggests increased electronic interaction with the trimer backbone in this arrangement. Thus far, DFT and spectroscopic results demonstrate that short-range ordering and chain conformation characteristics exert the greatest influence on optical and electronic properties.

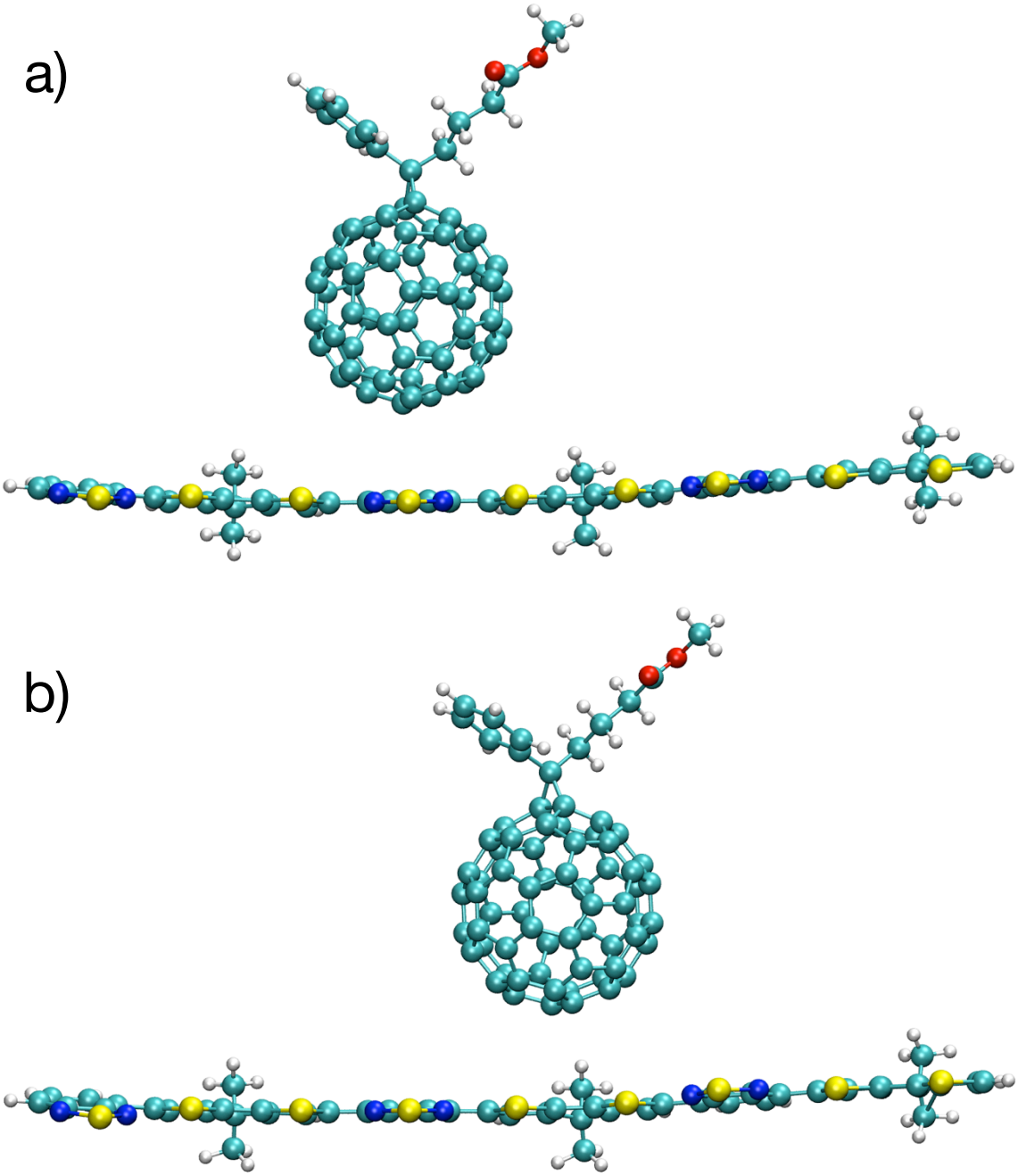

Figure 2.5.3. Optimized geometries for a CPDTBT trimer with PCBM over a) the BT group and b) the CDPT group.

Vacha and co-workers used single molecule fluorescence and excitation spectroscopy on small d/a molecules processed in different solvents to tune d/a twist

angles.[91] They demonstrated that large modulation of emission and absorption energies occurs where a greater twist angle results in blue-shifted spectra and greater localization on individual d/a segments. Intrasegment communication (within the same d/a molecule) improves with planarity leading to red-shifted spectra and intensity redistributions within the optical line shapes. Because PCPDTBT alkyl side groups likely inhibit significant interchain exciton coupling interactions observed in conventional π-stacked aggregate structures,[24,82] we propose that red-shifted absorption features in PCPDTBT blends with PCBM arise from more elongated and planarized chains with greater intrachain charge transfer character. Comparison of relative intensities of Raman modes with varying excitation energies also revealed that the 1269 cm^{-1} mode of the BT unit has larger excitation efficiency toward the red edge of the absorption spectrum. These results are consistent with recent reports of PCBM-induced polymer aggregation although this effect appears to promote greater intrachain communication as opposed to the more commonly observed interchain exciton coupling in well-ordered aggregates.

3. Spectroscopic and Photocurrent Imaging Studies of PCPDTBT:PCBM Blends

The spectroscopic results presented in Chapter 2 give us important information about the morphological changes PCPDTBT undergoes when blended with PCBM and ODT, and formed into nanoparticles, as well as how the vibrational modes of PCPDTBT respond to varying excitation energies. Although charge transfer between PCPDTBT and PCBM has been discussed widely in the literature, there is little discussion of the preferential interaction between PCPDTBT and the fullerene in blended thin films. In this chapter, we seek to apply the information from the previous chapter while investigating the preferential electronic interactions between PCPDTBT and PCBM. To this end, we employ Raman intensity and frequency imaging and the assignment of specific Raman vibrational modes to either the donor (CPDT) or acceptor (BT) moieties from Chapter 2. We also explore the effect of low and high excitation energy on the photocurrent produced by solar cells made from a blend of PCPDTBT, PCBM and ODT.

3.1 Raman Imaging of PCPDTBT:PCBM blends

We extend our studies from Chapter 2 to resonance Raman and photocurrent imaging of PCPDTBT:PCBM blends in functioning solar cells to understand how polymer structure is affected by local morphology, and examine the interactions between PCBM and the donor and acceptor moieties on the polymer backbone. A key objective of these measurements is to spatially correlate PCPDTBT conformational and packing characteristics within distinct morphological domains. Figure 3.1.1 shows Raman intensity images for a 10 × 10 μm area of a PCPDTBT:PCBM (1:2 w/w) solar cell device

excited with higher energy (458 nm) and lower energy (647 nm) excitation. All images in Fig. 3.1.1 are from the same area and pixel values represent integrated peak areas for the given modes normalized to the 1342 cm^{-1} acceptor C—H wag mode. Devices with this blend of polymer and PCBM showed no visible phase segregation under optical illumination after moderate annealing. However, Raman and photocurrent images (vide infra) show an interpenetrating type of morphology similar to previously reported AFM studies of these blends.[23,24,100] The region appearing toward the upper right of the image field of view shows diminished amounts of both PCPDTBT and PCBM indicating this feature is probably a defect and not representative of the bulk blend material. Under 458 nm excitation, the strength of the 1269 cm^{-1} BT mode is greatly diminished relative to the 1423 cm^{-1} CPDT C-C stretch, which follows from the excitation profile of the two modes (see Figure 2.4.2). Comparing the activities of the polymer donor and acceptor moiety modes, we see that in general, areas of high 1269 cm^{-1} BT activity correspond to areas with lower 1466 cm^{-1} PCBM activity, and areas with high 1423 cm^{-1} C—C stretch activity correspond to areas of high PCBM activity. This result is consistent with our proposed origin of the BT-centered NIR absorption transitions and the stronger sensitivity of BT vibrations to thin film processing conditions.

Additional views of the morphology-dependent blend landscape are obtained using 647 nm excitation, which is off-resonance with PCBM, and mostly reveal details of the polymer structure and variations due to local composition. We again find correlations between areas of high 1269 cm^{-1} mode activity and low PCBM activity. However, areas of high 1423 cm^{-1} intensity are not well-correlated with areas of high PCBM activity. Since Raman efficiencies decrease with lower excitation energies, we expect less

sensitivity of these modes to local morphology. Raman intensity images for the 1466 cm^{-1} PCBM mode are shown in Figure 3.1.3.

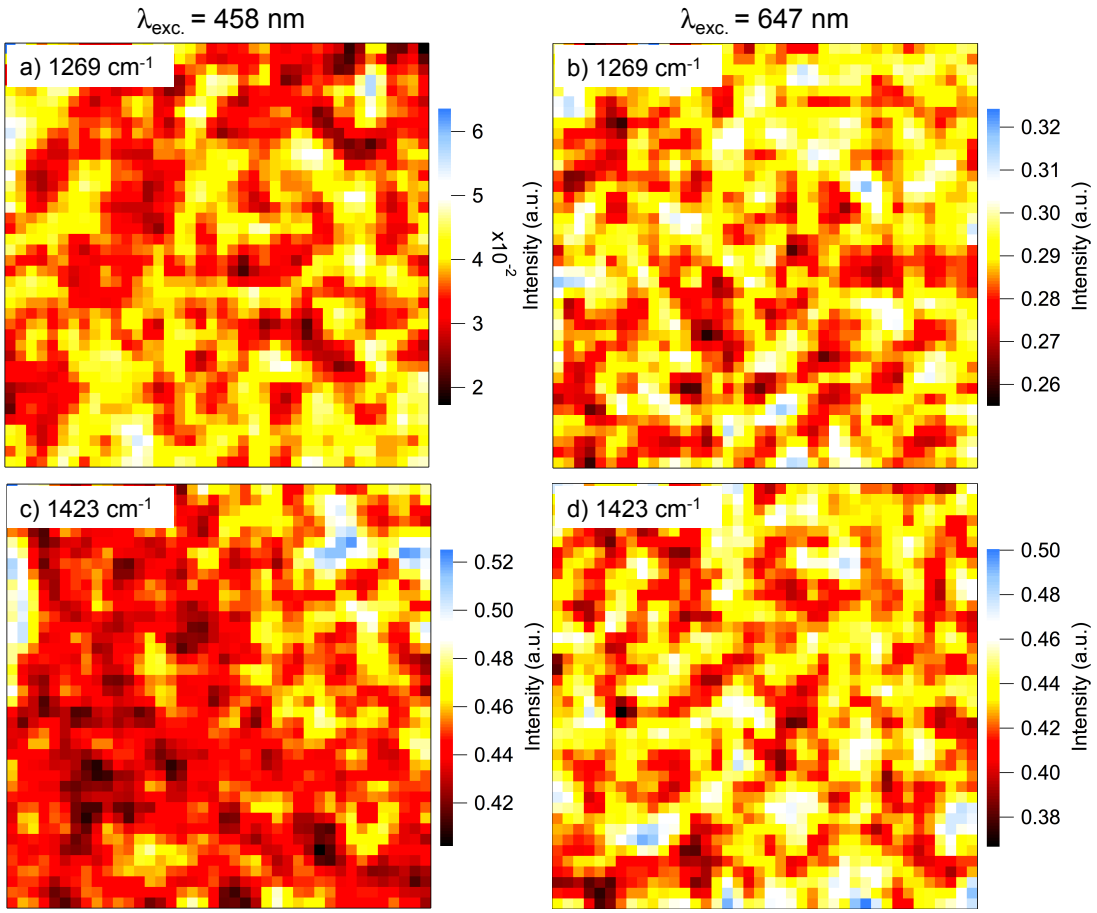

Figure 3.1.1. Raman intensity images of acceptor (a, b) and donor (c, d) moiety Raman mode intensities in PCPDTBT:PCBM (10:20 mg/ml) photovoltaic devices at 458 and 647 nm excitation. All images are of the same 10 × 10 μm area. Pixel values represent integrated peak areas. Intensities are normalized to the 1342 cm^{-1} acceptor mode. The PCBM signal is too weak to be distinguished from the background noise at 647 nm excitation.

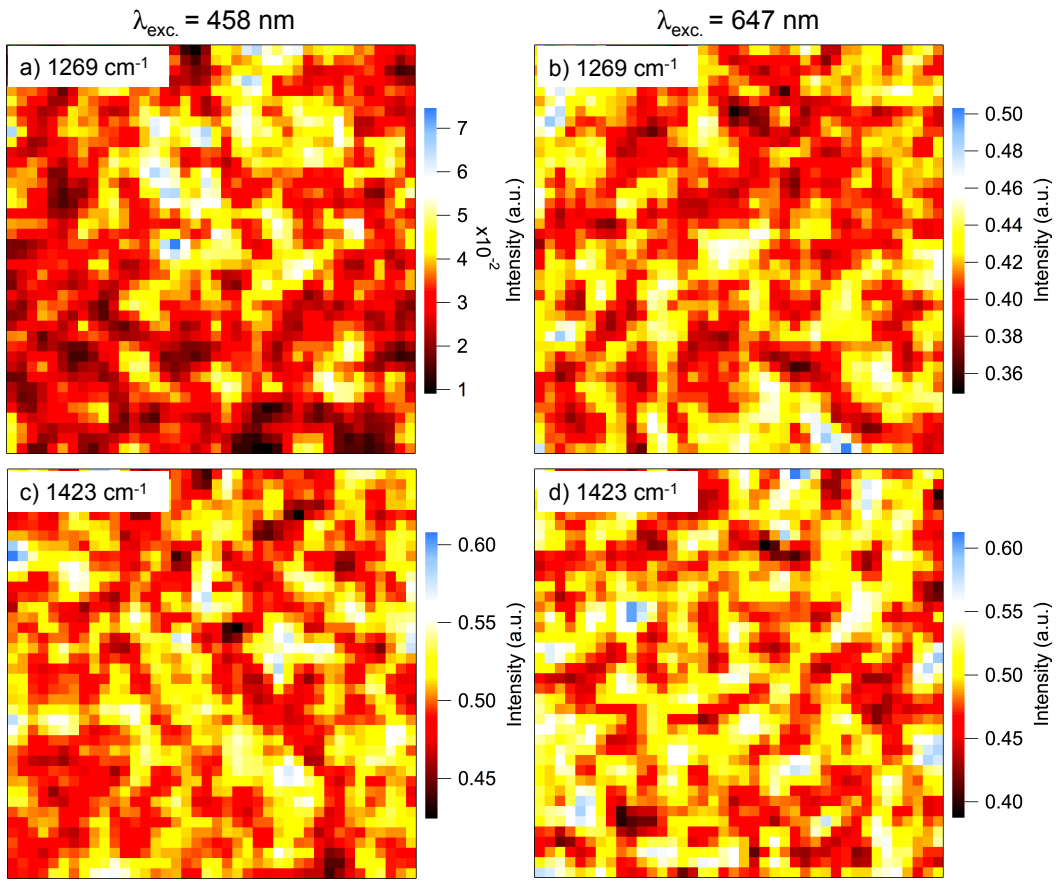

Figure 3.1.2. Raman intensity images of acceptor (a, b) and donor (c, d) moiety Raman mode intensities in PCPDTBT:PCBM:ODT (10:20:30 mg/ml) photovoltaic devices at 458 and 647 nm excitation. All images are of the same 10 × 10 μm area. Pixel values represent integrated peak areas. Intensities are normalized to the 1342 cm^{-1} acceptor mode. The PCBM signal is not discernible from the background noise under 647 nm excitation.

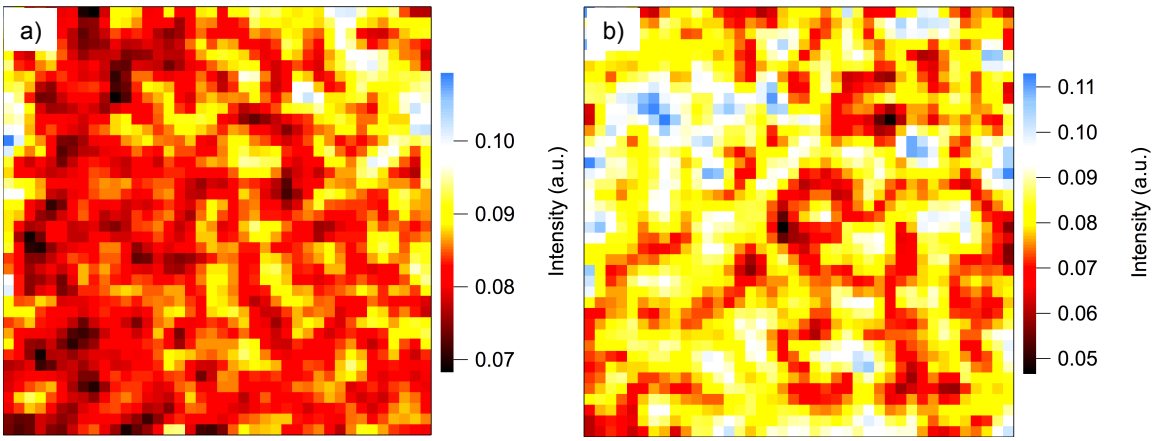

Figure 3.1.3. Raman intensity images of the 1466 cm^{-1} PCBM Raman mode at 458 nm excitation for a) PCPDTBT:PCBM (10:20 mg/ml) and b) PCPDTBT:PCBM:ODT (10:20:30 mg/ml). Images are of the same areas as in main article Figures 4 and 5, respectively. Pixel values represent integrated peak areas.

Figure 3.1.2 shows Raman intensity images for a 10 × 10 mm area of a PCPDTBT:PCBM solar cell device processed with ODT in the active layer blend. Similar to Fig. 3.1.1, all images are normalized to the 1342 cm^{-1} mode. A slightly larger degree of phase separation is apparent, but overall, the sizes of morphological features are similar to PCPDTBT:PCBM devices not treated with the additive. Under 458 nm excitation, the correlation between the 1269 cm^{-1} mode and PCBM activity is less pronounced than for the non-ODT device. This may be due to the very weak 1269 cm^{-1} signal at this wavelength in this blend. However, images generated with 647 nm excitation reveal areas of lower BT 1269 cm^{-1} activity adjacent to areas of higher 1466 cm^{-1} PCBM activity (at 458 nm excitation), suggesting increased charge transfer character between the polymer and PCBM. There is relatively good agreement between areas of high 1423 cm^{-1} C-C stretch activity and high PCBM activity. Under 647 nm excitation, the correlations between the polymer modes and PCBM activity are similar to the non-ODT device; with a fairly good correspondence between areas of high 1269 cm^{-1} activity and low PCBM activity, and less correlation between the donor moiety 1423 cm^{-1} mode and the PCBM mode.

3.2 Raman Frequency Imaging

Shifts in Raman mode frequencies can provide additional information about possible interactions between PCPDTBT and PCBM. Specifically, we can gain information about which moieties are interacting preferentially with PCBM under high- and low-energy excitation. Figures 3.2.1 and 3.2.2 show fitted Raman peak positions for the same areas as Figs. 3.1.1 and 3.1.2, respectively. As with the Raman intensity images under 458 nm excitation, it is difficult to make definitive correlations between the position of the 1269 cm^{-1} acceptor mode, for both ODT-free and ODT-containing devices, and PCBM concentration due to the weak signal strength of this mode at that wavelength. Similarly, there does not appear to be a strong correlation between regions of maximum red-shift and regions of higher PCBM activity for the 1423 cm^{-1} mode at this wavelength. Turning to the donor 1423 cm^{-1} mode, at 647 nm, we see that the area of maximum red shift correlates well with the area of highest PCBM Raman intensity. The acceptor moiety 1342 cm^{-1} in-plane "concert wave" C—H wag is much more intense at both 458 and 647nm, allowing for a better comparison between its position and PCBM activity. Figures 3.2.3 and 3.2.4 show comparisons between the acceptor 1342 cm^{-1} mode and the donor 1423 cm^{-1} mode at 458 and 647 nm excitation. At 458 nm, the 1342 cm^{-1} mode does not show a strong correlation between areas of maximum red shift and PCBM activity in the ODT-free device. However, like the 1423 cm^{-1} donor-centered mode, there is a strong correlation between areas where the 1342 cm^{-1} mode is most red-shifted and areas of high PCBM activity. These trends suggest that both the donor and acceptor moieties are interacting strongly with PCBM at 647 nm, and may help explain the higher photocurrent production when illuminating the device on resonance with the

low-energy absorption band of the polymer. This may indicate more efficient charge generation and separation in these blends coupled with more efficient absorption at this wavelength. With the addition of ODT, we see that these correlations are less clear for both the acceptor and donor modes, which may support the view that both moieties are interacting equally with PCBM at the D/A interface due to improved phase segregation in these films. Although the interaction between the polymer and fullerene appears to be weaker in ODT treated blends, increased photocurrents are due to improved charge transport.

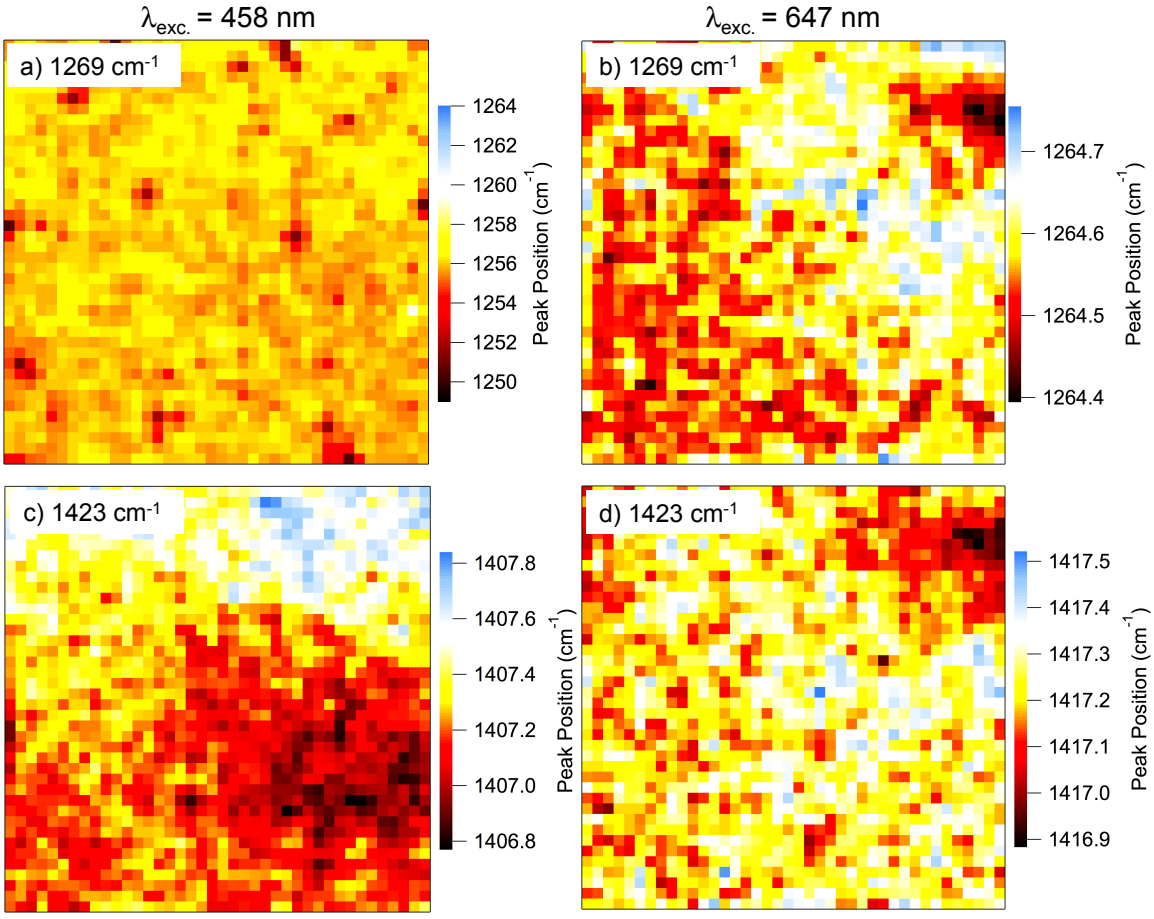

Figure 3.2.1. Raman frequency images of acceptor (a, b) and donor (c, d) moiety Raman modes in PCPDTBT:PCBM (10:20 mg/ml) photovoltaic devices at 458 and 647 nm

excitation. All images are of the same 10 × 10 μm area as in Figure 3.1.1. Pixel values represent fitted (Gaussian) peak positions of the indicated modes.

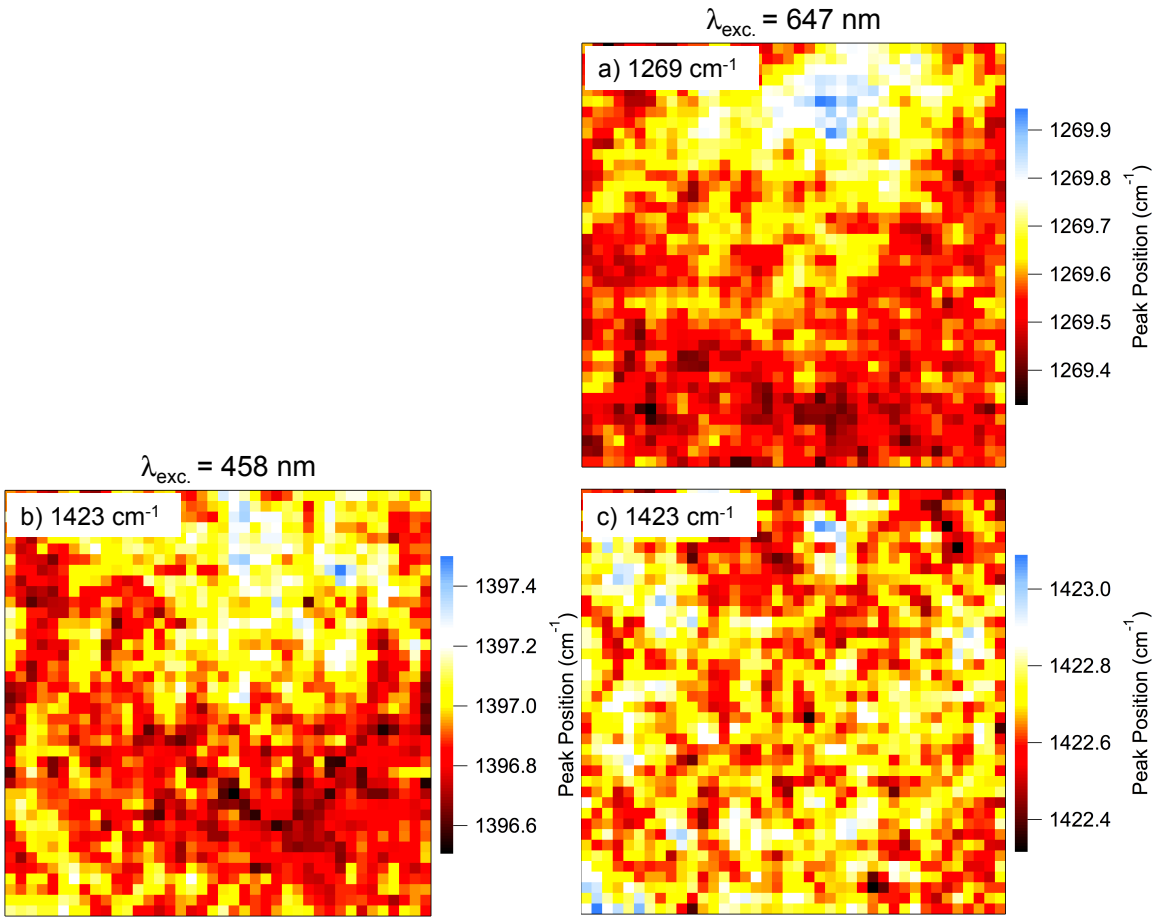

Figure 3.2.2. Raman frequency images of acceptor (a) and donor (b, c) moiety Raman modes in PCPDTBT:PCBM:ODT (10:20:30 mg/ml) photovoltaic devices at 458 and 647 nm excitation. All images are of the same 10 × 10 μm area as in Figure 3.1.2. Pixel values represent fitted (Gaussian) peak positions of the indicated modes. The 1269 cm^{-1} acceptor mode is not shown due to weak signal strength at 458 nm.

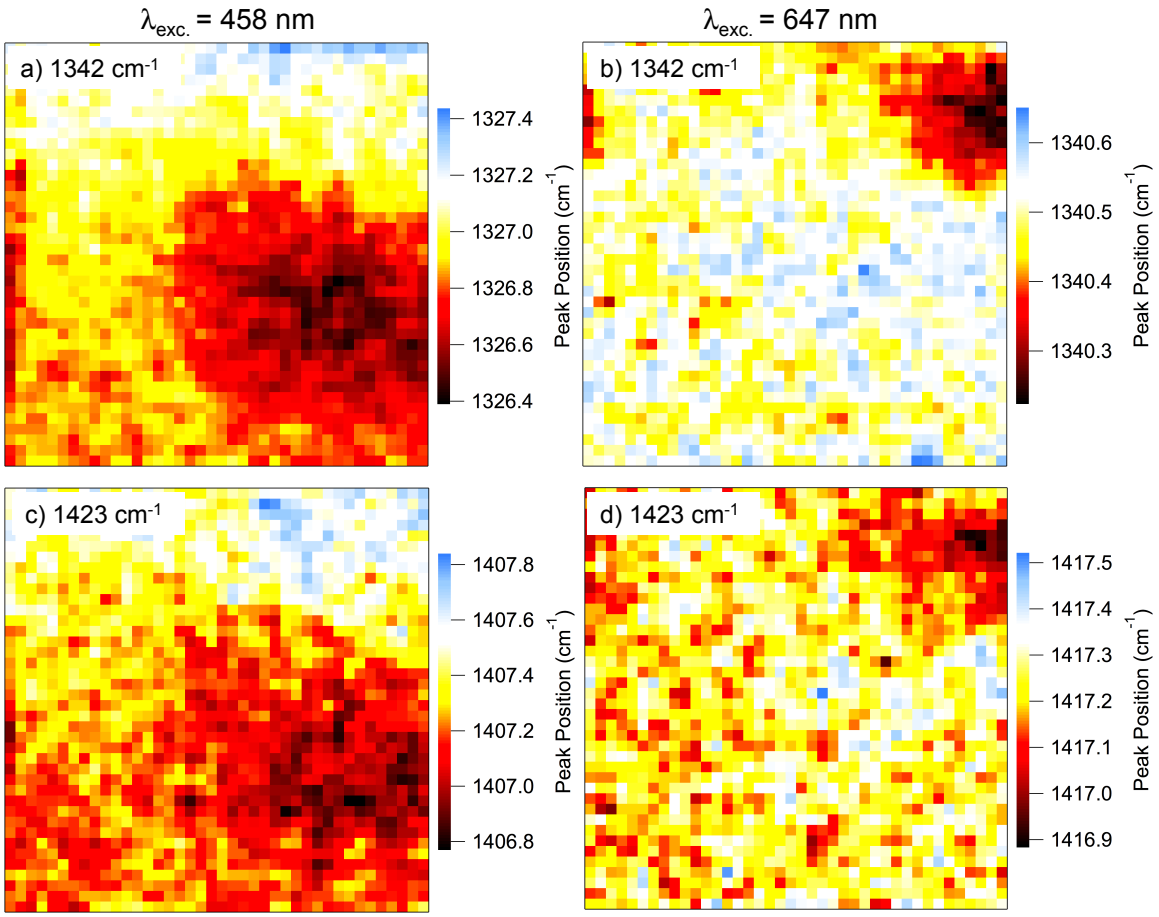

Figure 3.2.3. Raman frequency images of acceptor (a, b) and donor (c, d) moiety Raman modes in PCPDTBT:PCBM (10:20 mg/ml) photovoltaic devices at 458 and 647 nm excitation. All images are of the same 10 × 10 μm area as in Figure 3.1.1. Pixel values represent fitted (Gaussian) peak positions of the indicated modes.

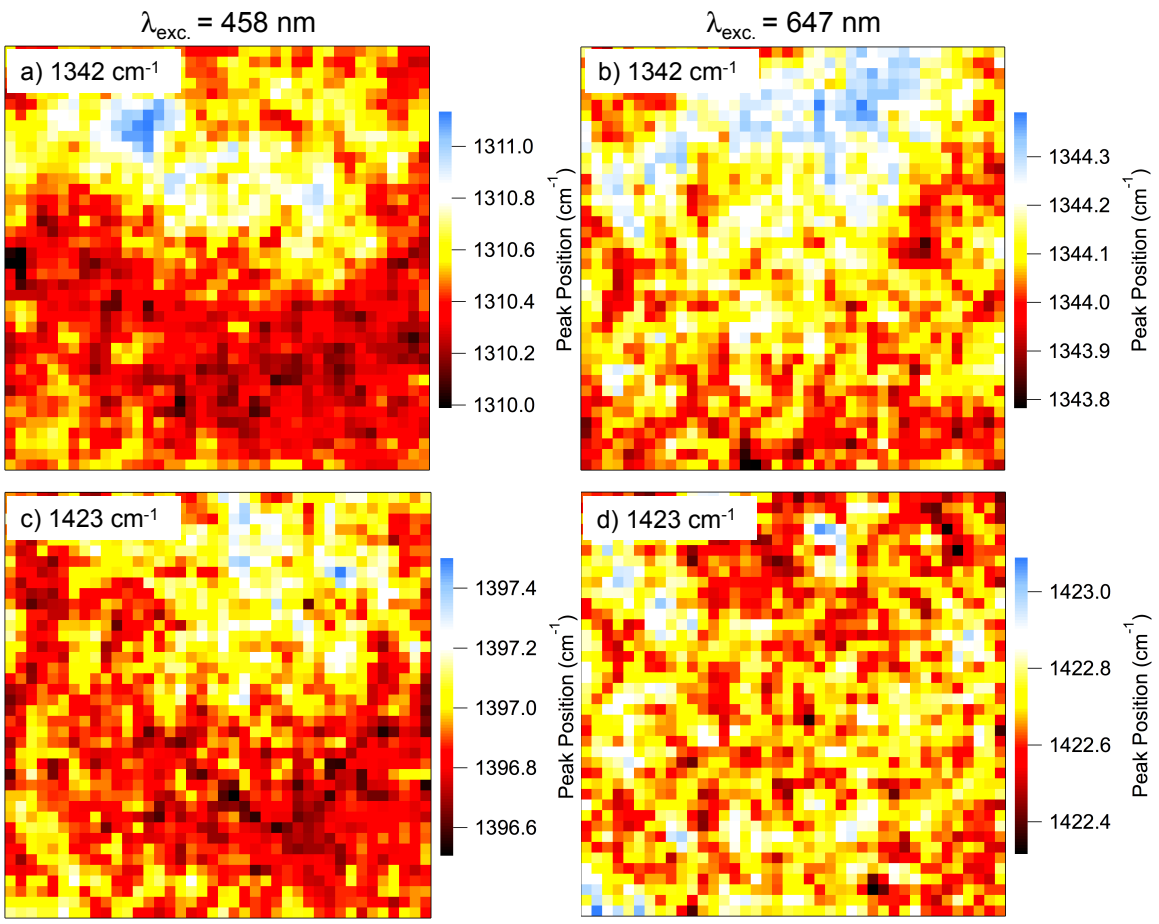

Figure 3.2.4 Raman frequency images of acceptor (a, b) and donor (c, d) moiety Raman modes in PCPDTBT:PCBM:ODT (10:20:30 mg/ml) photovoltaic devices at 458 and 647 nm excitation. All images are of the same 10 × 10 μm area as in main article Figure 3.1.2. Pixel values represent fitted (Gaussian) peak positions of the indicated modes.

3.3 Photocurrent Imaging

Solar cell devices were made with PCPDTBTPCBM:ODT blends of 10:20:20 mg/ml and 10:20:30 mg/ml. Current-Voltage plots for these devices are shown in Figure 3.3.1. The dark curves show characteristic diode rectification behavior, although with reduced sharpness at the turn-on voltage, and noticeable reverse-bias leakage current beyond -0.5V. The leakage current can be attributed to a low shunt resistance in the device.[101] The slower increase in forward current compared to an ideal diode is likely a

result of carrier recombination and Mott-Gurney behavior within the active layers of these devices.[102] In a transient photoconductivity study of PCDTBT:PCBM solar cell devices, Street et al. determined that it is not geminate recombination, but non-geminate recombination that accounts for the majority (~85 – 90%) of photogenerated carrier loss.[103] It is reasonable to assume that the same recombination mechanisms are at work in the PCPDTBT solar cells investigated here. The illuminated curves produced by both devices in Fig. 3.3.1 have a distinct S-shape, which has been explained by Finck and Schwartz to be a result of a combination of a mismatch in carrier mobility, i.e. $\mu_e \neq \mu_h$, and a decrease in electron mobility near the cathode.[104]

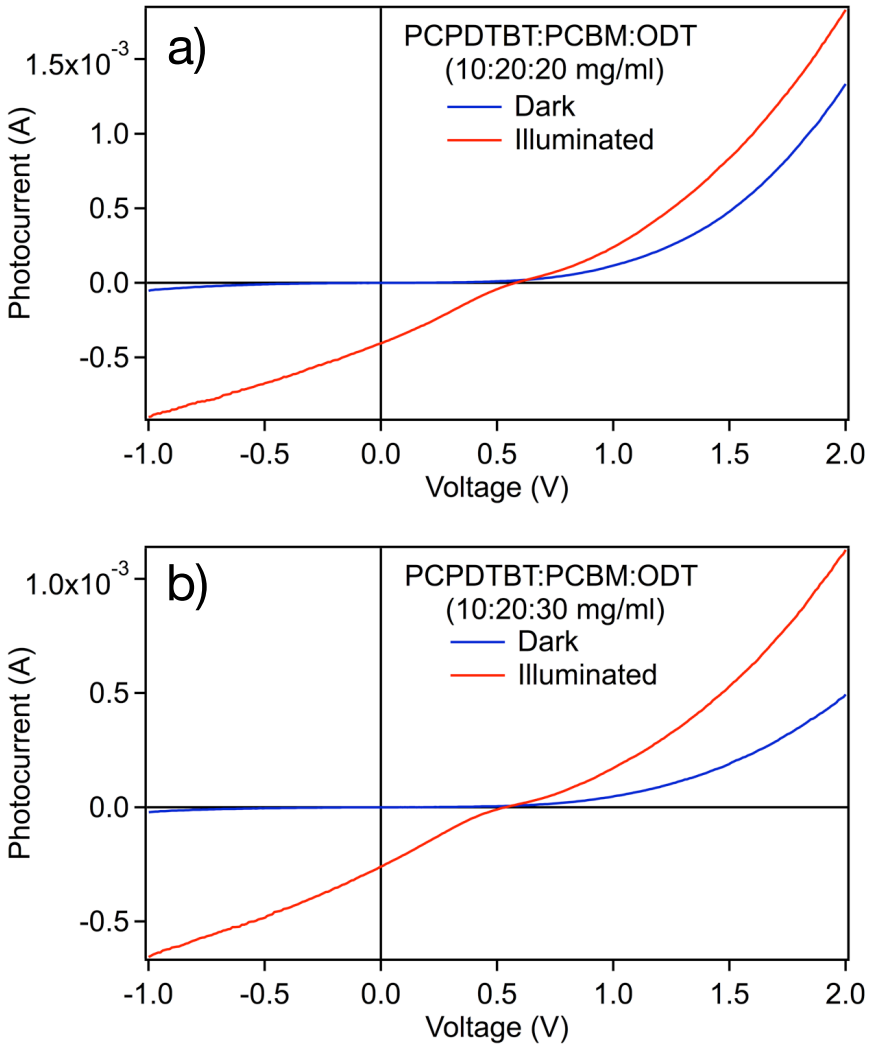

Figure 3.3.1 Current-voltage plots for PCPDTBT:PCBM:ODT devices at a) 10:20:20 and b) 10:20:30 mg/ml blend ratios.

We now explore the effect of excitation energy on local photocurrent production in these solar cells using photocurrent imaging. Figure 3.3.2 shows photocurrent images of a PCPDTBT:PCBM:ODT solar cell device under 405 and 647 nm excitation for the same area used to generate Raman images but over a smaller scan range. The shorter wavelength excitation was produced from a laser diode and was chosen to elicit PCBM, which has a larger absorption cross-section in this region. Raman imaging was not

possible using this excitation source due to the line width of the 405 nm diode laser used in this experiment. The magnitude of the photocurrent produced by the device at 647 nm is also ~3 times larger overall than under 405 nm illumination. Since charge transfer between the polymer and the fullerene is a vibration-assisted process, it is possible that inducing molecular vibrations on the BT group by irradiating the device with lower-energy photons enhances charge transfer to the fullerene, resulting in higher photocurrent. Again, we observe small scale phase segregation as a result of the incorporation of ODT, and areas of lower photocurrent production probably correspond to areas of higher PCBM concentration compared to the well-blended regions. The larger photocurrent contributions from well-blended regions are also observed at both excitation wavelengths.

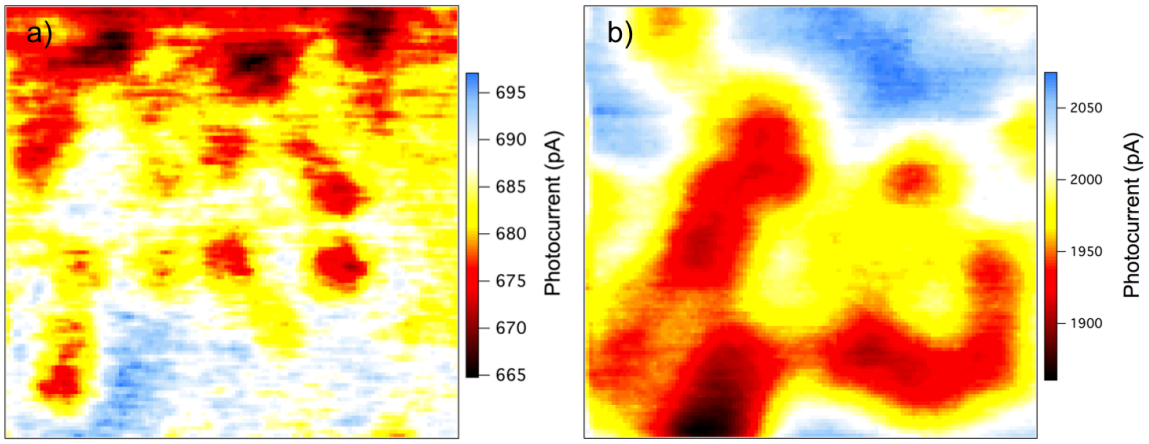

Figure 3.3.2. Photocurrent images of a PCPDTBT:PCBM:ODT (10:20:30 mg/ml) solar cell device at a) 405 nm and b) 647 nm excitation (5 × 5 μm).

4. Doping Studies

Although several studies have shown that improvements in solar cell performance can be achieved through molecular doping of PCPDTBT/PCBM blends, the question of how the dopant molecules interact with the polymer remains unanswered. This chapter is focused on studying the interactions of the small molecule electron acceptors DDQ and F_4-TCNQ with PCPDTBT in thin films. We use absorption and Raman spectroscopies to elucidate changes in polymer morphology and preferential interactions between the polymer and dopant molecules. Density functional theory calculations provide additional insight into the preferred orientations of the dopants relative to the polymer backbone and give an indication of the degree of charge transfer from the polymer to the dopants.

4.1 Background

Previous studies have focused on examining the morphology of polymer chains in thin films and in solutions through bulk spectroscopic and diffraction techniques.[24,73,90,105] In solutions, polymer morphologies have been examined as small molecule electron acceptors have been added in varying ratios.[105,106] These studies have revealed the extent to which the polymers will become more planar as the dopant molecules interact with the polymer backbones. For example, in studies conducted by Gao et al. on poly(3-hexylthiophene) (P3HT), ground state charge transfer is observed from the polymer to the acceptor, and the polymer extends and becomes more planar as a result of benzoid to quinoid transitions along the backbone.[105] In thin films, polymers can adopt varying conformations and morphologies as a function of dopant addition, post-processing treatments such as annealing, and the incorporation of processing additives. For

example, it has been well-established that polymer/fullerene blends experience phase segregation into polymer- and fullerene-rich domains as a result of annealing post casting or addition of octanedithiol or diiodooctane to the blend before casting.[20,24,79,82,87,107-109] This phase separation is an important part of the balance of factors contributing to improved power conversion efficiency in organic solar cell devices. By analyzing the PCE results of 150 donor/acceptor combinations reported in the literature, Jackson et al. have shown a much stronger correlation between J_{SC} and PCE than between V_{OC} and PCE.[110] Since V_{OC} is related primarily to the energy offset between the donor and acceptor species and the acceptor strength,[48] i.e. first reduction potential, of the acceptor, and J_{SC} is related to carrier concentration and mobility, and therefore morphology of donor and acceptor domains, it stands to reason that active layer morphology exerts the greatest control over device performance. In addition, it has been shown by recent reports that molecular doping of conjugated polymers and polymer/fullerene blends can fill existing trap states and enhance carrier mobility.[111-113]

Other studies have shown that adding a small amount of strong electron-accepting small molecules to the active layer blend can improve solar cell performance.[114,115] The authors of these studies use 2,3,5,6-Tetrafluoro-7,7,8,8-tetracyanoquinodimethane (F_4-TCNQ) as the electron acceptor or dopant molecule, and show performance improvements in the usual solar cell operating parameters including short circuit current, open circuit voltage, and fill factor; and show power conversion efficiency enhancements of as much as 24 %.[116] The authors of these studies attribute these enhancements to increased hole mobility within polymer domains, as well as decreased charge recombination via charge transfer states. These studies have been aimed at improving the

OPV device performance, but have left the question of how the small molecule electron acceptors interact with the polymer unanswered. In this chapter, we investigate the preferential interactions between the electron-accepting dopants 2,3-Dichloro-5,6-dicyano-1,4-benzoquinone (DDQ) and F_4-TCNQ, and PCPDTBT.

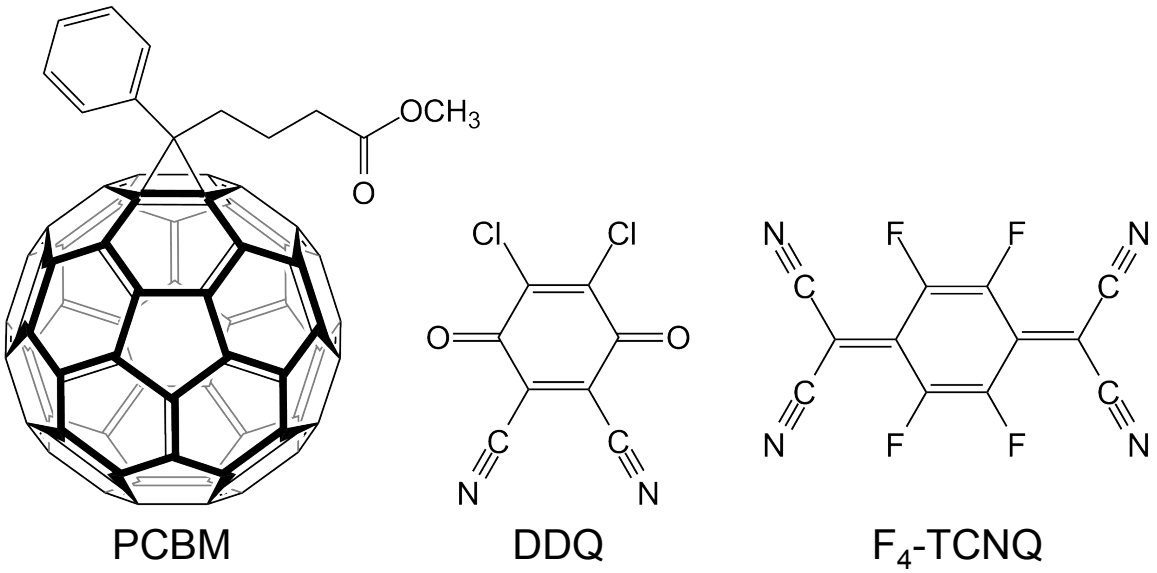

Figure 4.1.1. Structures of $PC_{61}BM$, DDQ, and F4-TCNQ.

Figure 4.1.1 shows the structures of PCBM, DDQ, and F_4-TCNQ. It is important to note that while PCBM is important as an electron acceptor in functioning OPV devices, it generally only acts as an acceptor for electrons in the excited state of a donor molecule. DDQ and F_4-TCNQ, however, have LUMO levels that lie below that of PCPDTBT, permitting ground state charge transfer from the polymer. Figure 4.1.2. shows the relationship between the reported HOMO and LUMO levels of PCPDTBT, $PC_{61}BM$, DDQ, and F_4-TCNQ.[117-120]

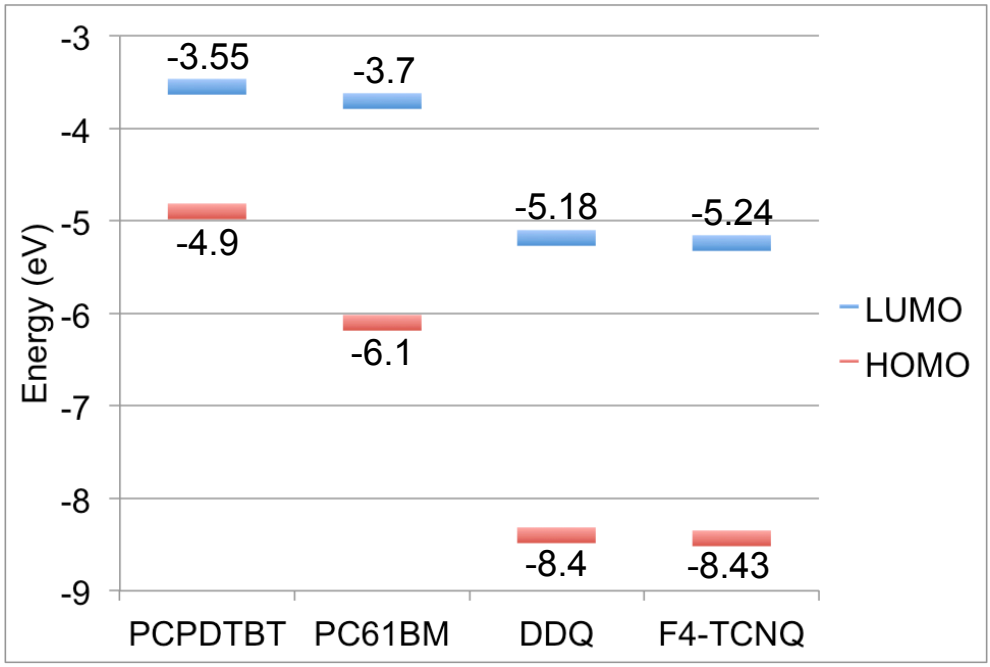

Figure 4.1.2. HOMO and LUMO energy levels relative to vacuum for PCPDTBT, PC61BM, DDQ and F_4-TCNQ.

4.2. Spectroscopy of Doped PCPDTBT Thin Films

Figure 4.2.1 shows absorption spectra of PCPDTBT thin films blended with DDQ at weight ratios from zero to 10%. The most immediately noticeable feature in the absorption lineshape is the appearance of a broad band centered at ~1200 nm, which has been assigned to PCPDTBT polaron absorption.[78,96,121-125] We see this band appear at a 2 wt % blend ratio and increase in intensity as the doping level is increased to 10 %. Another notable change is a red shift followed by a blue shift in the PCPDTBT absorption peak centered at 700 nm. Looking at the absorption peak centered at 700 nm, adding as little as 0.1 wt % DDQ to pristine PCPDTBT causes an immediate red-shift of ~30 nm in peak position, indicating increased ordering of the polymer backbone and more extended conjugation. The effects of increasing the doping levels from 0.1 to 1 wt % are subtle, suggesting that the majority of sites on the polymer backbone available to

interact with DDQ are already occupied at a 0.1 wt % loading. Further increasing the DDQ loading from 1 to 10 wt %, we see this peak shift back toward the blue, which is likely due to DDQ anion absorption,[126-130] along with increased charge localization on the polymer backbone and decreased absorbing chromophore lengths. The peak centered at 405 nm experiences a reduction in intensity when 0.1 Wt % DDQ is blended with the polymer, and further decreases in intensity as more DDQ is added up to 1 wt %. The reduction in absorption by the blend in that portion of the spectrum is likely due again to the increased ordering of the polymer chains, although the effects of adding small amounts of DDQ on the spectrum are more gradual for the high energy PCPDTBT absorption peak compared to the immediate and nearly static red-shift of the 700 nm peak between loadings of 0 and 1 wt % DDQ. At loading levels above 1 wt %, The intensity of the 405 nm peak increases, likely to due to increasing absorption by DDQ itself, between 1 and 10 wt %.

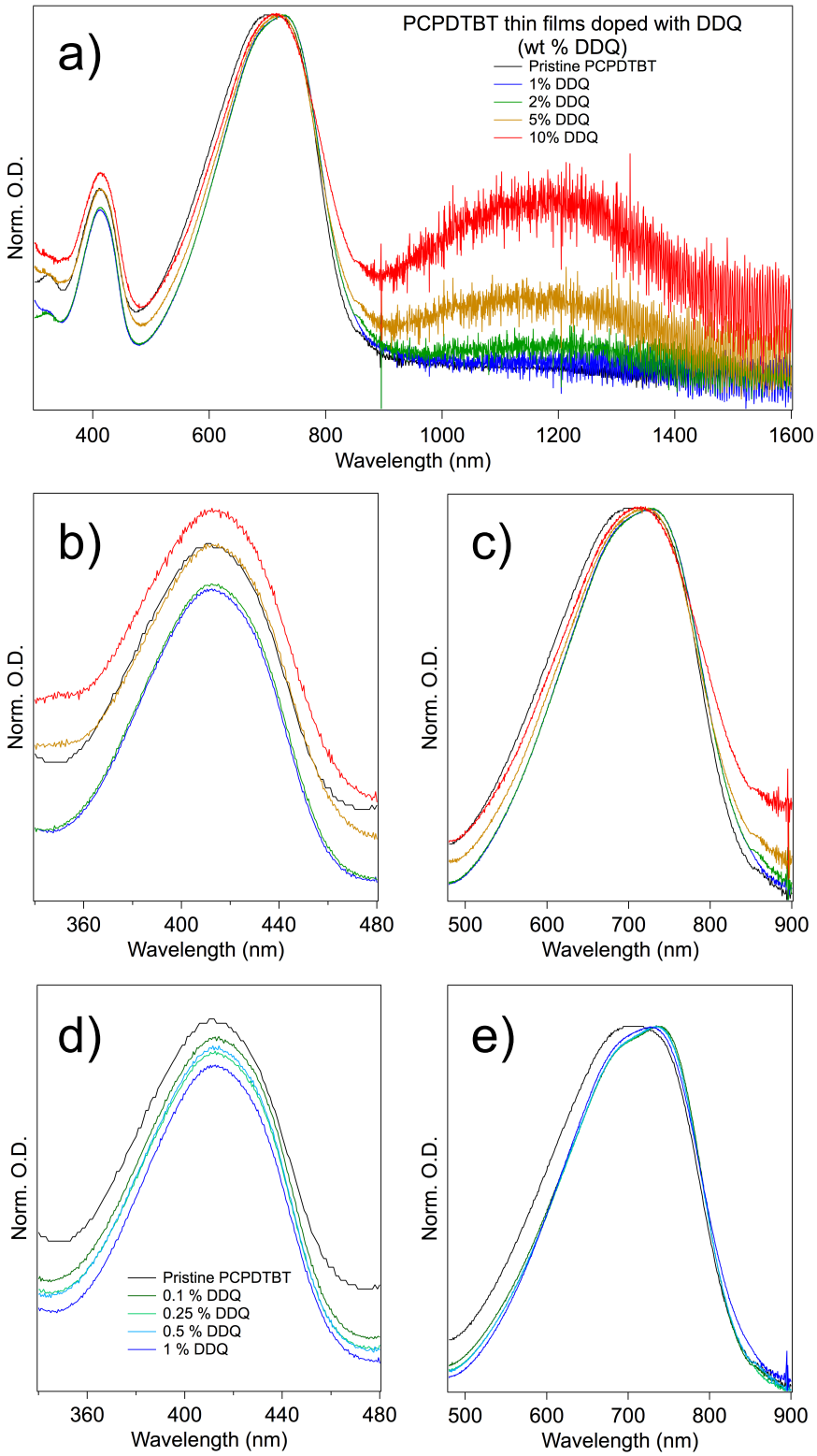

Figure 4.2.1. Absorption spectra of PCPDTBT thin films doped with DDQ at weight ratios from 0 to 10%. The legend for a) applies to b) and c). The legend for d) applies to e).

Figure 4.2.2 shows absorption spectra collected for thin films of PCPDTBT doped with F_4-TCNQ at blend weight percentages from 0 to 10 %. As with DDQ, we see the broad PCPDTBT polaron band centered around 1200 nm, although this band is weakly present at a 5 wt % doping level and doesn't grow to appreciable strength until a loading of 10 wt % F_4-TCNQ is reached. We also see similarities in the behavior of the 700 nm absorption peak when doping with F_4-TCNQ compared with doping with DDQ. At the smallest doping level of 0.1 wt % F_4-TCNQ, we see that the 700 nm peak has red-shifted by ~14 nm (Fig. 4.2.2 e). The smaller shift in peak position with F_4-TCNQ compared to DDQ may be due to the stronger electron-accepting nature of F_4-TCNQ and the resulting increased charge localization and effective chromophore shortening. Increasing the percentage of F_4-TCNQ from 0.1 to 1 wt % has little additional effect on this peak. Once again, we can infer from this that the majority of available interaction sites on the polymer backbone are occupied, by F_4-TCNQ in this case, at a dopant loading of 0.1 wt %. Increasing the F_4-TCNQ loading from 1 wt % to 10 wt % does little to alter the position of this peak, but does cause slight broadening of the peak in the NIR between 800 and 850 nm, and we see the emergence of the F_4-TCNQ anion peak at 860 nm.[131-133] In contrast to the absorption behavior with DDQ, the decrease in intensity in the 405 nm peak is more drastic at a F_4-TCNQ loading of 0.1 wt % and then only decreases slightly from 0.1 wt % up to a loading of 1 wt % (Fig. 4.2.2 d). The decrease in intensity of this peak can again be attributed to increased ordering in PCPDTBT, although the stronger electron-accepting character of F_4-TCNQ appears impose this effect more strongly than DDQ. Increasing the doping level from 1 wt % to 10 wt % produces an increase in

intensity in the 405 nm peak, and this can be attributed to increased absorption by F_4-TCNQ itself.

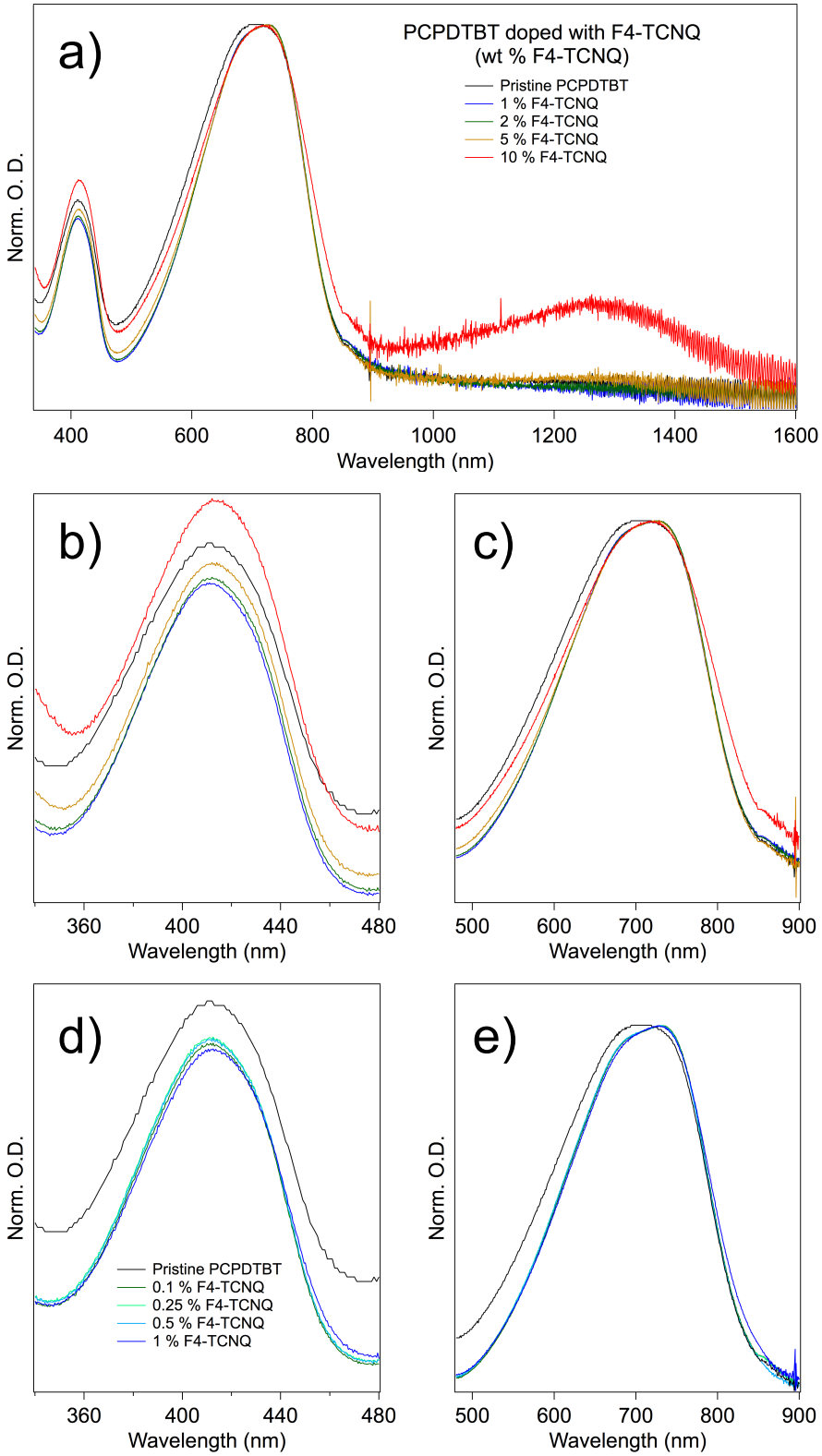

Figure 4.2.2. Absorption spectra for PCPDTBT films doped with F_4-TCNQ at weight ratios from 0 to 10%. The legend for a) applies to b) and c). The legend for d) applies to e).

The question of preferential interaction with PCPDTBT moieties remains. Raman spectroscopy allows us to explore the interactions between DDQ and F_4-TCNQ with specific PCPDTBT moieties by examining the behavior of the major PCPDTBT vibrational modes discussed in Chapter 2. An excitation wavelength of 780 nm is chosen for these investigations as it is pre-resonant to the polymer absorption profile. Here, as with the previous Raman studies, the strong PCPDTBT fluorescence precluded collecting a spectrum of the pristine polymer. Figure 4.2.3 show Raman spectra for PCPDTBT thin films doped with DDQ (a) and F_4-TCNQ (b). All spectra are normalized to the BT 1342 cm^{-1} mode.

At low DDQ doping levels, the signal to noise ratio is low due to strong PCPDTBT fluorescence, but increases as more DDQ is added to the blend, quenching the remaining fluorescence. Doping PCPDTBT with increasing loadings of DDQ most notably gives rise to an increase in intensity of the 1269 cm-1 BT symmetric in-plane C—H wag. We also see an increase in the intensity for the 1534 cm^{-1} BT C—C stretch and C—H wag. The CPDT vibrational modes are less affected by the addition of DDQ, suggesting that DDQ primarily interacts with the acceptor BT moiety, causing increased charge localization on that moiety. This idea is supported by DFT calculations that show increased wavefunction overlap and degree of charge transfer between PCPDTBT and DDQ when DDQ is placed over the BT group (see Section 4.3). Comparing differences in intensities of other modes at 1 and 2 wt % and 5 and 10 wt % DDQ is difficult because of the noise in the Raman signal at lower doping levels. However, upon increasing the dopant loading from 5 to 10 wt %, we see an increase in the 1195 mixed CPDT-BT mode

and 1423 cm-1 CPDT dithiophene C—C stretching mode, suggesting that the interaction between DDQ and PCPDTBT is not limited entirely to the BT moiety.

Similar trends in PCPDTBT vibrational modes are visible in films doped with F_4-TCNQ. Strong PCPDTBT fluorescence prevented collection of Raman spectra at F4-TCNQ doping levels below 5 wt %, which may be due to the rapid occupation of available interaction sites on the PCPDTBT backbone as discussed in Section 4.2, preventing interaction with additional F4-TCNQ molecules that would otherwise quench polymer fluorescence. The Raman signals at 5 and 10 wt % are still noisy as a result, but differences in mode intensities are discernable. As with DDQ, the most noticeable change when increasing the F4-TCNQ loading level from 5 to 10 wt % is in the increase in the BT 1269 cm-1 in-pane C—H wag intensity. At the same time, we see a decrease in the relative intensity of the 1534 cm-1 mode, which is likely due to a decrease in the C—C stretching component of that mode. This again suggests preferential interaction between F4-TCNQ and the BT moiety along with increased localization and charge transfer character. This is in contrast to the idea proposed by Di Nuzzo et al. that the primary interaction between F4-TCNQ and PCPDTBT is with the donor CPDT group.[134] Given the quantity of noise in the Raman signals, it is difficult to make comparisons in the intensities of the other vibrational modes.

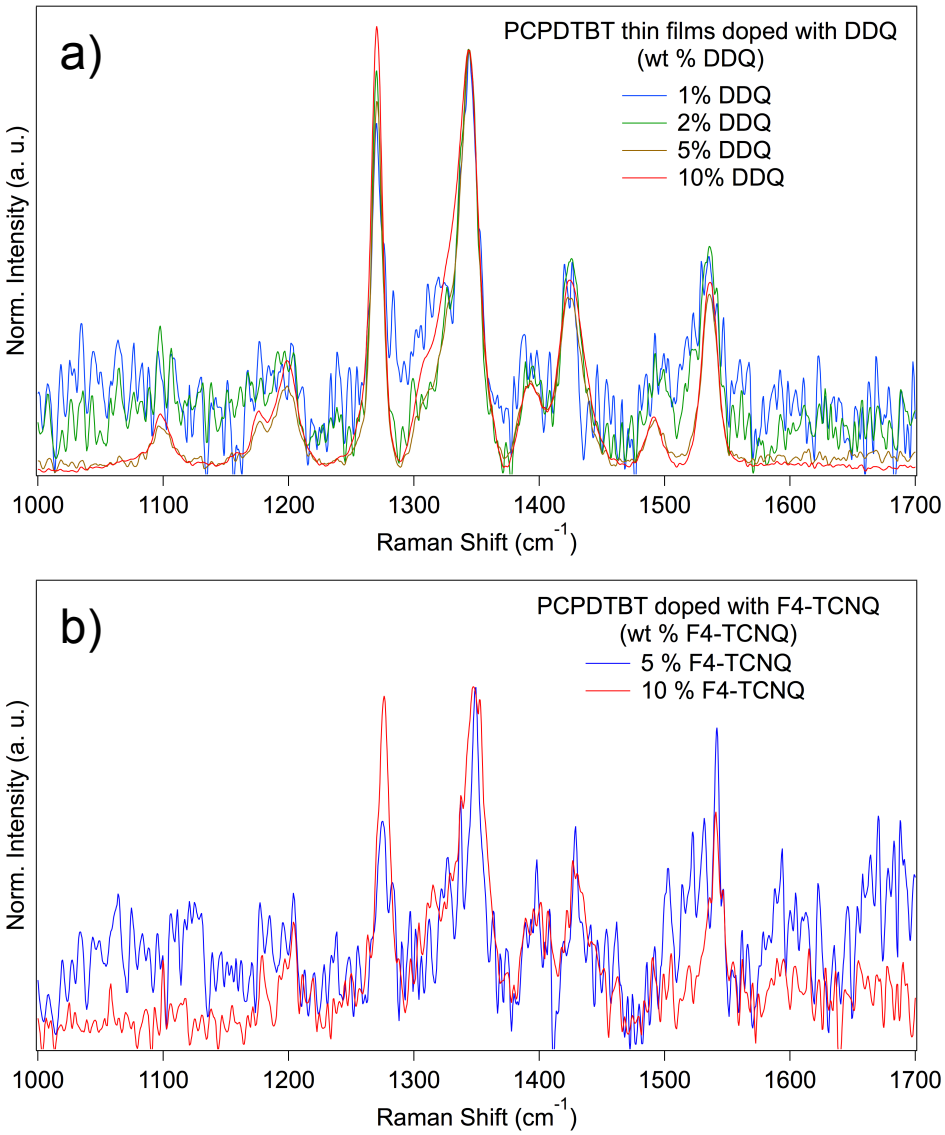

Figure 4.2.3. Raman spectra of PCPDTBT thin films doped with a) DDQ and b) F_4-TCNQ collected using 780 nm excitation. The PCPDTBT photoluminescence prevented collection of Raman spectra of pure PCPDTBT and at F_4-TCNQ doping concentrations lower than 5%.

4.3. DFT Calculations of PCPDTBT Interactions with DDQ and F_4-TCNQ

In order to better understand the interactions between DDQ, F_4-TCNQ, and PCPDTBT, DFT simulations were carried out on a PCPDTBT dimer with DDQ and F_4-TCNQ. We used the B3LYP functional with 6-311g(d) basis set for all calculations as in

Chapter 2. All calculations for the interactions between PCPDTBT and DDQ, and between PCPDTBT and F_4-TCNQ started with geometries in which the plane of the DDQ or F_4-TCNQ molecules were parallel to the plane of the dimer backbone. To examine the effect of dopant molecule position relative to the dimer, we investigated three starting geometries. In the first, the dopant is positioned squarely over the BT group, in the second, the dopant is positioned between the BT and CPDT groups, and in the third, the dopant is positioned over the CDPT group.

The starting and optimized geometries for these arrangements between PCPDTBT and DDQ are illustrated in Figure 4.3.1. We see that when the DDQ molecule is centered over the BT group, optimization keeps the DDQ essentially in the same location, although tilted with respect to the PCPDTBT dimer. When the DDQ is placed between the BT and CPDT groups, as in Fig. 4.3.1 b), we see that optimization tilts the DDQ away from the abbreviated side chains. This effect is increased when the DDQ is placed above the CPDT group (Fig. 4.3.1 c)). This effect is likely due to the steric hindrance caused by the side chains. This effect is expected to be more extreme in a real blend of PCPDTBT and DDQ, where the full, branched polymer alkyl side chains would strongly limit the possibility for DDQ to position itself parallel to the polymer backbone in proximity to the CDPT groups. We also see that in case c), the optimized position of the DDQ is rotated such that the CN groups are pointing away from the side chains, which again may be a result of steric hindrance. The calculated electronic interactions between PCPDTBT and DDQ are illustrated by the HOMO isosurface representations in Figure 4.3.2. The orbital illustrations in Figure 4.3.2 a), b), and c) correspond to the optimized geometries in Fig. 4.3.1 a), b), and c), respectively. As we would expect as a result of DDQ being tilted

farther away from a parallel arrangement with the dimer backbone, we see a decrease in orbital overlap between PCPDTBT and DDQ. The reduced interaction is also apparent in the sum of Mulliken charges, which show a monotonic decrease in electron transfer between the dimer and DDQ. When DDQ is positioned over the BT group, we see 0.46 e- transferred between the dimer and DDQ, 0.35 e- when DDQ is between the BT and CPDT groups, and 0.23 e- when DDQ is above the CDPT groups. These simulations suggest that steric hindrance plays a major role in limiting the interaction of DDQ with CPDT groups, which correlates well our observations of increased BT Raman activity upon doping with DDQ.

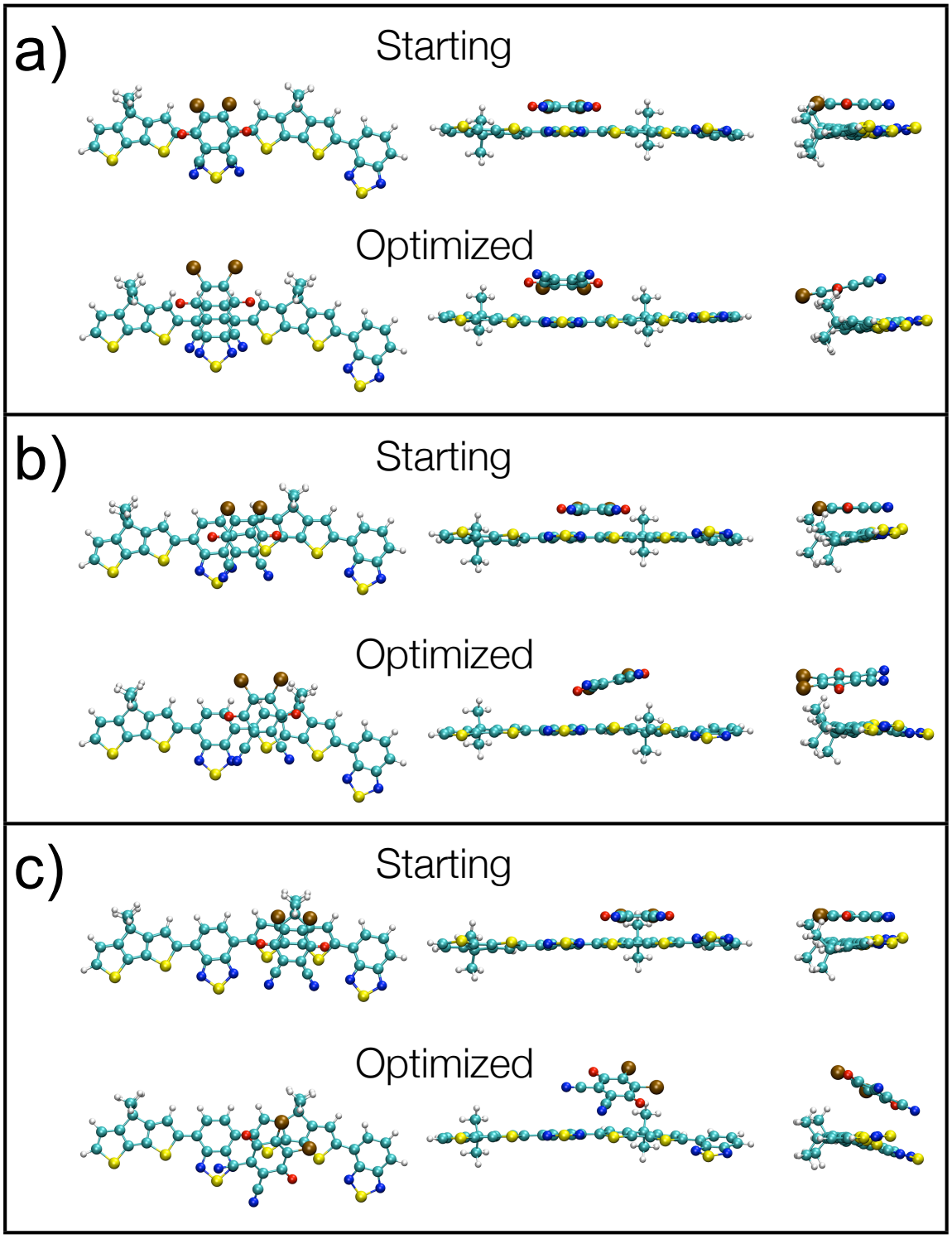

Figure 4.3.1. Starting and optimized geometries for interactions between a PCPDTBT dimer and DDQ, beginning with the long axis of DD parallel to the dimer backbone. Starting geometries are a) DDQ over the BT group, b) DDQ centered between the CPDT and BT groups, and c) DDQ centered over the CPDT group.

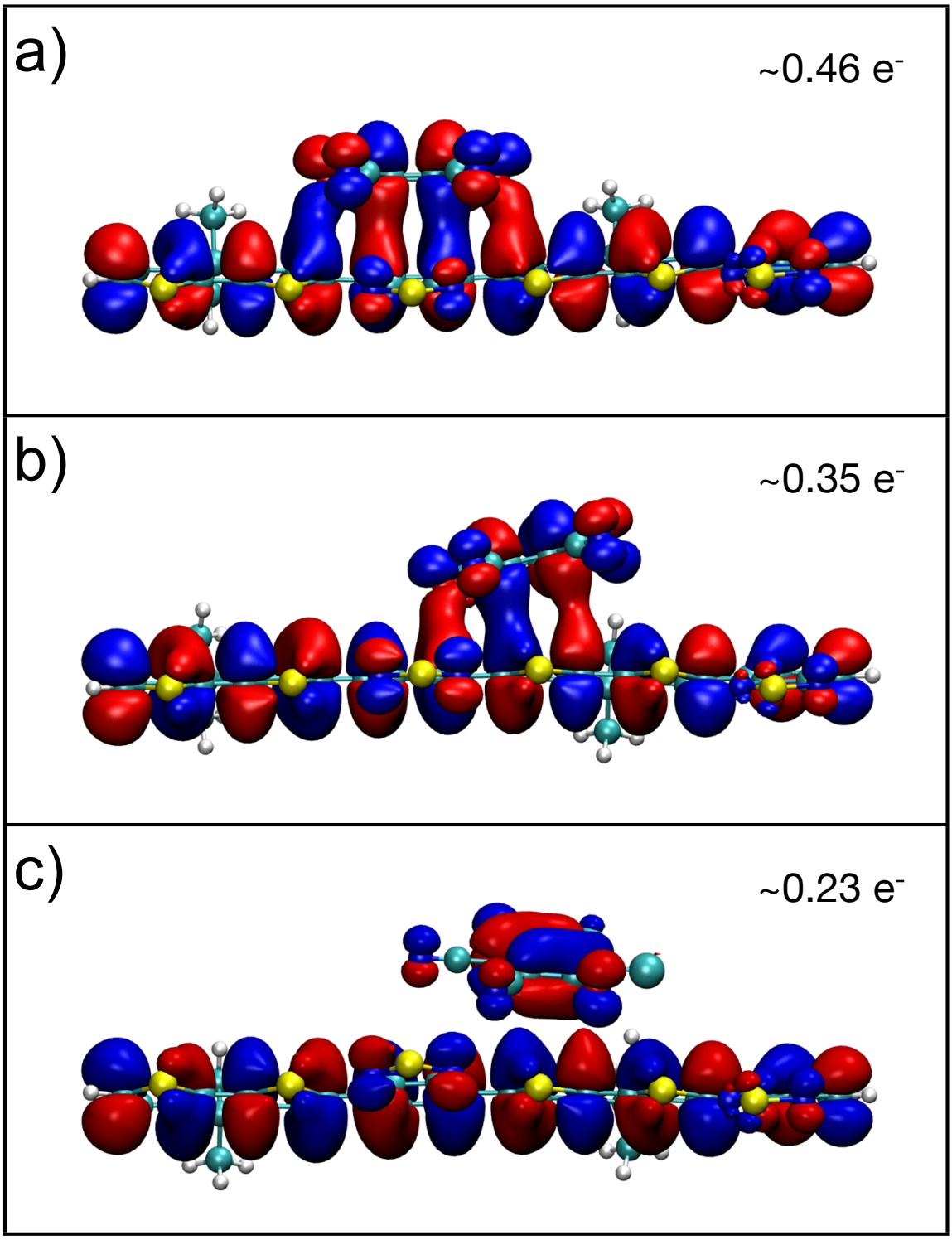

Figure 4.3.2. HOMO isosurfaces calculated for optimized geometries in Fig. 4.3.1 a), b), and c). Representations are at an isovalue of 0.01. Values in each pane indicate portion of electron transfer between the PCPDTBT dimer and DDQ.

We see some similar effects between PCPDTBT and F_4-TCNQ. When F_4-TCNQ is centered over the BT group, the optimization keeps the F_4-TCNQ molecule in essentially the same location, albeit rotated and tilted slightly. The tilting we see in this case is similar to that for the case with DDQ. The rotation of F_4-TCNQ is likely the result of minimizing interference with the abbreviated side chains. The position of the F_4-TCNQ quinoid group relative to the dimer is almost unchanged, but the optimized geometry shows that the molecule has been rotated such that the CN groups on the right hand side of the molecule are equidistant from the side chain on the CPDT group. With F_4-TCNQ starting between the BT and CPDT groups, optimization results in a tilting of the F_4-TCNQ molecule away from the side chains, again with a rotation. The rotation in this case is in the opposite direction from the above case, but we see again how the rotation results in less molecular congestion near the side chains by moving the CN groups away from the side chains. In this case, we also see a bending of the dimer backbone, bringing the right-most BT group closer to the F_4-TCNQ. The bending of the dimer backbone when interacting with F_4-TCNQ may be due to the larger energy offset between the PCPDTBT HOMO and the F_4-TCNQ LUMO and electrostatic attraction, as well as the ability of F_4-TCNQ to span multiple polymer moieties due to its physical size. With F_4-TCNQ starting directly over the CPDT group, the bending of the dimer molecule is even more apparent, suggesting that F_4-TCNQ is interacting with the two BT groups on either side of the CDPT group simultaneously. This effect may also help to explain the relatively uniform degree of ground state change transfer between the PCPDTBT dimer and F_4-TCNQ (vide infra).

Figure 4.3.4 shows molecular orbital isosurfaces calculated for the three optimized structures illustrated in Figure 4.3.3. As in the previous case, Fig. 4.3.4 a), b), and c) correspond to the optimized structures in Fig. 4.3.3 a), b), and c), respectively. In contrast to the decrease in ground state charge transfer between PCPDTBT and DDQ as DDQ is moved from a position over the BT group to a position over the CPDT group, F_4-TCNQ appears to interact strongly enough with PCPDTBT to cause approximately the same degree of charge transfer regardless of its position relative to the two copolymer moieties. The larger energetic offset between the PCPDTBT HOMO and the F_4-TCNQ LUMO may play a part in this as mentioned above, but the size and symmetry of the F_4-TCNQ molecule appear to increase the lateral extent of its interaction with the polymer backbone. This may help to explain the spectroscopic behavior of PCPDTBT blends with F_4-TCNQ at even the lowest blend ratios.

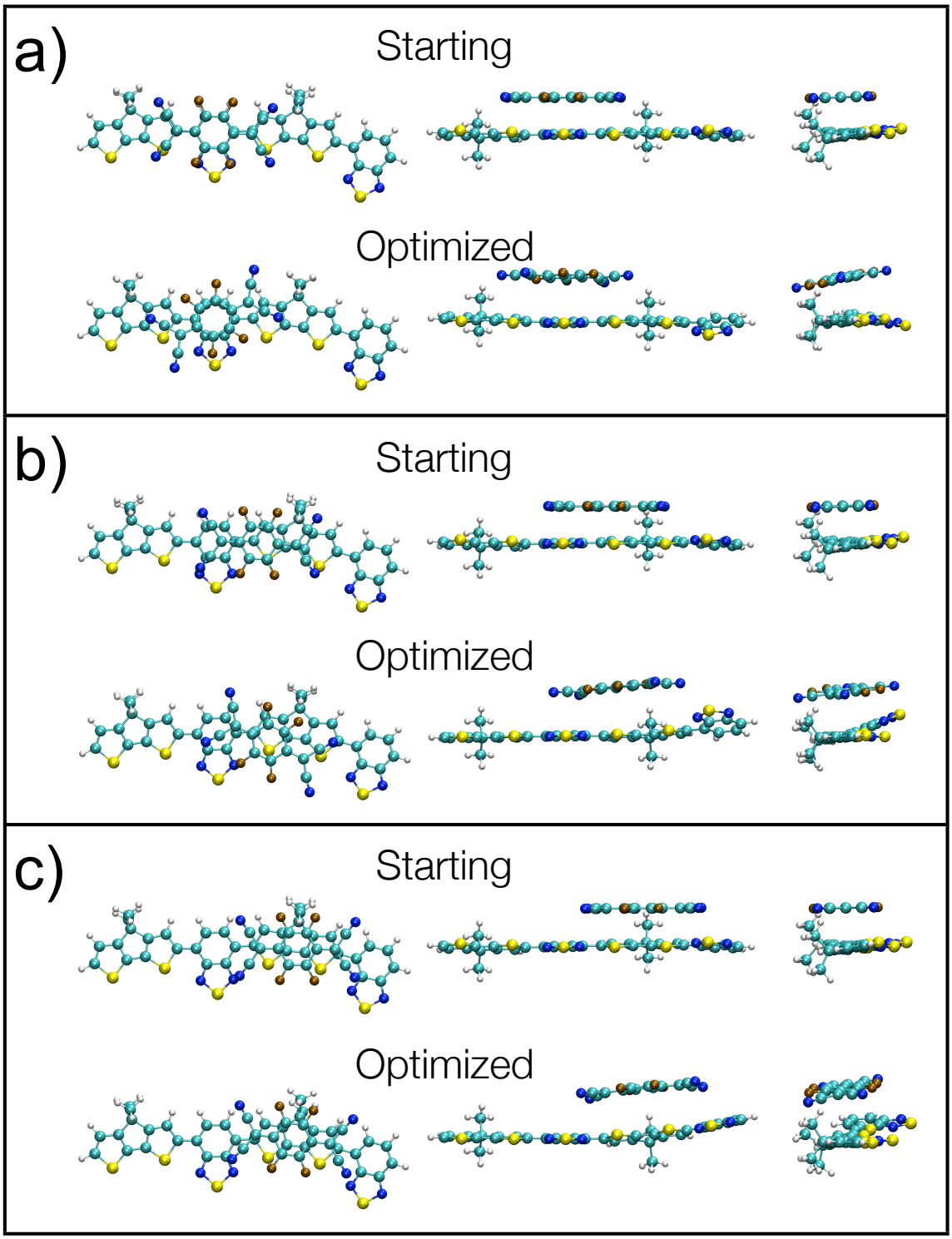

Figure 4.3.3. Starting and optimized geometries for interactions between a PCPDTBT dimer and F_4-TCNQ, beginning with the long axis of F4-TCNQ parallel to the dimer backbone. Starting geometries are a) F_4-TCNQ over the BT group, b) F_4-TCNQ centered between the CPDT and BT groups, and c) F_4-TCNQ centered over the CPDT group.

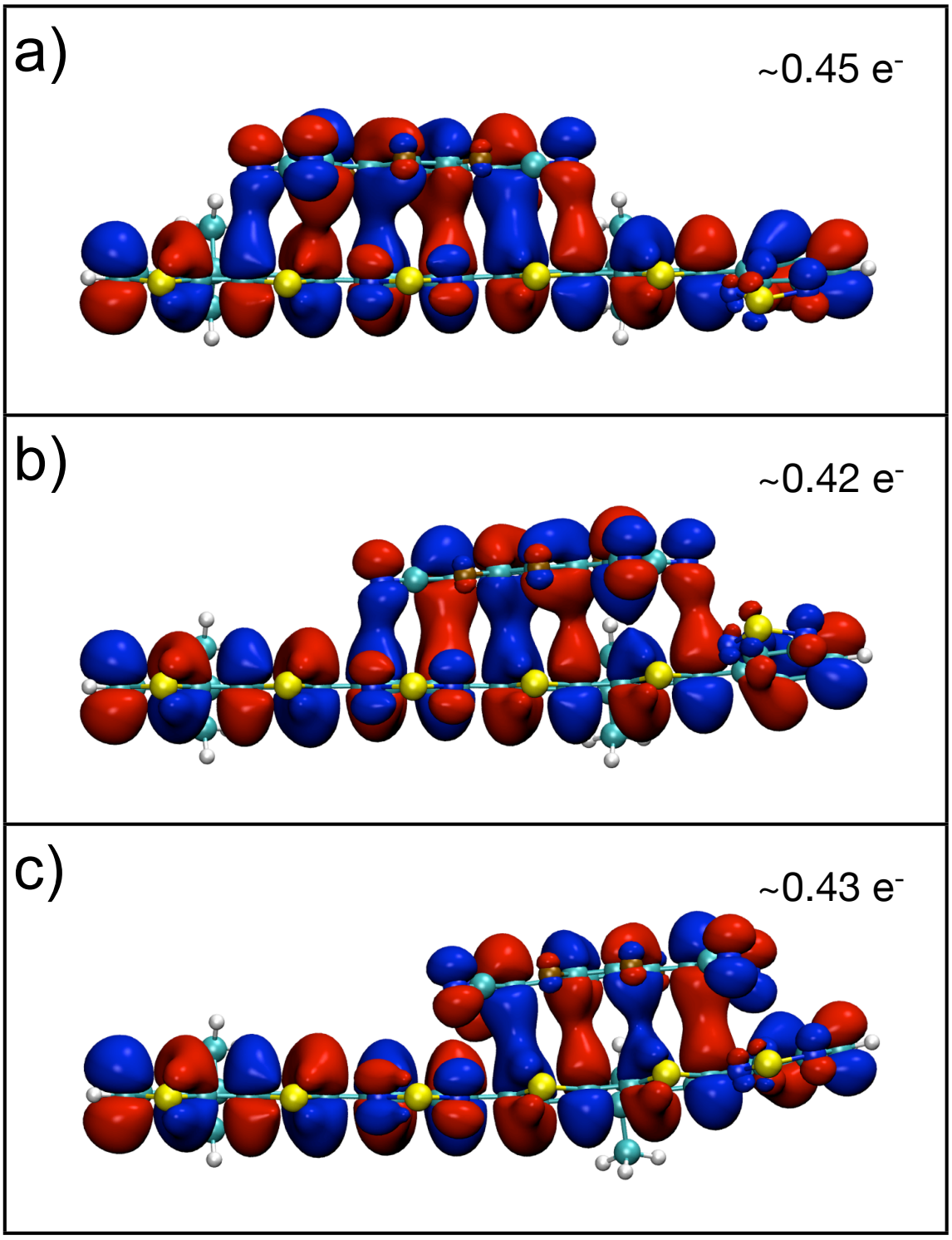

Figure 4.3.4. HOMO isosurfaces calculated for optimized geometries in Fig. 4.3.3 a), b), and c). Representations are at an isovalue of 0.01. Values in each pane indicate portion of electron transfer between the PCPDTBT dimer and F_4-TCNQ.

With the F_4-TCNQ molecule rotated 90° in-plane with respect to the dimer backbone in its starting position, we see that optimization again tends to minimize the interference of the CN groups with the abbreviated side chains. Figure 4.3.5 shows the starting and optimized geometries for the three F_4-TCNQ starting positions. With the F_4-TCNQ in a starting position over the BT group, we see the optimization warp both the dimer and F_4-TCNQ as if wrapping around one-another. Interestingly, this is the only arrangement where the optimization results in a bent F4-TCNQ conformation, and implies a strong interaction between it and the dimer. Another indication of a strong interaction between the dopant and dimer in this position is that the dihedral angle between the BT unit over which the F_4-TCNQ is placed and the two CPDT groups to either side is also increased, bringing the thiadiazole closer to the F_4-TCNQ CN groups. When the F_4-TCNQ is starts between the BT and CDPT groups, the optimized position of the F_4-TCNQ is angled slightly away from the abbreviated side chains, and rotated in-plane such that the CN groups are equidistant from the side chains. This behavior is similar to the case in which DDQ starts in a position over the CPDT group. In this case, the rotation minimizes the steric hindrance between the side chains and F_4-TCNQ, and as in the next case, leads to increased $\pi - \pi$ interaction between the quinoid and the dimer backbone with the HOMO lobes of F_4-TCNQ in a more parallel arrangement with those of the dimer (see Figure 4.3.6). We again see similar behavior when the starting position of the F_4-TCNQ is over the CPDT group. In this case, optimization shifts the F_4-TCNQ slightly away from the CPDT group, tilts the F_4-TCNQ away from the side chains somewhat more than the previous case, and rotates the F_4-TCNQ again to move the CN groups away from the side chains. We also see the right-most BT group of the dimer

tilted to bring the thiadiazole group closer to the F_4-TCNQ. As in the corresponding case where the F_4-TCNQ starts parallel to the dimer backbone over the CPDT group, F_4-TCNQ "attempts" to maximize its interaction with the dimer. In this case, however, the interaction between the BT group and F_4-TCNQ may be primarily an electrostatic attraction between the two nitrogen atoms on the CN groups of F_4-TCNQ (combined charge of -0.44e) and the sulfur of the thiadiazole (0.58e). As with other studies of D/A copolymers, we would expect the torsion of the dihedral angle between the CPDT and BT groups to lead to greater wavefunction localization on the BT group in the excited state,[58,59,84,91,97,98] which supports the observed increased BT Raman activity upon doping with F_4-TCNQ.

Figure 4.3.6 shows calculated HOMO isosurfaces for the optimized geometries in Fig. 4.3.5. As before, the geometries in Fig. 4.3.6 a), b), and c) are those illustrated in Fig. 4.3.5 a), b), and c), respectively. We would expect the degree of interaction, and therefore the degree of charge transfer between PCPDTBT and F_4-TCNQ to increase as the F_4-TCNQ is moved from a position over the CPDT group to over the BT group. However, the sum of Mulliken charges in each case indicates a relatively constant degree of charge transfer between the dimer and dopant, with a maximum of 0.41 e^- transferred to F4-TCNQ when it starts between the two polymer moieties. These results, and the results in the previous set of cases in which F_4-TCNQ is aligned parallel with the polymer backbone, are in contrast to the *ab-initio* results published by Di Nuzzo et al. that indicate near-integer electron transfer to the F_4-TCNQ when the dopant is near the CPDT unit, and near-zero charge transfer when F_4-TCNQ is near the BT unit.[134] Another interesting result of a perpendicular starting arrangement can be seen in the wavefunction overlap

between the two molecules. As shown in Figure 4.3.6 a), the wavefunction overlap between the dimer and F_4-TCNQ is smallest when the F_4-TCNQ starts over the BT group. This may be a result of the calculated molecular orbital lobe arrangement on both molecules. In this case the HOMO lobes of F_4-TCNQ are primarily perpendicular to those of the CPDTBT dimer, and as such should interact very little. Maximum calculated wavefunction overlap occurs in the optimized arrangement when F_4-TCNQ starts between the CPDT and BT groups, as shown in panel c). Rotating the F_4-TCNQ to minimize CN interaction with the dimer side chains allows better alignment of the F_4-TCNQ HOMO lobes with those of the dimer. In the final arrangement, with F_4-TCNQ starting squarely over the CPDT, we see an appreciable amount of wavefunction overlap between the dopant and dimer after optimization, again as a result of rotation of the F_4-TCNQ. In this case the F_4-TCNQ is angled away from the side chains, and this reorientation results in slightly less overlap than in the previous case.

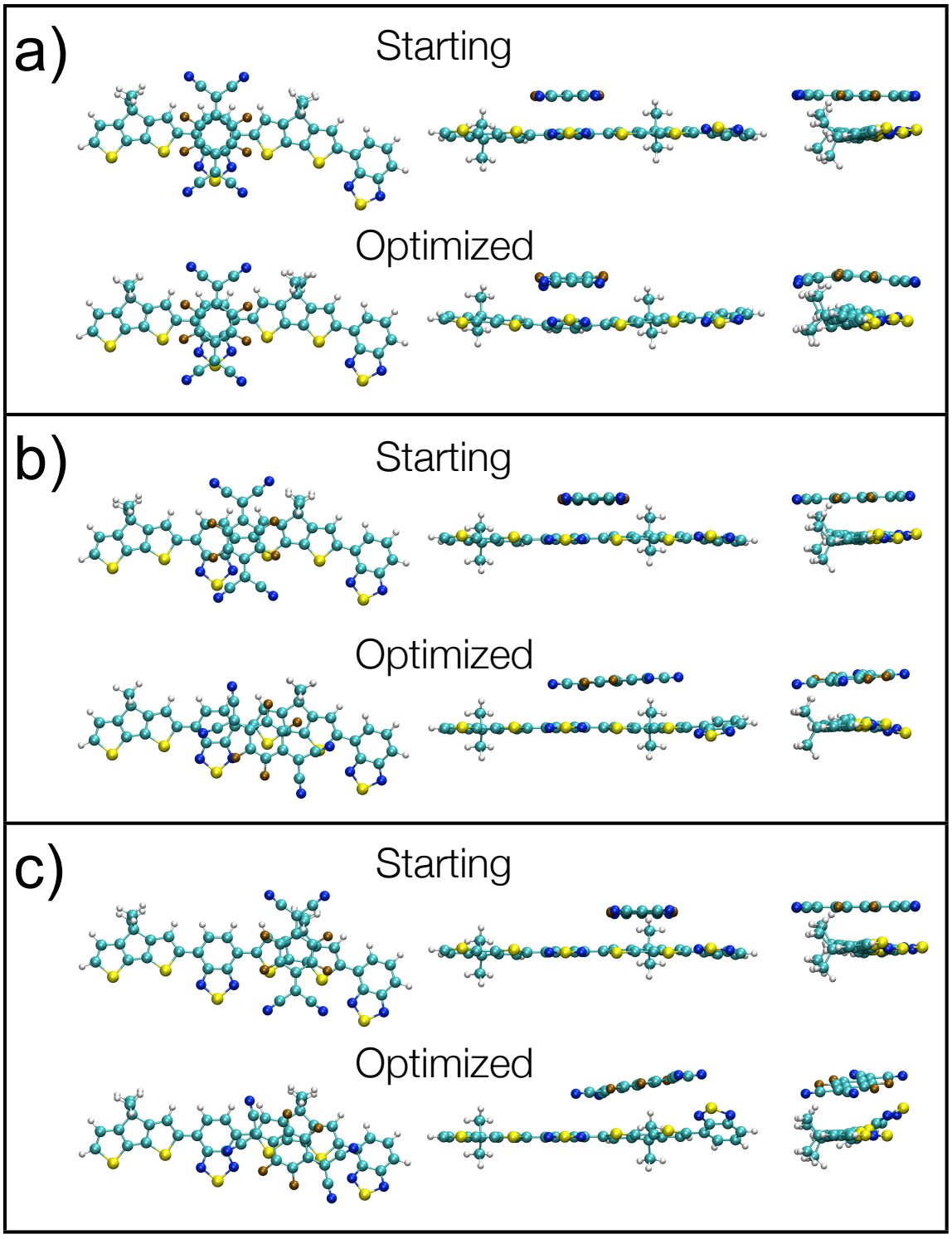

Figure 4.3.5. Starting and optimized geometries for interactions between a PCPDTBT dimer and F_4-TCNQ, beginning with the long axis of F4-TCNQ at 90° to the dimer backbone. Starting geometries are a) F_4-TCNQ over the BT group, b) F_4-TCNQ centered between the CPDT and BT groups, and c) F_4-TCNQ centered over the CPDT group.

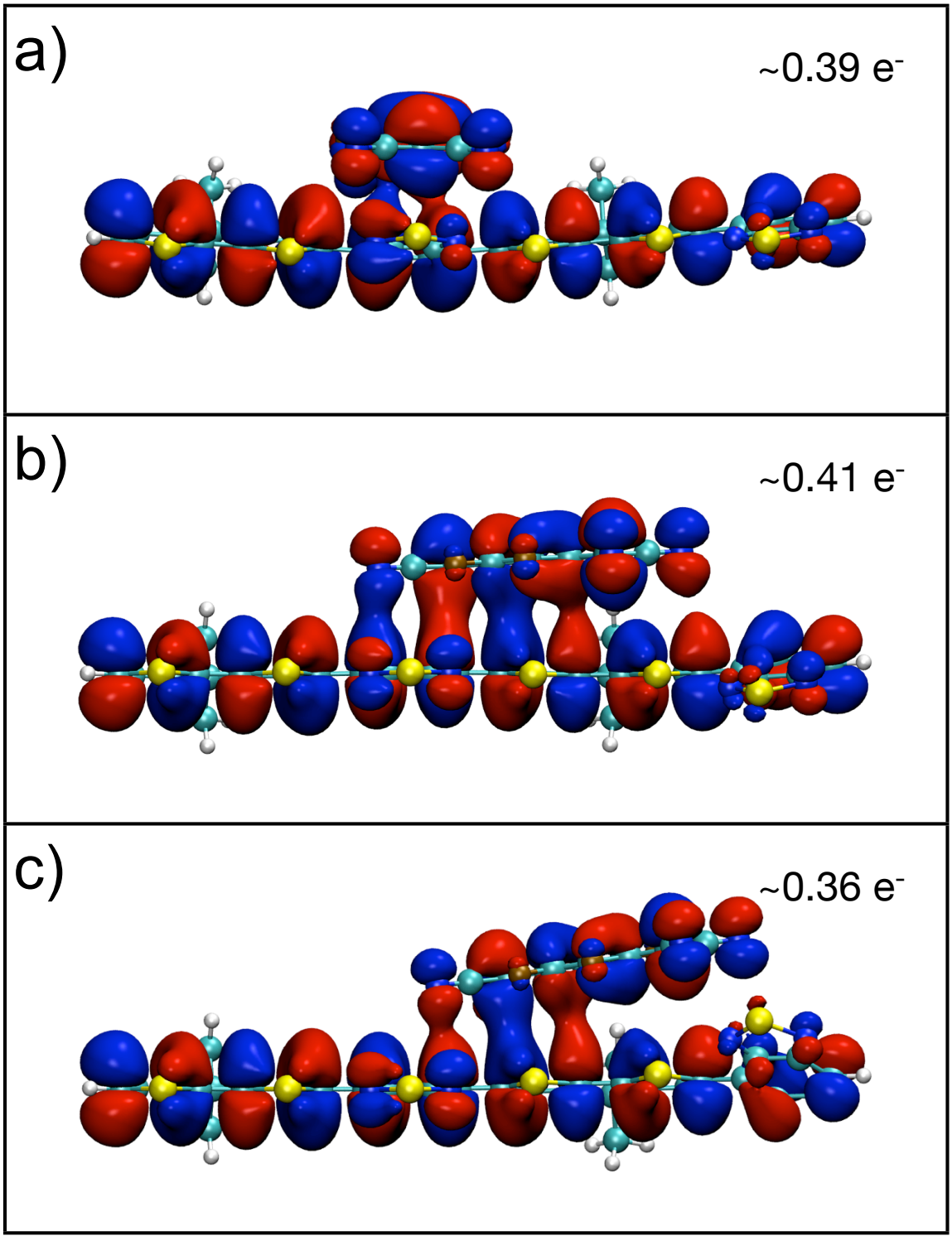

Figure 4.3.6. HOMO isosurfaces calculated for optimized geometries in Fig. 4.3.5 a), b), and c). Representations are at an isovalue of 0.01. Values in each pane indicate portion of electron transfer between the PCPDTBT dimer and F_4-TCNQ.

5. Experimental Methods

5.1 Sample Preparation

5.1.1 Thin Film Preparation For Absorption and Raman Spectroscopy

Thin film samples for optical absorption were prepared from 10 mg/mL PCPDTBT (Sigma-Aldrich), a 10 mg/mL 1:2 (w:w) blend of PCPDTBT/PCBM, and a 10 mg/mL 1:2:3 (w:w:w) blend of PCPDTBT, PCBM, and 1,8-octanedithiol (ODT) in chlorobenzene. The PCPDTBT and PCBM solutions were stirred at 100 °C overnight, then filtered through a 0.2 μm polytetrafluoroethylene (PTFE) filter to remove any remaining large particles. ODT was added to the polymer-PCBM blends for imaging experiments prior to deposition to promote phase separation by selectively dissolving PCBM molecules.

Solutions of PCPDTBT, DDQ, and F_4-TCNQ were prepared separately in chlorobenzene. The PCPDTBT solution was prepared at 10 mg/ml and the DDQ and F_4-TCNQ were prepared at 1 mg/ml to allow fine blend ratio control. The PCPDTBT solution was prepared as described above. The DDQ and F_4-TCNQ solutions were prepared at most one hour before blending with the PCPDTBT solution to retain DDQ and F_4-TCNQ activity. Blend solutions were mixed immediately before spin-casting or drop-casting. It is important to note that when doping PCPDTBT and other polymers with F_4-TCNQ, polymer-dopant salts will rapidly form clumps in solution due to the ease with which F_4-TCNQ induces ground-state charge transfer from most conjugated polymers because of its low-lying LUMO. These clumps are large enough to be visible to the eye when films are spin-cast at dopant concentrations above 1 wt %.

Glass cover slips for all samples were cleaned in an ultrasound bath in trichloroethylene (TCE), acetone, and methanol for 20 minutes in each solvent. The cover slips were then subjected to UV-ozone cleaning for 30 minutes. Thin film samples for absorption spectroscopy were spin cast onto cleaned glass cover slips at 500 rpm to achieve acceptable film thickness while maintaining film uniformity. Samples for Raman spectroscopy were prepared by drop-casting a solution of 1:3 PCPDTBT:PCBM (w/w) onto cleaned glass cover slips.

5.1.2 Nanoparticle Preparation

PCPDTBT nanoparticles were prepared by dissolving PCPDTBT in chloroform at 10 mg/ml, and blending the chloroform solution in a 1:2.5 volume ratio with a 10 mg/ml sodium dodecyl sulfate (SDS) solution in deionized (DI) water. The combined solution was stirred for 1 hour and sonicated for 5 minutes in a sealed container. Chloroform was evaporated from the blend solution by stirring at 60 °C for 2 hours in an open container. The nanoparticle suspension was then dialyzed for 24 hours in DI water with fresh DI water every two hours to remove excess surfactant. Absorption spectra of the nanoparticles were taken in suspension with 100 μl of finished nanoparticle suspension in 3 ml DI water in a quartz cuvette.

5.1.3 Solar Cell Device Preparation

Photovoltaic devices were prepared using blends of PCPDTBT, PCBM, and ODT in 10:20 mg/mL (PCPDTBT:PCBM) and 10:20:30 mg/mL (PCPDTBT:PCBM:ODT) ratios. Device substrates were indium tin oxide-coated glass cover slips cleaned by

sonication in trichloroethylene, acetone, and methanol for 20 minutes in each solvent. Substrates were subjected to UV-ozone treatment for 30 minutes after sonication. A layer of poly(3,4-ethylenedioxythiophene)**:**polystyrene sulfonate (PEDOT:PSS, Sigma Aldrich) was spun onto the substrates at 2000 rpm for 2 minutes, and then heated at 110°C for 30 minutes to remove any remaining water. Active layers were spin-cast onto the substrates at 500 rpm for one minute. Approximately 120 nm of aluminum was then evaporated onto the active layers through a shadow mask to create the cathode contacts. The rectifying and photovoltaic performance of each device was verified by collecting current-voltage curves in the dark and under air mass (AM) 1.5 illumination (routed to the device under test through a fiber bundle).

5.2 Spectroscopic Methods

5.2.1 Absorption Spectroscopy

Absorption spectra were collected using a Hitachi U-4100 spectrophotometer. For thin film spectra, a baseline spectrum was collected using a cleaned bare glass substrate. For nanoparticle suspension spectra, a baseline spectrum was collected using a quartz cuvette filled with deionized water. Spectra produced by manually subtracting the baseline spectra were identical to those produced by allowing the spectrometer software to subtract the baselines.

5.2.2 Raman Spectroscopy

Excitation sources for Raman spectroscopy included a tunable Ti:Sapphire laser for wavelengths spanning 700 – 850 nm, a Kr-ion laser for wavelengths spanning 520 –

647 nm, an Ar-ion laser for wavelengths from 458 – 488nm, and a frequency-doubled Ti:Sapphire laser for wavelengths from 387 – 430 nm. Raman spectra were acquired on a triple grating spectrometer (Spex, Princeton Instruments) for Ti:Sapphire excitation and a single grating spectrometer (Andor Shamrock) configured with a confocal microscope for Ar- and Kr-ion sources. Rayleigh scattering rejection edge filters were used in the latter apparatus. Details of both apparatus were described previously.[24] Excitation intensities were adjusted to minimize and maintain good photostability and several spectra were recorded at each wavelength on different samples. Photodegradation effects were minimal and successive measurements revealed similar Raman patterns and intensities. All spectra were corrected for instrument response and frequency calibration was checked by measuring known standards. Raman spectra of doped PCPDTBT thin films were collected on a Thermo Scientific DXR SmartRaman instrument using 780 nm excitation.

5.3 Spectroscopic and Photocurrent Imaging

5.3.1 Collection of Raman Images

Raman images were collected using a previously described microscope spectrometer setup[135] with a 5 second integration time per pixel with both 458 and 647 nm excitation. A simple schematic of the setup is shown in Figure 5.3.1.

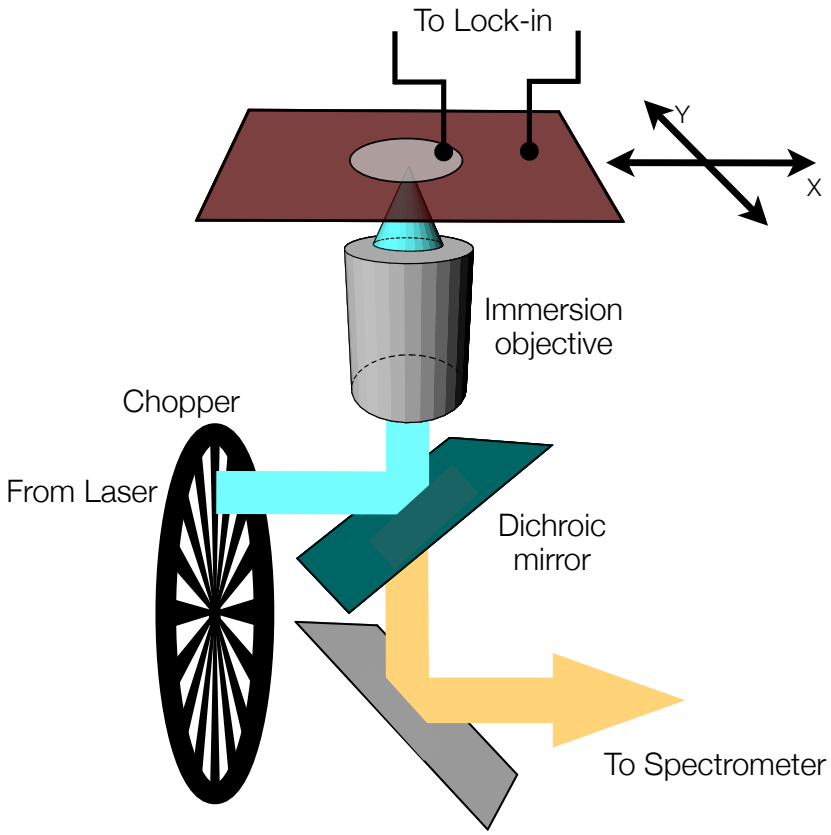

Figure 5.3.1. Basic schematic of the experimental Raman and photocurrent imaging setup.

5.3.2 Collection of Photocurrent Images

Photocurrent images were collected on the same setup as described above with excitation light chopped at 500 Hz. Photocurrent images were collected using 405 and 647 nm excitation from a diode laser (405 nm) and a Kr-ion laser (647 nm). A lock-in amplifier (Stanford Research SR830) was used to measure the current signal. Devices were kept in a nitrogen atmosphere during Raman and photocurrent imaging to avoid photodegradation.

Conclusions

Spectroscopic investigations of PCPDTBT in pristine nanoparticle and thin films and of PCPDTBT:PCBM and PCPDTBT:PCBM:ODT blend films have provided new insight into the conformational changes the polymer undergoes as a result of nanoparticle formation and in thin films with the addition of PCBM and ODT. The blue-shift in the low-energy polymer absorption peak of the PCPDTBT nanoparticles suggests increased disordering of the polymer chains as a result of rapid agglomeration. The red shifts in the absorption spectra of PCPDTBT thin film blends with PCB and ODT suggest increased ordering and planarization of the polymer domains as a result of electronic interactions with PCBM and phase segregation induced by ODT. Raman spectra collected while exciting PCPDTBT at wavelengths spanning its absorption profile have provided new information on the photophysical mechanisms behind the energetic behavior of this polymer. Correlating results of DFT calculations to these Raman spectra has allowed identification of specific vibrational modes on either the donor or acceptor moieties, and reveals preferential excitation of the acceptor moiety at low excitations energies and the donor moiety at high excitation energies. Raman and photocurrent imaging of solar cell devices reveal preferential interaction between PCBM and the BT acceptor moiety on the polymer backbone, and suggests that charge transfer occurs primarily via the BT moiety. Well blended regions of PCPDTBT:PCBM blend films produce more photocurrent than the more segregated regions, suggesting more charge transport pathways and better charge transfer between PCPDTBT and fullerene acceptors in those regions.

Spectroscopic investigations of PCDTBT thin films doped with the small molecule electron acceptors DDQ and F_4-TCNQ have provided insights into the

preferential interactions of these dopants with PCPDTBT. In particular, absorption spectra indicate the emergence of polymer polaron absorption at relatively low doping levels with DDQ and F_4-TCNQ, along with increased polymer chain ordering upon addition of as little as 0.1 wt % of both dopants. Raman spectra reveal increased activity of the acceptor (BT) upon doping with DDQ and F_4-TCNQ, suggesting the interactions between the dopants and the polymer, as well as charge localization, are concentrated on the acceptor moiety. Density functional theory calculations of complexes of a CPDTBT dimer with DDQ and F_4-TCNQ suggest that steric hindrance may significantly impact the ability of a small molecule dopant to interact with the polymer backbone, and that charge transfer between PCPDTBT and DDQ and F_4-TCNQ can be affected to varying degrees by the position of the dopants relative to the polymer donor and acceptor moieties.

Future Work

F1. Raman and Photocurrent Imaging of Doped PCPDTBT

As discussed in Chapter 3, Raman imaging can provide information on morphological features and specific interactions between species in thin films. This technique can be applied to thin films of PCPDTBT doped with DDQ and F_4-TCNQ, and can lead to greater understanding of morphological changes that occur in doped films as the doping levels are varied. Examining the intensities of the PCPDTBT Raman modes can yield insights into the relationships between polymer morphology and the electronic interactions between PCPDTBT and the two dopants, and frequency shifts in the major PCPDTBT Raman modes at different excitation wavelengths can provide information on the energy dependence of these preferential interactions.

Relating the Raman images to photocurrent images can reveal the locations of gradients in photocurrent production relative to the local film composition. This information can be applied to the design of active layer morphologies to enhance photocurrent generation for these and other polymer/dopant blends.

F2. N-Doping of PCPDTBT

The discussions in Chapter 4 touched on previous work that has shown enhanced power conversion efficiencies in solar cell devices through the addition of small amounts of small molecule electron acceptors in active layer blends. The enhancements in photovoltaic performance in these studies are attributed to increased hole concentrations and mobilities as a result of p-doping the polymer, which leads to improved hole conductivity in the polymer domains. We have explored some of the spectral signatures of conformational changes in PCPDTBT doped with DDQ and F_4-TCNQ, showing red-

shifted absorption line shapes and increased BT Raman activity due to increased order along the polymer backbone.

As yet, the morphological and spectral effects of n-doping of PCPDTBT or other conjugated polymers has not been explored to a great extent. It may be possible to n-dope commonly used homopolymers such as P3HT with metallocenes including ferrocene or cobaltocene. However, the LUMO level of PCPDTBT precludes the use of metallocenes, including decamethylated metallocenes as n-dopants for PCPDTBT. Cotton et al. discovered the organometallic compound ditungsten tetra(1,3,4,6,7,8-hexahydro-2H-pyrimido[1,2- a]pyrimidine) ($W_2(hpp)_4$) that has a ionization potential of 3.51 eV, making it more easily ionized than cesium.[136] This ionization potential lies just slightly above the LUMO of PCPDTBT (-3.55 eV), allowing ground state charge transfer to PCPDTBT. This energy offset is nearly one order of magnitude smaller than that between PCPDTBT and DDQ, and may result in more subtle and gradual changes in both morphology and resultant spectroscopic lineshapes than doping with DDQ. $W_2(hpp)_4$ will be difficult to handle as it is so easily ionized. However, Cotton et al. developed a chlorinated version, $W_2(hpp)_4Cl_2$, that is stable for storage and transport, and allows for a simple reduction reaction with potassium metal to produce $W_2(hpp)_4$.[137,138] Figure F1 shows the structures of $W_2(hpp)_4$ and $W_2(hpp)_4Cl_2$.

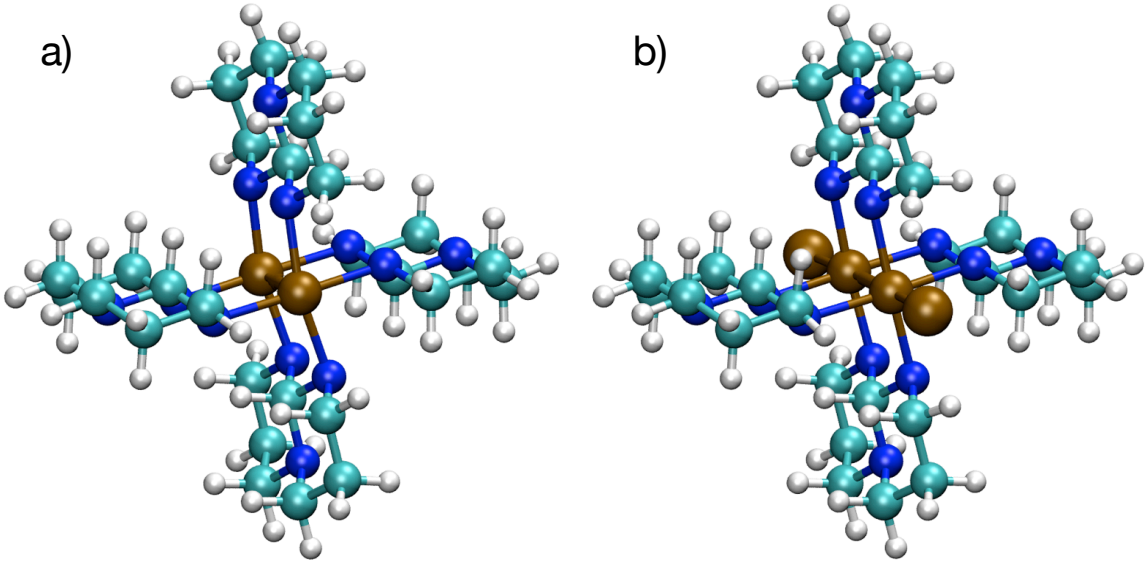

Figure F2.1. Structures of a) $W_2(hpp)_4$ and b) $W_2(hpp)_4Cl_2$. These images were produced with VMD 1.9.1, which assigns the same color to W and Cl. The Cl atoms are on the outside of the two central W atoms.

In addition, electron paramagnetic resonance (EPR) can provide information on the efficiency with which dopant molecules interact with conjugated polymers. For example, Gao et al. and Niklas et al. showed that EPR and light-induced EPR (LERP) signal strength is a good indicator of doping and PCBM intercalation in polymers including P3HT, Poly[[4,8- bis[(2-ethylhexyl)oxy]benzo[1,2-b:4,5-b']dithiophene- 2,6-diyl][3-fluoro-2-[(2-ethylhexyl)carbonyl]thieno[3,4- b]thiophenediyl]] (PTB7), and PCDTBT.[73,139] Kraffert et al. have investigated the EPR signatures of PCPDTBT:PCBM blends to elucidate the mechanisms of charge transfer in these blends.[140] The efficiency with which DDQ, F_4-TCNQ, and $W_2(hpp)_4$ intercalate and interact with PCPDTBT can be ascertained with EPR, and will be important information to support the findings in Chapter 4.

F3. Probing Local Dielectric Constants Through IMPS Imaging

Intensity modulated photocurrent spectroscopy (IMPS) was originally utilized to study photoelectrolysis at semiconductor electrodes in electrolyte baths. More recently, IMPS has been used to investigate the photogeneration and recombination dynamics in organic photovoltaics.[141-144] The authors of these and other studies of OPV with IMPS often invoke intensely complex models to explain the frequency response of OPV devices,[145-147] often proposing equivalent resistance-inductance-capacitance (RLC) circuits, yet there is no physical basis for including inductance as a parameter for modeling an OPV cell. However, it may be possible to couple IMPS with photocurrent imaging to probe local dielectric constants in OPV devices. With the idea that an OPV device is constructed like a capacitor, i.e. a dielectric medium sandwiched between two conducting plates, modeling the device as a capacitor with a series and shunt resistance may allow extraction of an effective dielectric constant for the region of the device under study. Rastering an excitation source across an area of a device, as with photocurrent and Raman imaging, IMPS response curves can be taken at each point, creating and IMPS image. The resonant frequencies of these response curves can be related to the capacitance of the device at each point, from which a relative permittivity, or dielectric constant, can be calculated through the relation:

$$C = \frac{\varepsilon A}{d} = \frac{\varepsilon_r \varepsilon_0 A}{d} \tag{F3.1}$$

where C is the capacitance, ε, ε_r, and ε_0 are the permittivity, relative permittivity, and permittivity of free space, A is area, and d is the thickness of the dielectric layer. This information can in turn be related to Raman and steady-state photocurrent images of the

same area, permitting correlation between morphology, dielectric constant, and photocurrent production.

References

(1) Liang, Y.; Xu, Z.; Xia, J.; Tsai, S.-T.; Wu, Y.; Li, G.; Ray, C.; Yu, L. For the Bright Future-Bulk Heterojunction Polymer Solar Cells with Power Conversion Efficiency of 7.4%. *Adv. Mater.* **2010**, *22*, E135–E138.

(2) Huo, L.; Hou, J. Benzo[1,2-B:4,5-B′]Dithiophene-Based Conjugated Polymers: Band Gap and Energy Level Control and Their Application in Polymer Solar Cells. *Polym. Chem.* **2011**, *2*, 2453.

(3) Huang, Y.; Guo, X.; Liu, F.; Huo, L.; Chen, Y.; Russell, T. P.; Han, C. C.; Li, Y.; Hou, J. Improving the Ordering and Photovoltaic Properties by Extending Π-Conjugated Area of Electron-Donating Units in Polymers with D-a Structure. *Adv. Mater.* **2012**, *24*, 3383–3389.

(4) Liang, Y.; Feng, D.; Wu, Y.; Tsai, S.-T.; Li, G.; Ray, C.; Yu, L. Highly Efficient Solar Cell Polymers Developed via Fine-Tuning of Structural and Electronic Properties. *J. Am. Chem. Soc.* **2009**, *131*, 7792–7799.

(5) Duan, C.; Huang, F.; Cao, Y. Recent Development of Push–Pull Conjugated Polymers for Bulk-Heterojunction Photovoltaics: Rational Design and Fine Tailoring of Molecular Structures. *Journal of Materials Chemistry* **2012**, *22*, 10416–10434.

(6) Carsten, B.; Szarko, J. M.; Son, H. J.; Wang, W.; Lu, L.; He, F.; Rolczynski, B. S.; Lou, S. J.; Chen, L. X.; Yu, L. Examining the Effect of the Dipole Moment on Charge Separation in Donor–Acceptor Polymers for Organic Photovoltaic Applications. *J. Am. Chem. Soc.* **2011**, *133*, 20468–20475.

(7) McCulloch, I.; Ashraf, R. S.; Biniek, L.; Bronstein, H.; Combe, C.; Donaghey, J. E.; James, D. I.; Nielsen, C. B.; Schroeder, B. C.; Zhang, W. Design of Semiconducting Indacenodithiophene Polymers for High Performance Transistors and Solar Cells. *Acc. Chem. Res.* **2012**, *45*, 714–722.

(8) Zhang, Z. G.; Wang, J. Structures and Properties of Conjugated Donor–Acceptor Copolymers for Solar Cell Applications. *Journal of Materials Chemistry* **2012**, *22*, 4178–4187.

(9) Kettle, J.; Horie, M.; Majewski, L. A.; Saunders, B. R.; Tuladhar, S.; Nelson, J.; Turner, M. L. Optimisation of PCPDTBT Solar Cells Using Polymer Synthesis with Suzuki Coupling. *Solar Energy Materials and Solar Cells* **2011**, *95*, 2186–2193.

(10) Mikhnenko, O. V.; Kuik, M.; Lin, J.; van der Kaap, N.; Nguyen, T.-Q.; Blom, P. W. M. Trap-Limited Exciton Diffusion in Organic Semiconductors. *Adv. Mater.* **2013**, *26*, 1912–1917.

(11) Mikhnenko, O. V.; Azimi, H.; Scharber, M.; Morana, M.; Blom, P. W. M.; Loi, M. A. Exciton Diffusion Length in Narrow Bandgap Polymers. *Energy Environ. Sci.* **2012**, *5*, 6960.

(12) Dunn, D. R.; Barrick, J.; Sweeney, A.; Davis, N.; Thapa, S.; Hankey, R. S.;

Kaplan, S.; Klein, M.; Wong, P.; Peterson, R.; et al. February 2015 Monthly Energy Review; DOE/EIA-0035(2015/02); U. S. Energy Information Administration, 2004; pp. 1–224.
(13) Chu, S. Letter From Secretary Steven Chu to Energy Department Employees; U. S. Department of Energy, 2013.
(14) Gaudiana, R.; Brabec, C. Organic Materials: Fantastic Plastic. *Nature Photon* **2008**, *2*, 287–289.
(15) Brabec, C. J.; Hauch, J. A.; Schilinsky, P.; Waldauf, C. Production Aspects of Organic Photovoltaics and Their Impact on the Commercialization of Devices. *MRS Bull.* **2011**, *30*, 50–52.
(16) Currie, M. J.; Mapel, J. K.; Heidel, T. D.; Goffri, S.; Baldo, M. A. High-Efficiency Organic Solar Concentrators for Photovoltaics. *Science* **2008**, *321*, 226–228.
(17) Kalowekamo, J.; Baker, E. Estimating the Manufacturing Cost of Purely Organic Solar Cells. *Solar Energy* **2009**, *83*, 1224–1231.
(18) Emmott, C. J. M.; Urbina, A.; Nelson, J. Environmental and Economic Assessment of ITO-Free Electrodes for Organic Solar Cells. *Solar Energy Materials and Solar Cells* **2012**, *97*, 14–21.
(19) Espinosa, N.; Garcia-Valverde, R.; Urbina, A. A Life Cycle Analysis of Polymer Solar Cell Modules Prepared Using Roll-to-Roll Methods Under Ambient Conditions. ... *Materials and Solar Cells* **2011**.
(20) Albrecht, S.; Janietz, S.; Schindler, W.; Frisch, J.; Kurpiers, J.; Kniepert, J.; Inal, S.; Pingel, P.; Fostiropoulos, K.; Koch, N.; et al. Fluorinated Copolymer PCPDTBT with Enhanced Open-Circuit Voltage and Reduced Recombination for Highly Efficient Polymer Solar Cells. *J. Am. Chem. Soc.* **2012**, *134*, 14932–14944.
(21) Coffin, R. C.; Peet, J.; Rogers, J.; Bazan, G. C. Streamlined Microwave-Assisted Preparation of Narrow-Bandgap Conjugated Polymers for High-Performance Bulk Heterojunction Solar Cells. *Nature Chem* **2009**, *1*, 657–661.
(22) Hou, J.; Chen, H.-Y.; Zhang, S.; Li, G.; Yang, Y. Synthesis, Characterization, and Photovoltaic Properties of a Low Band Gap Polymer Based on Silole-Containing Polythiophenes and 2,1,3-Benzothiadiazole. *J. Am. Chem. Soc.* **2008**, *130*, 16144–16145.
(23) Lee, J. K.; Ma, W. L.; Brabec, C. J.; Yuen, J.; Moon, J. S.; Kim, J. Y.; Lee, K.; Bazan, G. C.; Heeger, A. J. Processing Additives for Improved Efficiency From Bulk Heterojunction Solar Cells. *J. Am. Chem. Soc.* **2008**, *130*, 3619–3623.
(24) Peet, J.; Kim, J. Y.; Coates, N. E.; Ma, W. L.; Moses, D.; Heeger, A. J.; Bazan, G. C. Efficiency Enhancement in Low-Bandgap Polymer Solar Cells by Processing with Alkane Dithiols. *Nat Mater* **2007**, *6*, 497–500.
(25) Gelinas, S.; Rao, A.; Kumar, A.; Smith, S. L.; Chin, A. W.; Clark, J.; van der Poll, T. S.; Bazan, G. C.; Friend, R. H. Ultrafast Long-Range Charge Separation in Organic Semiconductor Photovoltaic Diodes. *Science* **2014**, *343*, 512–516.
(26) Becquerel, E. Mémoire Sur Les Effets Électriques Produits Sous L'influence

Des Rayons Solaires. *Comptes Rendus* **1839**, *9*, 561–567.
(27) Chapin, D. M.; Fuller, C. S.; Pearson, G. L. A New Silicon P-N Junction Photocell for Converting Solar Radiation Into Electrical Power. *J. Appl. Phys.* **1954**, *25*, 676.
(28) Kearns, D.; Calvin, M. Photovoltaic Effect and Photoconductivity in Laminated Organic Systems. *J. Chem. Phys.* **1958**, *29*, 950.
(29) Ghosh, A. K.; Morel, D. L.; Feng, T.; Shaw, R. F.; Rowe, C. A. Photovoltaic and Rectification Properties of Al/Mg Phthalocyanine/Ag Schottky-Barrier Cells. *J. Appl. Phys.* **1974**, *45*, 230.
(30) Tang, C. W. Two-Layer Organic Photovoltaic Cell. *Appl. Phys. Lett.* **1986**, *48*, 183.
(31) Suslick, K. S.; Chen, C.-T.; Meredith, G. R.; Cheng, L.-T. Push-Pull Porphyrins as Nonlinear Optical Materials. *J. Am. Chem. Soc.* **1992**, *114*, 6928–6930.
(32) Sariciftci, N. S.; Braun, D.; Zhang, C. Semiconducting Polymer-Buckminsterfullerene Heterojunctions: Diodes, Photodiodes, and Photovoltaic Cells. *Appl. Phys. Lett.* **1993**, *62*, 585–587.
(33) Yu, G.; Gao, J.; Hummelen, J. C.; Wudl, F.; Heeger, A. J. Polymer Photovoltaic Cells: Enhanced Efficiencies via a Network of Internal Donor-Acceptor Heterojunctions. *Science* **1995**, *270*, 1789–1791.
(34) MacKenzie, J. D.; Arias, A. C.; Friend, R. H.; Huck, W. Optoelectronic Devices and a Method for Producing the Same. US 8,049,406 B2, October 24, 2002.
(35) Wilson, G.; VanSant, K.; Ullal, H. Best Research-Cell Efficiencies; National Renewable Energy Laboratory, 2015.
(36) Le Séguillon, T.; Rohr, S. Heliatek Consolidates Its Technology Leadership by Establishing a New World Record for Organic Solar Technology with a Cell Efficiency of 12%, 2013, *Treidlerstraße 3 01139 Dresden, Germany*, 1–3.
(37) Li, G.; Zhu, R.; Yang, Y. Polymer Solar Cells. *Nature Photon* **2012**, *6*, 153–161.
(38) Veldman, D.; Meskers, S. C. J.; Janssen, R. A. J. The Energy of Charge-Transfer States in Electron Donor-Acceptor Blends: Insight Into the Energy Losses in Organic Solar Cells. *Advanced Functional Materials* **2009**, *19*, 1939–1948.
(39) Kroon, R.; Lenes, M.; Hummelen, J. C.; Blom, P. W. M.; de Boer, B. Small Bandgap Polymers for Organic Solar Cells (Polymer Material Development in the Last 5 Years). *Polymer Reviews* **2008**, *48*, 531–582.
(40) Deibel, C.; Strobel, T.; Dyakonov, V. Role of the Charge Transfer State in Organic Donor-Acceptor Solar Cells. *Adv. Mater.* **2010**, *22*, 4097–4111.
(41) Günes, S.; Neugebauer, H.; Sariciftci, N. S. Conjugated Polymer-Based Organic Solar Cells. *Chemical Reviews* **2007**.
(42) Clarke, T. M.; Durrant, J. R. Charge Photogeneration in Organic Solar Cells. *Chemical Reviews* **2010**, *110*, 6736–6767.
(43) Sims, M.; Tuladhar, S.; Nelson, J.; Maher, R.; Campoy-Quiles, M.; Choulis, S.; Mairy, M.; Bradley, D.; Etchegoin, P.; Tregidgo, C.; et al. Correlation

Between Microstructure and Charge Transport in Poly(2,5-Dimethoxy-P-Phenylenevinylene) Thin Films. *Phys. Rev. B* **2007**, *76*, 195206.
(44) Myers, A. B. Resonance Raman Intensities and Charge-Transfer Reorganization Energies. *Chemical Reviews* **1996**, *96*, 911–926.
(45) Marcus, R. A. Chemical and Electrochemical Electron-Transfer Theory. *Annual Review of Physical Chemistry* **1964**.
(46) Barbara, P. F.; Meyer, T. J.; Ratner, M. A. Contemporary Issues in Electron Transfer Research. *J. Phys. Chem.* **1996**, *100*, 13148–13168.
(47) Deibel, C.; Dyakonov, V.; Brabec, C. J. Organic Bulk-Heterojunction Solar Cells. *IEEE J. Select. Topics Quantum Electron. 16*, 1517–1527.
(48) Brabec, C. J.; Cravino, A.; Meissner, D.; Sariciftci, N. S.; Fromherz, T.; Rispens, M. T.; Sanchez, L.; Hummelen, J. C. Origin of the Open Circuit Voltage of Plastic Solar Cells. *Advanced Functional Materials* **2001**, *11*, 374–380.
(49) Albrecht, S.; Schäfer, S.; Lange, I.; Yilmaz, S.; Dumsch, I.; Allard, S.; Scherf, U.; Hertwig, A.; Neher, D. Light Management in PCPDTBT:PC70BM Solar Cells: a Comparison of Standard and Inverted Device Structures. *Organic Electronics* **2012**, *13*, 615–622.
(50) Ko, H. M.; Choi, H.; Paek, S.; Kim, K.; Song, K. Molecular Engineering of Push-Pull Chromophore for Efficient Bulk-Heterojunction Morphology in Solution Processed Small Molecule Organic Photovoltaics - Journal of Materials Chemistry (RSC Publishing) DOI:10.1039/C1JM10667H. *Journal of Materials …* **2011**.
(51) Provencher, F.; Sakowicz, M. Slow Geminate-Charge-Pair Recombination Dynamics at Polymer: Fullerene Heterojunctions in Efficient Organic Solar Cells - Provencher - 2012 - Journal of Polymer Science Part B: Polymer Physics - Wiley Online Library. *Journal of Polymer …* **2012**.
(52) Zeigler, D. F.; Chen, K.-S.; Yip, H.-L.; Zhang, Y.; K Y Jen, A. Tunable Light-Harvesting Polymers Containing Embedded Dipolar Chromophores for Polymer Solar Cell Applications. *J. Polym. Sci. A Polym. Chem.* **2012**, *50*, 1362–1373.
(53) Boland, P.; Lee, K.; Namkoong, G. Device Optimization in PCPDTBT:PCBM Plastic Solar Cells. *Solar Energy Materials and Solar Cells* **2010**, *94*, 915–920.
(54) Chang, S. Y.; Liao, H. C.; Shao, Y. T.; Sung, Y. M. Enhancing the Efficiency of Low Bandgap Conducting Polymer Bulk Heterojunction Solar Cells Using P3HT as a Morphology Control Agent - Journal of Materials Chemistry a (RSC Publishing) DOI:10.1039/C2TA00990K. *Journal of Materials Chemistry A* **2013**.
(55) Chappell, J.; Lidzey, D. G.; Jukes, P. C.; Higgins, A. M.; Thompson, R. L.; O'Connor, S.; Grizzi, I.; Fletcher, R.; O'Brien, J.; Hammond, G. S.; et al. Correlating Structure with Fluorescence Emission in Phase-Separated Conjugated-Polymer Blends. *Nat Mater* **2003**, *2*, 616–621.
(56) Fazzi, D.; Grancini, G.; Maiuri, M.; Brida, D.; Cerullo, G.; Lanzani, G. Ultrafast Internal Conversion in a Low Band Gap Polymer for Photovoltaics: Experimental and Theoretical Study. *Physical Chemistry Chemical Physics*

2012, *14*, 6367–6374.
(57) Hutchison, G. R.; Ratner, M. A.; Marks, T. J. Hopping Transport in Conductive Heterocyclic Oligomers: Reorganization Energies and Substituent Effects. *J. Am. Chem. Soc.* **2005**, *127*, 2339–2350.
(58) Ku, J.; Kim, D.; Ryu, T.; Jung, E.; Lansac, Y. Time-Dependent Density Functional Theory Study on Cyclopentadithiophene- Benzothiadiazole-Based Push-Pull-Type Copolymers for New Design of Donor Materials in Bulk Heterojunction Organic Solar Cells. *Bull Korean Chem …* **2012**, *33*, 1029–1036.
(59) Schmidtke, J. P.; Kim, J.-S.; Gierschner, J.; Silva, C.; Friend, R. H. Optical Spectroscopy of a Polyfluorene Copolymer at High Pressure: Intra- and Intermolecular Interactions. *Phys. Rev. Lett.* **2007**, *99*, 167401.
(60) Aggarwal, R. L.; Farrar, L. W.; Saikin, S. K.; Andrade, X.; Aspuru-Guzik, A.; Polla, D. L. Measurement of the Absolute Raman Cross Section of the Optical Phonons in Type Ia Natural Diamond. *Solid State Communications* **2012**, *152*, 204–209.
(61) Li, B.; Myers, A. B. Absolute Raman Cross Sections for Cyclohexane, Acetonitrile, and Water in the Far-Ultraviolet Region. *Journal of Physical Chemistry* **1990**, *94*, 4051–4054.
(62) Reigue, A.; Auguié, B.; Etchegoin, P. G.; Le Ru, A. C. CW Measurements of Resonance Raman Profiles, Line-Widths, and Cross-Sections of Fluorescent Dyes: Application to Nile Blue a in Water and Ethanol. *J. Raman Spectrosc.* **2013**, *44*, 573–581.
(63) Meyer, S. A.; Ru, E. C. L.; Etchegoin, P. G. Quantifying Resonant Raman Cross Sections with SERS. *J. Phys. Chem. A* **2010**, *114*, 5515–5519.
(64) Le Ru, E. C.; Schroeter, L. C.; Etchegoin, P. G. Direct Measurement of Resonance Raman Spectra and Cross Sections by a Polarization Difference Technique. *Anal. Chem.* **2012**, *84*, 5074–5079.
(65) Lee, H. M.; Jin, S. M.; Kim, H. M.; Suh, Y. D. Single-Molecule Surface-Enhanced Raman Spectroscopy: a Perspective on the Current Status. *Phys Chem Chem Phys* **2013**, *15*, 5276.
(66) Heller, E. J.; Sundberg, R.; Tannor, D. Simple Aspects of Raman Scattering. *J. Phys. Chem.* **1982**, *86*, 1822–1833.
(67) Heller, E. J. The Semiclassical Way to Molecular Spectroscopy. *Acc. Chem. Res.* **1981**, *14*, 368–375.
(68) Tannor, D. J. Polyatomic Raman Scattering for General Harmonic Potentials. *J. Chem. Phys.* **1982**, *77*, 202–218.
(69) Zink, J. I.; Shin, K.-S. K. Molecular Distortions in Excited Electronic States Determined From Electronic and Resonance Raman Spectroscopy. In; Volman, D. H.; Hammond, G. S.; Neckers, D. C., Eds.; John Wiley & Sons, Inc.: Hoboken, NJ, USA, 1991; Vol. 16.
(70) Myers, A. B. "Time-Dependent" Resonance Raman Theory. *J. Raman Spectrosc.* **1997**, *28*, 389–401.
(71) Zink, J. I.; Shin, K.-S. K. Molecular Distortions in Excited Electronic States Determined From Electronic and Resonance Raman Spectroscopy. In *Advances in Photochemistry*; Volman, D. H.; Hammond, G. S.; Neckers, D.

C., Eds.; John Wiley & Sons, Inc., 1991; Vol. 16, pp. 119–214.
(72) Niles, E. T.; Roehling, J. D.; Yamagata, H.; Wise, A. J.; Spano, F. C.; Moulé, A. J.; Grey, J. K. J-Aggregate Behavior in Poly-3-Hexylthiophene Nanofibers. *J. Phys. Chem. Lett.* **2012**, *3*, 259–263.
(73) Gao, J.; Niles, E. T.; Grey, J. K. Aggregates Promote Efficient Charge Transfer Doping of Poly(3-Hexylthiophene). *J. Phys. Chem. Lett.* **2013**, *4*, 2953–2957.
(74) Gao, J.; Kamps, A.; Park, S.-J.; Grey, J. K. Encapsulation of Poly(3-Hexylthiophene) J-Aggregate Nanofibers with an Amphiphilic Block Copolymer. *Langmuir* **2012**, *28*, 16401–16407.
(75) Gao, Y.; Martin, T. P.; Niles, E. T.; Wise, A. J.; Thomas, A. K.; Grey, J. K. Understanding Morphology-Dependent Polymer Aggregation Properties and Photocurrent Generation in Polythiophene/Fullerene Solar Cells of Variable Compositions. *J. Phys. Chem. C* **2010**, 100818141308067.
(76) Gao, J.; Thomas, A. K.; Johnson, R.; Guo, H.; Grey, J. K. Spatially Resolving Ordered and Disordered Conformers and Photocurrent Generation in Intercalated Conjugated Polymer/Fullerene Blend Solar Cells. *Chem. Mater.* **2014**, *26*, 4395–4404.
(77) Cho, S.; Lee, J. K.; Moon, J. S.; Yuen, J.; Lee, K.; Heeger, A. J. Bulk Heterojunction Bipolar Field-Effect Transistors Processed with Alkane Dithiol. *Organic Electronics* **2008**.
(78) Chow, P. C. Y.; Gélinas, S.; Rao, A.; Friend, R. H. Quantitative Bimolecular Recombination in Organic Photovoltaics Through Triplet Exciton Formation. *J. Am. Chem. Soc.* **2014**, 140212170954008.
(79) Coates, N. E.; Hwang, I.-W.; Peet, J.; Bazan, G. C.; Moses, D.; Heeger, A. J. 1,8-Octanedithiol as a Processing Additive for Bulk Heterojunction Materials: Enhanced Photoconductive Response. *Appl. Phys. Lett.* **2008**, *93*, 072105.
(80) Etzold, F.; Howard, I. A.; Forler, N.; Cho, D. M.; Meister, M.; Mangold, H.; Shu, J.; Hansen, M. R.; Müllen, K.; Laquai, F. The Effect of Solvent Additives on Morphology and Excited-State Dynamics in PCPDTBT:PCBM Photovoltaic Blends. *J. Am. Chem. Soc.* **2012**, *134*, 10569–10583.
(81) Hwang, I. W.; Soci, C.; Moses, D.; Zhu, Z.; Waller, D.; Gaudiana, R.; Brabec, C. J.; Heeger, A. J. Ultrafast Electron Transfer and Decay Dynamics in a Small Band Gap Bulk Heterojunction Material. *Adv. Mater.* **2007**, *19*, 2307–2312.
(82) Rogers, J. T.; Schmidt, K.; Toney, M. F.; Kramer, E. J.; Bazan, G. C. Structural Order in Bulk Heterojunction Films Prepared with Solvent Additives. *Adv. Mater.* **2011**, *23*, 2284–2288.
(83) Grancini, G.; Maiuri, M.; Fazzi, D.; Petrozza, A.; Egelhaaf, H.-J.; Brida, D.; Cerullo, G.; Lanzani, G. Hot Exciton Dissociation in Polymer Solar Cells. *Nat Mater* **2012**, *12*, 29–33.
(84) Reish, M. E.; Nam, S.; Lee, W.; Woo, H. Y.; Gordon, K. C. A Spectroscopic and DFT Study of the Electronic Properties of Carbazole-Based D–a Type Copolymers. *J. Phys. Chem. C* **2012**, *116*, 21255–21266.
(85) Jespersen, K. G.; Beenken, W. J. D.; Zaushitsyn, Y.; Yartsev, A.; Andersson,

M.; Pullerits, T.; Sundström, V. The Electronic States of Polyfluorene Copolymers with Alternating Donor-Acceptor Units. *J. Chem. Phys.* **2004**, *121*, 12613.

(86) Yamamoto, S.; Ohkita, H.; Benten, H.; Ito, S. Role of Interfacial Charge Transfer State in Charge Generation and Recombination in Low-Bandgap Polymer Solar Cell. *J. Phys. Chem. C* **2012**, *116*, 14804–14810.

(87) Hwang, I.-W.; Cho, S.; Kim, J. Y.; Lee, K.; Coates, N. E.; Moses, D.; Heeger, A. J. Carrier Generation and Transport in Bulk Heterojunction Films Processed with 1,8-Octanedithiol as a Processing Additive. *J. Appl. Phys.* **2008**, *104*, 033706.

(88) Park, S. H.; Roy, A.; Beaupré, S.; Cho, S.; Coates, N.; Moon, J. S.; Moses, D.; Leclerc, M.; Lee, K.; Heeger, A. J. Bulk Heterojunction Solar Cells with Internal Quantum Efficiency Approaching 100%. *Nature Photon* **2009**, *3*, 297–302.

(89) Tsutsumi, J.; Matsuzaki, H.; Kanai, N.; Yamada, T.; Hasegawa, T. Charge Separation and Recombination of Charge-Transfer Excitons in Donor–Acceptor Polymer Solar Cells. *J. Phys. Chem. C* **2013**, *117*, 16769–16773.

(90) Love, J. A.; Proctor, C. M.; Liu, J.; Takacs, C. J.; Sharenko, A.; van der Poll, T. S.; Heeger, A. J.; Bazan, G. C.; Nguyen, T. Q. Film Morphology of High Efficiency Solution-Processed Small-Molecule Solar Cells. *Advanced Functional Materials* **2013**, *23*, 5019–5026.

(91) Habuchi, S.; Fujita, H.; Michinobu, T.; Vacha, M. Twist Angle Plays an Important Role in Photophysical Properties of a Donor–Acceptor-Type Conjugated Polymer: a Combined Ensemble and Single-Molecule Study. *J. Phys. Chem. B* **2011**, *115*, 14404–14415.

(92) Distler, A.; Kutka, P.; Sauermann, T.; Egelhaaf, H.-J.; Guldi, D. M.; Di Nuzzo, D.; Meskers, S. C. J.; Janssen, R. A. J. Effect of PCBM on the Photodegradation Kinetics of Polymers for Organic Photovoltaics. *Chem. Mater.* **2012**, *24*, 4397–4405.

(93) Kastner, J.; Kuzmany, H.; Vegh, D.; Landl, M.; Cuff, L.; Kertesz, M. Raman Spectra and Ground State of the New Low Bandgap Polymer Poly(Thienopyrazine). *Synthetic Metals* **1995**, *69*, 593–594.

(94) Yu, W.; Donohoo-Vallett, P. J.; Zhou, J.; Bragg, A. E. Ultrafast Photo-Induced Nuclear Relaxation of a Conformationally Disordered Conjugated Polymer Probed with Transient Absorption and Femtosecond Stimulated Raman Spectroscopies. *J. Chem. Phys.* **2014**, *141*.

(95) Provencher, F.; Bérubé, N.; Parker, A. W.; Greetham, G. M.; Towrie, M.; Hellmann, C.; Côté, M.; Stingelin, N.; Silva, C.; Hayes, S. C. Direct Observation of Ultrafast Long-Range Charge Separation at Polymer–Fullerene Heterojunctions. *Nature Communications* **2014**, *5*, 1–11.

(96) Fischer, F. S. U.; Tremel, K.; Saur, A. K.; Link, S.; Kayunkid, N.; Brinkmann, M.; Herrero-Carvajal, D.; Navarrete, J. T. L.; Delgado, M. C. R.; Ludwigs, S. Influence of Processing Solvents on Optical Properties and Morphology of a Semicrystalline Low Bandgap Polymer in the Neutral and Charged States. *Macromolecules* **2013**, *46*, 4924–4931.

(97) Cornil, J.; Gueli, I.; Dkhissi, A.; Sancho-Garcia, J. C.; Hennebicq, E.;

Calbert, J. P.; Lemaur, V.; Beljonne, D.; Brédas, J. L. Electronic and Optical Properties of Polyfluorene and Fluorene-Based Copolymers: a Quantum-Chemical Characterization. *J. Chem. Phys.* **2003**, *118*, 6615.

(98) Winfield, J. M.; Van Vooren, A.; Park, M.-J.; Hwang, D.-H.; Cornil, J. M.; Kim, J.-S.; Friend, R. H. Charge-Transfer Character of Excitons in Poly[2,7-(9,9-Di-N-Octylfluorene)[Sub (1−X)]-Co-4,7-(2,1,3-Benzothiadiazole)[Sub (X)]]. *J. Chem. Phys.* **2009**, *131*, 035104.

(99) Risko, C.; McGehee, M. D.; Brédas, J. L. A Quantum-Chemical Perspective Into Low Optical-Gap Polymers for Highly-Efficient Organic Solar Cells. *Chemical Science* **2011**, *2*, 1200–1218.

(100) Albrecht, S.; Schindler, W.; Kurpiers, J.; Kniepert, J.; Blakesley, J. C.; Dumsch, I.; Allard, S.; Fostiropoulos, K.; Scherf, U.; Neher, D. On the Field Dependence of Free Charge Carrier Generation and Recombination in Blends of PCPDTBT/PC 70BM: Influence of Solvent Additives. *J. Phys. Chem. Lett.* **2012**, *3*, 640–645.

(101) Dongaonkar, S.; Servaites, J. D.; Ford, G. M.; Loser, S.; Moore, J.; Gelfand, R. M.; Mohseni, H.; Hillhouse, H. W.; Agrawal, R.; M A Ratner; et al. Universality of Non-Ohmic Shunt Leakage in Thin-Film Solar Cells. *J. Appl. Phys.* **2010**, *108*, 1–12.

(102) Wetzelaer, G. A. H.; Kuik, M.; Lenes, M.; Blom, P. W. M. Origin of the Dark-Current Ideality Factor in Polymer:Fullerene Bulk Heterojunction Solar Cells. *Appl. Phys. Lett.* **2011**, *99*, 153506.

(103) Street, R. A.; Cowan, S.; Heeger, A. J. Experimental Test for Geminate Recombination Applied to Organic Solar Cells. *Phys. Rev. B* **2010**, *82*, 121301.

(104) Finck, B. Y.; Schwartz, B. J. Understanding the Origin of the S-Curve in Conjugated Polymer/Fullerene Photovoltaics From Drift-Diffusion Simulations. *Appl. Phys. Lett.* **2013**, *103*, 053306.

(105) Gao, J.; Roehling, J. D.; Li, Y.; Guo, H.; Moulé, A. J.; Grey, J. K. The Effect of 2,3,5,6-Tetrafluoro-7,7,8,8-Tetracyanoquinodimethane Charge Transfer Dopants on the Conformation and Aggregation of Poly(3-Hexylthiophene). *J. Mater. Chem. C* **2013**, *1*, 5638.

(106) Wise, A. J.; Grey, J. K. Resonance Raman Studies of Excited State Structural Displacements of Conjugated Polymers in Donor/Acceptor Charge Transfer Complexes. *Phys Chem Chem Phys* **2012**, *14*, 11273–11276.

(107) Agostinelli, T.; Ferenczi, T. A. M.; Pires, E.; Foster, S.; Maurano, A.; Müller, C.; Ballantyne, A.; Hampton, M.; Lilliu, S.; Campoy-Quiles, M.; et al. The Role of Alkane Dithiols in Controlling Polymer Crystallization in Small Band Gap Polymer:Fullerene Solar Cells. *J. Polym. Sci. B Polym. Phys.* **2011**, *49*, 717–724.

(108) Chambon, S.; Mens, R.; Vandewal, K.; Clodic, E.; Scharber, M.; Lutsen, L.; Gelan, J.; Manca, J.; Vanderzande, D.; Adriaensens, P. Influence of Octanedithiol on the Nanomorphology of PCPDTBTPCBM Blends Studied by Solid-State NMR. *Solar Energy Materials and Solar Cells* **2012**, *96*, 210–217.

(109) Morana, M.; Wegscheider, M.; Bonanni, A.; Kopidakis, N.; Shaheen, S.;

Scharber, M.; Zhu, Z.; Waller, D.; Gaudiana, R.; Brabec, C. Bipolar Charge Transport in PCPDTBT-PCBM Bulk-Heterojunctions for Photovoltaic Applications. *Advanced Functional Materials* **2008**, *18*, 1757–1766.

(110) Jackson, N. E.; Savoie, B. M.; Marks, T. J.; Chen, L. X.; Ratner, M. A. The Next Breakthrough for Organic Photovoltaics? *J. Phys. Chem. Lett.* **2015**, *6*, 77–84.

(111) Wei, P.; Oh, J. H.; Dong, G.; Bao, Z. Use of a 1 H-Benzoimidazole Derivative as an N-Type Dopant and to Enable Air-Stable Solution-Processed N-Channel Organic Thin-Film Transistors. *J. Am. Chem. Soc.* **2010**, *132*, 8852–8853.

(112) Olthof, S.; Mehraeen, S.; Mohapatra, S. K.; Barlow, S.; Coropceanu, V.; Bredas, J.-L.; Marder, S. R.; Kahn, A. Ultralow Doping in Organic Semiconductors: Evidence of Trap Filling. *Phys. Rev. Lett.* **2012**, *109*, 176601.

(113) Zhang, Y.; de Boer, B.; Blom, P. W. M. Trap-Free Electron Transport in Poly(P-Phenylene Vinylene) by Deactivation of Traps with N-Type Doping. *Phys. Rev. B* **2010**, *81*, 085201.

(114) Veysel Tunc, A.; De Sio, A.; Riedel, D.; Deschler, F.; Da Como, E.; Parisi, J.; Hauff, von, E. Molecular Doping of Low-Bandgap-Polymer:Fullerene Solar Cells: Effects on Transport and Solar Cells. *Organic Electronics* **2012**, *13*, 290–296.

(115) Loiudice, A.; Rizzo, A.; Biasiucci, M.; Gigli, G. Bulk Heterojunction Versus Diffused Bilayer: the Role of Device Geometry in Solution P-Doped Polymer-Based Solar Cells. *J. Phys. Chem. Lett.* **2012**, *3*, 1908–1915.

(116) Zhang, Y.; Zhou, H.; Seifter, J.; Ying, L.; Mikhailovsky, A.; Heeger, A. J.; Bazan, G. C.; Nguyen, T.-Q. Molecular Doping Enhances Photoconductivity in Polymer Bulk Heterojunction Solar Cells. *Adv. Mater.* **2013**, *25*, 7038–7044.

(117) Gong, X.; Tong, M.-H.; Park, S. H.; Liu, M.; Jen, A.; Heeger, A. J. Semiconducting Polymer Photodetectors with Electron and Hole Blocking Layers: High Detectivity in the Near-Infrared. *Sensors* **2010**, *10*, 6488–6496.

(118) Meyer, J.; Hamwi, S.; Schmale, S.; Winkler, T.; Johannes, H.-H.; Riedl, T.; Kowalsky, W. A Strategy Towards P-Type Doping of Organic Materials with HOMO Levels Beyond 6 eV Using Tungsten Oxide. *Journal of Materials Chemistry* **2009**, *19*, 702.

(119) Panda, P.; Veldman, D.; Sweelssen, J.; Bastiaansen, J. J. A. M.; Langeveld-Voss, B. M. W.; Meskers, S. C. J. Charge Transfer Absorption for Π-Conjugated Polymers and Oligomers Mixed with Electron Acceptors. *J. Phys. Chem. B* **2007**, *111*, 5076–5081.

(120) Thompson, B. C.; Kim, Y.-G.; Reynolds, J. R. Spectral Broadening in MEH-PPV:PCBM-Based Photovoltaic Devices via Blending with a Narrow Band Gap Cyanovinylene−Dioxythiophene Polymer. *Macromolecules* **2005**, *38*, 5359–5362.

(121) Rao, A.; Chow, P. C. Y.; Gélinas, S.; Schlenker, C. W.; Li, C.-Z.; Yip, H.-L.; Jen, A. K. Y.; Ginger, D. S.; Friend, R. H. The Role of Spin in the Kinetic Control of Recombination in Organic Photovoltaics. *Nature* **2013**, *500*, 435–

439.
(122) Clarke, T.; Ballantyne, A.; Jamieson, F.; Brabec, C. Transient Absorption Spectroscopy of Charge Photogeneration Yields and Lifetimes in a Low Bandgap Polymer/Fullerenefilm. *Chem. Commun.* **2009**.
(123) Deschler, F. How Molecular Doping Affects the Charge Separation Process in Polymer-Fullerene Blends, Dissertation: Bayreuth, 2012.
(124) Di Nuzzo, D.; Aguirre, A.; Shahid, M.; Gevaerts, V. S.; Meskers, S. C. J.; Janssen, R. A. J. Improved Film Morphology Reduces Charge Carrier Recombination Into the Triplet Excited State in a Small Bandgap Polymer-Fullerene Photovoltaic Cell. *Adv. Mater.* **2010**, *22*, 4321–4324.
(125) Bakulin, A. A.; Rao, A.; Pavelyev, V. G.; van Loosdrecht, P. H. M.; Pshenichnikov, M. S.; Niedzialek, D.; Cornil, J.; Beljonne, D.; Friend, R. H. The Role of Driving Energy and Delocalized States for Charge Separation in Organic Semiconductors. *Science* **2012**, *335*, 1340–1344.
(126) Naka, K.; Chujo, Y. Organo-Arsenic, Phosphorus, and Antimony Conjugated Polymers. In *Conjugated Polymer Synthesis*; Conjugated polymer synthesis : methods and reactions; Wiley-VCH Verlag GmbH & Co. KGaA: Weinheim, 2010; pp. 229–249.
(127) Miller, J. S.; Krusic, P. J.; Dixon, D. A.; Reiff, W. M.; Zhang, J. H.; Anderson, E. C.; Epstein, A. J. Radical Ion Salts of 2,3-Dichloro-5,6-Dicyanobenzoquinone and Metallocenes. a Reexamination of Their Magnetic and Spectroscopic Properties. *J. Am. Chem. Soc.* **1986**, *108*, 4459–4466.
(128) Sidorov, A.; Vashkinskaya, O.; Grigorieva, A.; Shekhovtsova, T.; Veselova, I.; Goodilin, E. Entrapment Into Charge Transfer Complexes for Resonant Raman Scattering Enhancement. *Chem. Commun.* **2014**, *50*, 6468–6470.
(129) SUBHANI, M. S.; BHATTI, N. K.; MOHAMMAD, M.; KHAN, A. Y. Spectroscopic Studies of Charge-Transfer Complexes of 2,3-Dichloro-5,6-Dicyano-P-Benzo-Quinone. *Turk J Chem* **2000**, *24*, 223–230.
(130) Fathima, A.; Rao, S.; Venkateshwarlu, G. Spectrophotometric Determination of Drugs Using 2,3 Dichloro 5,6 Dicyano P- Benzoquinone as Analytical Reagent. *International Journal of ChemTech Research* **2011**, *3*, 1769–1780.
(131) Ghani, F.; Opitz, A.; Pingel, P.; Heimel, G.; Salzmann, I.; Frisch, J.; Neher, D.; Tsami, A.; Scherf, U.; Koch, N. Charge Transfer in and Conductivity of Molecularly Doped Thiophene-Based Copolymers. *J. Polym. Sci. B Polym. Phys.* **2014**, *53*, 58–63.
(132) Yim, K.-H.; Whiting, G. L.; Murphy, C. E.; Halls, J. J. M.; Burroughes, J. H.; Friend, R. H.; Kim, J.-S. Controlling Electrical Properties of Conjugated Polymers via a Solution-Based P-Type Doping. *Adv. Mater.* **2008**, *20*, 3319–3324.
(133) Pingel, P.; Neher, D. Comprehensive Picture of P-Type Doping of P3HT with the Molecular Acceptor F4TCNQ. *Phys. Rev. B* **2013**, *87*, 115209.
(134) Di Nuzzo, D.; Fontanesi, C.; Jones, R.; Allard, S.; Dumsch, I.; Scherf, U.; Hauff, von, E.; Schumacher, S.; Da Como, E. How Intermolecular Geometrical Disorder Affects the Molecular Doping of Donor–Acceptor Copolymers. *Nature Communications* **2015**, *6*, 1–8.

(135) Gao, Y.; Grey, J. K. Resonance Chemical Imaging of Polythiophene/Fullerene Photovoltaic Thin Films: Mapping Morphology-Dependent Aggregated and Unaggregated C═C Species. *J. Am. Chem. Soc.* **2009**, *131*, 9654–9662.

(136) Cotton, F. A.; Gruhn, N. E.; Gu, J.; Huang, P.; Lichtenberger, D. L.; Murillo, C. A.; Van Dorn, L. O.; Wilkinson, C. C. Closed-Shell Molecules That Ionize More Readily Than Cesium. *Science* **2002**, *298*, 1971–1974.

(137) Cotton, F. A.; Donahue, J. P.; Gruhn, N. E.; Lichtenberger, D. L.; Murillo, C. A.; Timmons, D. J.; Van Dorn, L. O.; Villagrán, D.; Wang, X. Facilitating Access to the Most Easily Ionized Molecule: an Improved Synthesis of the Key Intermediate, W 2(Hpp) 4Cl 2, and Related Compounds. *Inorg. Chem.* **2006**, *45*, 201–213.

(138) Cotton, F. A.; Donahue, J. P.; Lichtenberger, D. L.; Murillo, C. A.; Villagran, D. Expeditious Access to the Most Easily Ionized Closed-Shell Molecule, W-2(hPP)(4). *J. Am. Chem. Soc.* **2005**, *127*, 10808–10809.

(139) Niklas, J.; Mardis, K. L.; Banks, B. P.; Grooms, G. M.; Sperlich, A.; Dyakonov, V.; Beaupré, S.; Leclerc, M.; Xu, T.; Yu, L.; et al. Highly-Efficient Charge Separation and Polaron Delocalization in Polymer–Fullerene Bulk-Heterojunctions: a Comparative Multi-Frequency EPR and DFT Study. *Phys Chem Chem Phys* **2013**, *15*, 9562.

(140) Kraffert, F.; Steyrleuthner, R.; Albrecht, S.; Neher, D.; Scharber, M. C.; Bittl, R.; Behrends, J. Charge Separation in PCPDTBT:PCBM Blends From an EPR Perspective. *J. Phys. Chem. C* **2014**, *118*, 28482–28493.

(141) van de Lagemaat, J.; Park, N. G.; Frank, A. J. Influence of Electrical Potential Distribution, Charge Transport, and Recombination on the Photopotential and Photocurrent Conversion Efficiency of Dye-Sensitized Nanocrystalline TiO 2Solar Cells: a Study by Electrical Impedance and Optical Modulation Techniques. *J. Phys. Chem. B* **2000**, *104*, 2044–2052.

(142) Krüger, J.; Plass, R.; Grätzel, M.; Cameron, P. J.; Peter, L. M. Charge Transport and Back Reaction in Solid-State Dye-Sensitized Solar Cells: a Study Using Intensity-Modulated Photovoltage and Photocurrent Spectroscopy. *J. Phys. Chem. B* **2003**, *107*, 7536–7539.

(143) Byers, J. C.; Ballantyne, S.; Rodionov, K.; Mann, A.; Semenikhin, O. A. Mechanism of Recombination Losses in Bulk Heterojunction P3HT:PCBM Solar Cells Studied Using Intensity Modulated Photocurrent Spectroscopy. *ACS Appl. Mater. Interfaces* **2011**, *3*, 392–401.

(144) Dloczik, L.; Ileperuma, O.; Lauermann, I.; L M Peter; Ponomarev, E. A.; Redmond, G.; Shaw, N. J.; Uhlendorf, I. Dynamic Response of Dye-Sensitized Nanocrystalline Solar Cells: Characterization by Intensity-Modulated Photocurrent Spectroscopy. *J. Phys. Chem. B* **1997**, *101*, 10281–10289.

(145) Mora-Seró, I.; Bisquert, J.; Fabregat-Santiago, F.; Garcia-Belmonte, G.; Zoppi, G.; Durose, K.; Proskuryakov, Y.; Oja, I.; Belaidi, A.; Dittrich, T.; et al. Implications of the Negative Capacitance Observed at Forward Bias in Nanocomposite and Polycrystalline Solar Cells. *Nano Lett.* **2006**, *6*, 640–650.

(146) Fabregat-Santiago, F.; Bisquert, J.; Palomares, E.; Otero, L.; Kuang, D.; Zakeeruddin, S. M.; Gratzel, M. Correlation Between Photovoltaic Performance and Impedance Spectroscopy of Dye-Sensitized Solar Cells Based on Ionic Liquids. *J. Phys. Chem. C* **2007**, *111*, 6550–6560.

(147) Garcia-Belmonte, G.; Munar, A.; Barea, E. M.; Bisquert, J.; Ugarte, I.; Pacios, R. Charge Carrier Mobility and Lifetime of Organic Bulk Heterojunctions Analyzed by Impedance Spectroscopy. *Organic Electronics* **2008**, *9*, 847–851.